

REPORT DOCUMENTATION PAGE			Form Approved OMB NO. 0704-0188		
<p>The public reporting burden for this collection of information is estimated to average 1 hour per response, including the time for reviewing instructions, searching existing data sources, gathering and maintaining the data needed, and completing and reviewing the collection of information. Send comments regarding this burden estimate or any other aspect of this collection of information, including suggestions for reducing this burden, to Washington Headquarters Services, Directorate for Information Operations and Reports, 1215 Jefferson Davis Highway, Suite 1204, Arlington VA, 22202-4302. Respondents should be aware that notwithstanding any other provision of law, no person shall be subject to any penalty for failing to comply with a collection of information if it does not display a currently valid OMB control number.</p> <p>PLEASE DO NOT RETURN YOUR FORM TO THE ABOVE ADDRESS.</p>					
1. REPORT DATE (DD-MM-YYYY)		2. REPORT TYPE Technical Report		3. DATES COVERED (From - To) -	
4. TITLE AND SUBTITLE Josephson Parametric Amplification for Circuit Quantum Electrodynamics: Theory and Implementation		5a. CONTRACT NUMBER W911NF-08-1-0189			
		5b. GRANT NUMBER			
		5c. PROGRAM ELEMENT NUMBER 611102			
6. AUTHORS Christopher M. Quintana		5d. PROJECT NUMBER			
		5e. TASK NUMBER			
		5f. WORK UNIT NUMBER			
7. PERFORMING ORGANIZATION NAMES AND ADDRESSES Princeton University Office of Research & Project Administration The Trustees of Princeton University Princeton, NJ 08544 -0036			8. PERFORMING ORGANIZATION REPORT NUMBER		
9. SPONSORING/MONITORING AGENCY NAME(S) AND ADDRESS(ES) U.S. Army Research Office P.O. Box 12211 Research Triangle Park, NC 27709-2211			10. SPONSOR/MONITOR'S ACRONYM(S) ARO		
			11. SPONSOR/MONITOR'S REPORT NUMBER(S) 53367-PH-PCS.10		
12. DISTRIBUTION AVAILABILITY STATEMENT Approved for public release; distribution is unlimited.					
13. SUPPLEMENTARY NOTES The views, opinions and/or findings contained in this report are those of the author(s) and should not be construed as an official Department of the Army position, policy or decision, unless so designated by other documentation.					
14. ABSTRACT Princeton Undergraduate Senior Thesis Circuit Quantum Electrodynamics (cQED) is a highly promising platform for quantum control, quantum simulation, and quantum optics in a solid-state environment. Such systems consist of artificial atoms coupled to superconducting resonators, and can be probed with microwave signals on a chip. This thesis theoretically and					
15. SUBJECT TERMS quantum measurement					
16. SECURITY CLASSIFICATION OF:			17. LIMITATION OF ABSTRACT UU	15. NUMBER OF PAGES	19a. NAME OF RESPONSIBLE PERSON Jason Petta
a. REPORT UU	b. ABSTRACT UU	c. THIS PAGE UU			19b. TELEPHONE NUMBER 609-258-1173

Report Title

Josephson Parametric Amplification for Circuit Quantum Electrodynamics: Theory and Implementation

ABSTRACT

Princeton Undergraduate Senior Thesis

Circuit Quantum Electrodynamics (cQED) is a highly promising platform for quantum control, quantum simulation, and quantum optics in a solid-state environment. Such systems consist of artificial atoms coupled to superconducting resonators, and can be probed with microwave signals on a chip. This thesis theoretically and experimentally studies a method of quantum-limited Josephson parametric amplification for the improvement of such microwave measurements. A theoretical analysis of parametric amplification with a nonlinear quantum oscillator is given, along with an analysis of a particular implementation with a superconducting coplanar waveguide resonator shunted by an array of SQUIDs. A parametric amplifier chip is designed and a fabrication process is engineered. Measurements and analysis of a successfully fabricated device are presented, and future outlook is discussed.

JOSEPHSON PARAMETRIC AMPLIFICATION FOR
CIRCUIT QUANTUM ELECTRODYNAMICS:
THEORY AND IMPLEMENTATION

CHRISTOPHER MICHAEL QUINTANA

A SENIOR THESIS
PRESENTED TO THE FACULTY
OF PRINCETON UNIVERSITY
IN PARTIAL FULFILLMENT OF THE DEGREE OF
BACHELOR OF ARTS

DEPARTMENT OF PHYSICS
ADVISOR: JASON R. PETTA
SECOND READER: ANDREW A. HOUCK

PRINCETON UNIVERSITY

MAY 2013

ABSTRACT

JOSEPHSON PARAMETRIC AMPLIFICATION FOR CIRCUIT QUANTUM ELECTRODYNAMICS: THEORY AND IMPLEMENTATION

Christopher Michael Quintana

Department of Physics

Bachelor of Arts

Circuit Quantum Electrodynamics (cQED) is a highly promising platform for quantum control, quantum simulation, and quantum optics in a solid-state environment. Such systems consist of artificial atoms coupled to superconducting resonators, and can be probed with microwave signals on a chip. This thesis theoretically and experimentally studies a method of quantum-limited Josephson parametric amplification for the improvement of such microwave measurements. A theoretical analysis of parametric amplification with a nonlinear quantum oscillator is given, along with an analysis of a particular implementation with a superconducting coplanar waveguide resonator shunted by an array of SQUIDs. A parametric amplifier chip is designed and a fabrication process is engineered. Measurements and analysis of a successfully fabricated device are presented, and future outlook is discussed.

This thesis represents my own work in accordance with University regulations.

– *Chris Quintana*

ACKNOWLEDGMENTS

The work performed in this thesis would not have been completed were it not for the kindness and help of others in the Petta and Houck labs. I would especially like to thank Karl Petersson for teaching me various clean room fabrication techniques and for generally providing advice, and Sri Srinivasan for his infinite patience in answering the many questions about junction fabrication with which I pestered him throughout the semester. Both of them are excellent scientists and role models. I am in addition very grateful for the assistance of Loren Alegria, George Stehlik, Jeff Cady, Yanbing Liu, Gengyan Zhang, Devin Underwood, and Ted Brundage. I also want to acknowledge the friendship and support of my labmates, especially Will McFaul and Anasua Chatterjee. I (and all other lab members) also thank Mr. Bean, our coffee/espresso machine, for always being there.

Next, I want to thank Prof. Petta for taking me into his lab during the summer of my freshman year. Working in the Petta lab over the past few years has been the most challenging but most rewarding experience I've ever had. Prof. Petta is a shining example of how much can be accomplished with determination, hard work, and ingenuity. We have also been very fortunate to have Prof. Houck (who happens to be a well-known leader in the field of superconducting qubits) as a collaborator on our circuit QED experiments. The combination of Prof. Houck's excellent (and enthusiastic) quantum computing classes and my laboratory experience under Prof. Petta has without a doubt solidified my resolve to become an experimentalist in the incredibly rich and challenging field of solid-state quantum information. I still find it amazing that it is possible, with the aid of modern technology (as demonstrated in this thesis), to manufacture and control such tiny quantum mechanical systems that behave according to theoretical predictions.

Next, I apologize to my friends Ethan and Austin for not goofing off nearly as much as they would have liked me to throughout the year. Finally, I wish more than words can express to thank my family for their unwavering support, and dedicate this work to my grandmother Toby.

Contents

Table of Contents	iv
1 Introduction and Motivation	1
1.1 Quantum Computation	1
1.2 Circuit QED: Quantum Optics on a Chip	2
1.3 Thesis Overview	5
2 Parametric Amplification	7
2.1 A Classical Intuition: Parametric Resonance	7
2.2 Parametric Amplification with a Quantum Duffing Oscillator	10
2.2.1 Input-Output Theory	11
2.2.2 Pumping the Oscillator	15
2.2.3 Parametric Amplification of Small Perturbations	21
3 Implementation with Superconducting Circuits: Theory	35
3.1 Superconductivity	36
3.1.1 Background	36
3.1.2 Josephson Junctions	37
3.1.3 SQUIDs	39
3.2 Circuit Quantization	42
3.2.1 Linear Part	42
3.2.2 Kerr Nonlinearity	50
4 Implementation with Superconducting Circuits: Experiment	53
4.1 Design and Fabrication	53
4.1.1 Coplanar Waveguide Resonators	54
4.1.2 Fabrication of SQUIDs	64
4.2 Amplifier Implementation and Characterization	72
4.2.1 Nonlinearity	76
4.2.2 Parametric Gain	77
4.3 Future Directions	83

A	Quantization of the Electromagnetic Field in a Perfectly Conducting Cavity	85
B	The Jaynes-Cummings Hamiltonian	89
	B.1 Derivation	89
	B.2 Coupling Phenomena	93
C	Transmission Line Circuits	98
	Bibliography	100

Chapter 1

Introduction and Motivation

1.1 Quantum Computation

Building a quantum information processor is currently an active area of experimental research in physics and engineering. In the standard model of quantum computation, the familiar logical bit (0 or 1) of a classical computer is replaced by a two-level quantum system to form a quantum bit, or *qubit*, with computational basis states denoted by $|0\rangle$ and $|1\rangle$. Algorithms that take advantage of uniquely quantum behavior, such as superposition of basis states and entanglement of qubits, allow certain computational tasks to be completed in an inherently more efficient way than any known (and in some cases any possible) classical algorithm. Two now-famous examples are Shor's algorithm, which uses a quantum mechanical speedup in taking a discrete Fourier transform to factor numbers exponentially faster than we know how to classically, and Grover's algorithm, which yields a quadratic speedup in the brute-force solution of NP problems (essentially any problem whose answer can be efficiently checked) [1,2]. The techniques of quantum computation are also promising as a means of studying the behavior of computationally intractable quantum systems.

Since any two-level quantum system will in principle function as a qubit, many physical architectures have been and are still being pursued. There are certain obvious requirements that any physical implementation should satisfy, widely known as the DiVincenzo criteria [3]:

- (D1) Scalable, well-characterized qubits.
- (D2) Initialization of qubits; say, to $|000\dots\rangle$.
- (D3) Long coherence times relative to gate speeds.
- (D4) A universal set of quantum gates.
- (D5) Qubit state readout.

Criterion (D1) means that we should have qubits in the first place. If we don't have a natural two-level system like a spin- $\frac{1}{2}$ particle, we require a quantum system with anharmonic, isolatable energy levels so that a two-level subspace approximation can be made. This way, our computations will only drive transitions between two chosen levels (although, the clever use of higher auxiliary levels can aid in computations). Requirement (D1) also means that we should know the qubit parameters necessary for the performance of the quantum gates of (D4). In the prominent gate model of quantum computation, "gates" are simply pre-determined unitary time-evolution operations on quantum states resulting from carefully engineered Hamiltonians. "Universal" in (D4) refers to the fact that any quantum gate can be written as a composition of single-qubit gates and a single type of entangling two-qubit gate [3] (i.e., a gate which cannot be written as the tensor product of two one-qubit gates). This requirement poses the necessary challenge of coupling different physical qubits together for the generation of entanglement. The controllable coupling of more than a few qubits has shown to be an extremely difficult experimental task. Decoherence of fragile quantum states due to internal noise and unwanted interaction with the environment puts a limit on how many quantum gates can be performed before the quantum states change undesirably by decaying to their ground states (relaxation) or losing their relative complex phase information (dephasing). In fact, it is surprising that useful quantum computation is thought to be possible at all in the face of decoherence – remarkably, feedback-based quantum error correction schemes have been developed which show that below certain error and fidelity thresholds, computations can succeed with arbitrarily high probability [4]. In particular, the use of so-called "surface codes," in which fault tolerance emerges out of a fabric of logical qubits formed by many physical qubits with nearest-neighbor coupling, is a highly promising (though highly ambitious) route to take with superconducting qubits [5, 6]. The ability to quickly, reliably, and nondestructively read out quantum states is therefore an essential part of (D5). Even one working quantum computer would be an incredibly marvelous accomplishment. Due to these difficulties and the specific nature of known quantum algorithms (not to mention the expensive laboratory equipment needed), one shouldn't expect to see personal quantum computers in the future, but rather servers allotting (valuable) quantum computation time to users, not unlike in today's supercomputing clusters.

1.2 Circuit QED: Quantum Optics on a Chip

This thesis focuses on a method, to be described shortly, of improving (D5) in arguably the most promising implementation of quantum computation: circuit quantum electrodynamics (cQED), a field which has seen incredible progress over the past decade. As illustrated

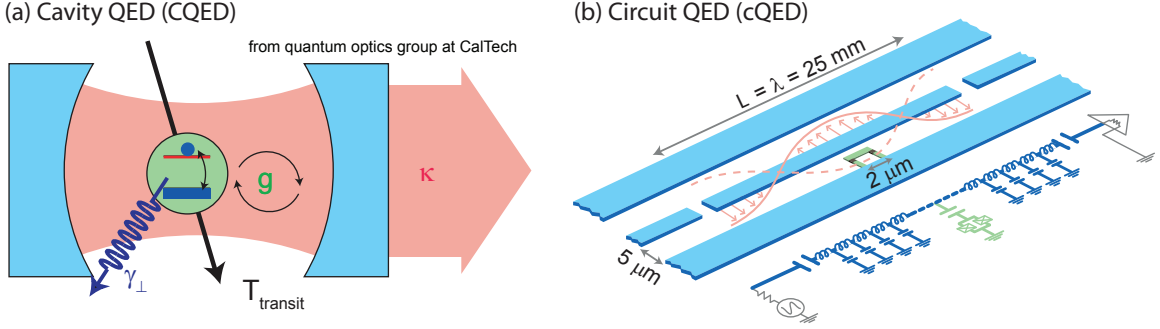


Figure 1.1 (a) Cavity Quantum Electrodynamics (CQED): A two-level atom interacting with a single mode of the electromagnetic field with coupling strength g . κ is the rate at which photons decay out of the cavity, set by the transparency of mirror-like walls. γ_{\perp} is the rate at which the atom decays into modes not trapped by the cavity via other mechanisms. T_{transit} is the amount of time that the atom spends in the cavity. (b) Circuit QED (cQED): Modern solid-state offspring of CQED in which a spatially fixed artificial atom interacts with a resonator formed by a coplanar waveguide circuit on a chip. Figure adapted from [7].

in Figure 1.1, cQED stems from cavity quantum electrodynamics (CQED), the study of atoms interacting with photons in cavities, which was well-studied before it was considered for quantum computation [8]. In CQED, the interaction of an atom with a single mode of the electromagnetic field can cause a quantum of energy to coherently oscillate between an atomic excitation and a cavity photon, a phenomenon known as vacuum Rabi oscillation. This process, depicted in Figure 1.1(a), occurs at a rate related to the coupling strength g until photons leak out of the cavity. This phenomenon has no obvious classical counterpart and requires a quantum theory of light to explain. To a good approximation, such a system is described by the *Jaynes-Cummings Hamiltonian*¹

$$H_{\text{JC}} = \hbar\omega_r \left(a^{\dagger}a + \frac{1}{2} \right) + \frac{1}{2}\hbar\omega_a\sigma_z + \hbar g(\sigma_+a + \sigma_-a^{\dagger}), \quad (1.1)$$

where a and σ_- are lowering operators for the cavity mode and the atom, respectively. In circuit QED, the atom and cavity are replaced by a solid-state “artificial atom” and (usually) a coplanar waveguide resonator on a chip. This modern development has among other advantages the capability of being conveniently fabricated on a chip with standard clean room techniques, allowing for a significant amount of man-made control over design parameters and for artificial atoms that are spatially stationary.

It can be shown (see Appendix B.2) that when the detuning $|\Delta| \equiv |\omega_a - \omega_r|$ of the atom

¹For a discussion of electromagnetic field quantization and an in-depth derivation of (1.1), the interested reader may consult Appendices A and B.

from the resonator mode is large compared to the coupling g , under a change of basis the “dispersive” Hamiltonian can be well-approximated by

$$H_{\text{disp}} \approx \hbar \left(\omega_r + \frac{g^2}{\Delta} \sigma_z \right) \left(a^\dagger a + \frac{1}{2} \right) + \frac{1}{2} \hbar \omega_a \sigma_z. \quad (1.2)$$

Comparing the first term with the form of a standard harmonic oscillator Hamiltonian, we can interpret the effect of the dispersive coupling as an effective qubit state-dependent shift in the cavity’s resonance frequency. By probing the cavity near resonance with a signal weak enough not to disturb the qubit, one can reliably read out the qubit’s state [8]. In fact, the above Hamiltonian generalizes to the case of several qubits coupled to a single cavity mode, and the dispersive readout method can be used to infer the joint state of multiple qubits at once [9, 10]. The dispersive regime also provides an effective coupling between two qubits coupled to the same resonator, allowing the performance of two-qubit gates [8, 9, 11]. “Building a quantum computer” is a phrase that has been thrown around a lot over the past decade or so, but in just the past couple of years, very impressive progress in superconducting qubit coherence times and scalability (for example, [12–14]) have made this goal no longer insane (for lack of a better word), but rather only insanely (for lack of better word) difficult. If steady progress continues, it is not unreasonable to speculate that a large-scale practical quantum computer could be built within ~ 20 years from now.

Besides its potential use for quantum information processing, circuit QED offers an exquisite solid-state test bed for the rich field of quantum optics in the microwave regime. A special case of this is the dispersive readout of qubits mentioned above. Because cQED systems have characteristic energies in the microwave regime (much lower than optical energies), it is a difficult task to detect signals at the level of a few photons. For nondestructive quantum feedback and other interesting quantum optics experiments, it is necessary to probe systems using signals of low average photon number. Commercial amplifiers can work for many of these experiments, at the expense of adding significant noise and thereby requiring long averaging times and potentially disturbing the quantum system being probed. This in general arises from the lack of control over many microscopic degrees of freedom (such as electrons in a high-electron mobility transistor [HEMT]) that need to be coupled to the input signal for energy transfer to occur. It would be nice to have a linear amplifier with a noise temperature below 1 K at microwave frequencies. In accordance with Frii’s formula for a chain of amplifiers [15, 16], an initial amplification with a low noise figure and high gain will lead to an effective SNR at later stages of amplification determined by the added noise figure of the first stage (and the SNR of the original input signal).

To date, the most successful microwave amplifiers have been based on so-called para-

metric amplification [17], which can achieve the best added-noise performance allowed by quantum mechanics. In general, parametric amplification is a phenomenon which occurs when some reactive parameter oscillates near twice the frequency of an oscillating system, allowing energy to be pumped into or out of an input/output port to create an amplifier. Such an oscillation can naturally be achieved in systems consisting of a nonlinear oscillator. In the context of superconducting electrical circuits, such microwave detectors were first explored in the late 1980s by Yurke *et. al.* [18, 19]. In recent years, interest in such quantum-limited amplifiers based on Josephson junctions has seen a great resurgence due to applications to quantum information and astronomical metrology [20–26], with each variant of Josephson parametric amplifier having its own strengths and weaknesses. As a result, in very recent years, impressive experiments have been enabled by such amplifiers, including the realtime monitoring of quantum jumps in a superconducting qubit [27], feedback control and state preparation of superconducting qubits [28, 29], the measurement of nontrivial microwave photon correlation statistics [30, 31], significant advances in quantum measurements [25], and the monitoring of a qubit state via a partial back-action measurement [32]. Quantum-limited microwave amplifiers, then, allow interesting quantum optics experiments to be performed that would otherwise be too difficult due to a loss of detection efficiency. In general, better amplifiers lead to more efficient experiments. In particular, the implementation of quantum-limited amplifiers for quantum feedback is an extremely important and active area of research in the current effort to achieve scalable quantum error correction.

1.3 Thesis Overview

The goal of this thesis is to thoroughly study the theory behind Josephson parametric amplification, engineer a physical design, and experimentally make and test such an amplifier in the laboratory. In Chapter 2, an in-depth treatment of the theory of parametric amplification with a quantum Duffing oscillator will be given. Unlike in this introduction, an attempt to be thorough and guide the reader through all of the important physics will be made. We will explore the origins of parametric amplification in nonlinear quantum systems and analyze important practical considerations and tradeoffs such as gain, bandwidth, dynamic range, phase-sensitivity, and added noise. In particular, it will be shown that this method of parametric amplification can in principle yield an amplifier that adds the least amount of noise allowed by quantum theory. In the following chapter (Chapter 3), an in-depth theoretical treatment of a particular implementation with superconducting circuits is discussed; namely, how a quantum Duffing oscillator naturally arises out of a system composed of an array of SQUIDs terminating the centerpin of a $\lambda/4$ coplanar waveguide

resonator. Such an amplifier can be driven with a single-mode pump field of reasonable power and also have its amplified band tuned in frequency via the SQUIDs. Finally, in Chapter 4, we will first describe in detail the development of a process to physically make such an amplifier from scratch using clean room techniques. Various practical design factors are considered based on the theory developed in the previous two chapters. Finally, measurements characterizing a successfully fabricated Josephson parametric amplifier are presented. The behavior of the parametric amplifier is analyzed and future prospects for using it as a tool in other experiments are discussed.

Chapter 2

Parametric Amplification

2.1 A Classical Intuition: Parametric Resonance

Before delving into a thorough quantum mechanical treatment, in order to obtain an intuition behind parametric amplification we will briefly discuss the classical phenomenon of parametric resonance, to which we will eventually compare the quantum case. A parametric oscillator is one whose *parameters*, such as a spring constant or damping term, vary in time [33,34]. A simple example of such a system is a small-angle pendulum with a vertically oscillating support point, or a child (partially) pumping a swing already in motion by periodically standing and squatting. Here, the time-varying length of the pendulum multiplies the dynamical variable θ in its equation of motion. In the context of the classical spring oscillator studied in freshman physics, a parametric oscillator has the second-order linear differential equation of motion

$$\ddot{x} + 2\gamma(t)\dot{x} + \frac{k(t)}{m}x = 0. \quad (2.1)$$

Without loss of generality we can assume $\gamma(t) = 0$ by making the change of variables $q(t) = e^{\int_0^t \gamma(\tau) d\tau} x(t)$ [33, 35], effectively moving into an “undamped” frame in which the equation of motion becomes

$$\ddot{q} + \omega_1^2(t)q = 0, \quad (2.2)$$

where $\omega_1^2(t) = k(t)/m - \gamma^2(t) - \dot{\gamma}(t)$ is the effective natural frequency of the q -oscillator. When $\omega_1(t)$ is a periodic function of time, this is known in mathematics as a *Hill equation*. Let us suppose, as is often the case, that $\omega_1(t)$ is varied via a sinusoidal perturbation. We

write this in the canonical form

$$w_1^2(t) = \omega_0^2 [1 + h \cos(2\omega_p t)], \quad (2.3)$$

where $h \ll 1$. With this form for $\omega_1^2(t)$, equation (2.2) is known in mathematics as the *Mathieu equation*. To gain an intuitive understanding of parametric resonance, we substitute (2.3) into (2.2) and bring the oscillating parameter to the right hand side,

$$\ddot{q} + \omega_0^2 q = -h\omega_0^2 \cos(2\omega_p t)q. \quad (2.4)$$

This represents a driven simple harmonic oscillator, with an effective driving term proportional to the response q . Starting for the moment with $h = 0$, the solution is simple harmonic motion, $q(t) = a \cos(\omega_0 t)$ (choosing the appropriate origin of time). As an approximation, we can substitute $q = a \cos(\omega_0 t)$ on the right hand side,

$$\begin{aligned} \ddot{q} + \omega_0^2 q &= -h\omega_0^2 a \cos(2\omega_p t) \cos(\omega_0 t) \\ &= -h\omega_0^2 \frac{a}{2} [\cos([2\omega_p - \omega_0]t) + \cos([2\omega_p + \omega_0]t)]. \end{aligned} \quad (2.5)$$

Resonance will occur when the effective driving frequency is equal to the effective natural frequency ω_0 . We see that this happens in the first term¹ when $2\omega_p = 2\omega_0$ and the second term then becomes an effective off-resonant drive at frequency $3\omega_0$ which, as studied in freshman physics [36], is heavily filtered out and can be ignored to a good approximation. Therefore, if $\omega_1(t)$ is perturbed with a frequency close to $2\omega_0$ (i.e., *twice* the natural frequency of the oscillator), we effectively have a simple harmonic oscillator driven near resonance, with the driving force proportional to the amplitude of existing oscillations. But this suggests that the amplitude of oscillation will grow exponentially (unless the amplitude is initially zero)! Roughly, this idea is known as *parametric resonance*. Of course, our analysis was by no means rigorous and is not exact, but this is in fact what happens – it can be shown through a more thorough analysis [33] that for a parameter modulation of frequency of $2\omega_0 + \epsilon$ (where $|\epsilon| < \frac{1}{h}\omega_0$ is small), the amplitude of the non-transient sinusoidal response² at frequency $\omega_0 + \frac{1}{2}\epsilon$ is proportional to e^{st} , where $s = \frac{1}{2}\sqrt{(\frac{1}{2}h\omega_0)^2 - \epsilon^2}$. When we add damping [as in (2.1)], the proportionality constant with respect to the lab

¹Alternatively, the first term would satisfy a degenerate “resonance” condition if and only if $\omega_p = 0$, which means no parametric variation in the first place.

²Consistent with Floquet theory [37], the response will also have Fourier components at frequencies $(2n+1)(\omega_p + \frac{1}{2}\epsilon)$ for nonzero n , but it can be shown that the amplitudes of these components are very small in the steady state. For example, the leading third-harmonic correction at frequency $3(\omega_0 + \frac{1}{2}\epsilon)$ is smaller in amplitude by a factor of $h/16$ from the fundamental harmonic response [33].

frame dynamical variable x becomes $e^{(s-\gamma)t}$. We therefore see that to a good approximation the parametric oscillation manifests itself as an effective negative damping constant that competes with (and if large enough can overcome) the natural damping of the system.

To roughly see how parametric resonance can be utilized for amplification, consider adding an external driving term to the system

$$\ddot{x} + 2\gamma\dot{x} + \omega^2(t)x = \frac{F_0}{m} \cos(\omega_d t), \quad (2.6)$$

and then (naively) approximate the effect of the parametric oscillation as a modification of the damping term of a non-modulated resonator,

$$\ddot{x} + 2(\gamma - s)\dot{x} + \omega_0^2 x = \frac{F_0}{m} \cos(\omega_d t). \quad (2.7)$$

If the parametric oscillation strength h is such that the effective damping constant $\gamma - s$ is still positive but small, then from the study of the forced damped harmonic oscillator of freshman physics [36], the resulting steady-state amplitude of oscillation at frequency ω_1 is

$$a = \frac{F_0}{m} \frac{1}{\sqrt{(\omega_d^2 - \omega_0^2)^2 + (2[\gamma - s]\omega_d)^2}}, \quad (2.8)$$

showing a Lorentzian resonance near $\omega_d = \omega_0$ with a maximum amplitude proportional to $1/(\gamma - s)$. For strong enough parametric oscillation, s can approach γ and yield a large parametrically amplified steady-state response, and if s is large enough to overcome γ , the system response will continue to increase in amplitude (even without an explicit driving term, as discussed above). This is by no means an exact solution, and is only meant to give an intuition behind the origins of parametric gain (a rigorous treatment of the quantum case will be given later).

Such an amplification scheme has several advantages. It can easily be made very sensitive while simultaneously having a low level of noise, assuming one can pump the parameter $\omega(t)$ in a low-noise manner, and that a reactive rather than resistive parameter is made to oscillate. This can for example be done inductively or with an electromagnetic drive. This pump tone (i.e., the signal that modulates the system parameters) is ultimately what provides the energy for the amplification of signals. Besides forming a natural cryogenically-operable parametric amplifier, we will see through a quantum mechanical treatment that the parametric amplifier implemented in this thesis in fact theoretically adds the minimum amount of noise allowed by quantum mechanics, allowing for example signals at the one-photon level and for signal-to-noise ratios to overcome the limitations of commercial HEMT

amplifiers. In addition, when operated in the quantum regime, such an amplifier can let us access some very interesting quantum phenomena, such as squeezing.

2.2 Parametric Amplification with a Quantum Duffing Oscillator

How can we make a parametric amplifier (paramp³ for short) for microwave signals in cQED? A practical way to achieve parametric amplification is by employing a nonlinear oscillator, which can have a bifurcation point near which the resonator response depends very strongly on the input [21]. By perturbing a strong pump signal sent into such a nonlinear cavity, one can achieve parametric amplification. If we pursue this practical method, the question then becomes how to create such a nonlinear quantum oscillator. As we will see in detail in Chapter 3, the effect of embedding Josephson junctions in a coplanar waveguide resonator is to give rise to a nonlinear resonator that can be treated quantum-mechanically under experimental conditions. Before delving into this specific implementation, we study the general theory of parametric amplification with a quantum Duffing oscillator, which will allow us to use the powerful technique of input-output theory from quantum optics to describe how we can send input microwave signals to such a resonator and receive amplified output signals. Input-output theory also provides a straightforward way to include both linear and nonlinear loss, as well as other general nonlinearities⁴. Finally, as already mentioned, a fully quantum treatment will allow us to see that such amplifiers are quantum-limited, in principle yielding the least amount of noise allowable by the quantum-mechanical uncertainty principle. For these reasons, we will study parametric amplification in its general quantum context, allowing us to derive among other things expressions for the bandwidth and gain of a parametric amplifier derived from a general class of nonlinear effects.

The Hamiltonian of the quantum Duffing oscillator follows naturally from its classical counterpart. We start with the classical Duffing oscillator Hamiltonian

$$\mathcal{H}(q, p) = \frac{p^2}{2m} + \frac{1}{2}m\omega_0^2 q^2 + \frac{1}{4}\beta q^4, \quad (2.9)$$

and convert the first two terms into a quantum Hamiltonian using the standard method of annihilation and creation operators (which we will denote by A and A^\dagger) studied in

³We will often use this abbreviation for brevity, even though “para-amp” may be more logical.

⁴In particular, it allows us to include the nonlinear kinetic inductance of the superconducting transmission line itself, although we will see that such nonlinearities are negligible in our parametric amplifier.

introductory quantum mechanics in the context of the simple harmonic oscillator. For the third term, we use the fact that $q \propto (A + A^\dagger)$ to obtain the quantum Duffing Hamiltonian operator

$$\begin{aligned} H_{\text{Kerr}} &= \hbar\omega_0 A^\dagger A + \hbar \frac{K}{12} (A + A^\dagger)^4 \\ &\approx \hbar\omega_0 A^\dagger A + \hbar \frac{K}{2} (A^\dagger)^2 A^2, \end{aligned} \quad (2.10)$$

where in the second equality we have dropped rapidly oscillating terms whose net time-averaged effect is zero in the rotating wave approximation. Seen in another way, we can drop these terms provided $K\langle A^\dagger A \rangle$ isn't large compared with ω_0 , because they represent non-energy-conserving processes with an unbalanced number of photon creations and annihilations. With the normalization chosen as above, K is usually referred to as the “Kerr constant,” by analogy to the classical nonlinear Kerr effect in which a material has an electric field-dependent index of refraction $n = n_0 + n_2 E^2$ [38].

2.2.1 Input-Output Theory

Suppose we have a quantum Kerr oscillator. To utilize such an oscillator (which we will often refer to as the cavity) as an amplifier, we need to couple it to the outside world – in particular via an open port coupling the oscillator to a microwave transmission line. But before specializing to the case of a coupling capacitor, we consider the general case of a single cavity mode interacting with an external bosonic field, and derive the relation between input and output signals to and from the cavity mediated by this field. To do this, we will use the method of *input-output theory* developed in chapter 7 of [39]. Namely, we will model the transmission line used to drive the cavity by a collection of harmonic oscillators $b(\omega)$, and describe the signals we send into and out of the cavity by traveling wave combinations $a_{\text{in}}(\omega)$ and $a_{\text{out}}(\omega)$ of these transmission line modes. We will then extend this method to account for the leakage of energy from the cavity through other ports as well to account for possible damping of the system. In particular, our model will yield a coupling rate γ_1 between the transmission line and cavity, and will assume a linear loss port with coupling γ_2 (what this means will be described shortly). If desired, the reader may skip to the main results of this section [(2.23) and (2.25)], which make sense in the context of the schematic in Figure 2.1].

Following [39], we break up the total Hamiltonian into the sum

$$H = H_{\text{Kerr}} + H_{\text{bath}} + H_{\text{int}}, \quad (2.11)$$

where H_{bath} is the Hamiltonian of the external field and H_{int} describes the coupling between the Kerr cavity and external fields. We decompose this field into its component bosonic modes, whose annihilation operators we denote by $b(\omega)$. Technically, when an open port is present, the harmonic modes of the joint system are not strictly A and $b(\omega)$, but this model is accurate when the quality factor of the system is much greater than unity [17] (our system will have $Q \gtrsim 100$). We then have an infinite bath of harmonic oscillators with (dropping the zero-point energy for now)

$$H_{\text{bath}} = \int \hbar \omega b^\dagger(\omega) b(\omega) d\omega. \quad (2.12)$$

This continuum decomposition is valid in the limit of an infinitely long transmission line bath⁵. We posit that the interaction Hamiltonian consists of terms representing the swapping of excitations between the cavity mode and each external mode with a rate proportional to a coupling factor⁶ $f(\omega)$,

$$H_{\text{int}} = i\hbar \int_{-\infty}^{\infty} \left[f(\omega) b(\omega) A^\dagger - f^*(\omega) A b^\dagger(\omega) \right] d\omega. \quad (2.13)$$

Physically, the lower limit of integration should be $\omega = 0$, but since most of the weight of the integral will occur near the resonance frequency of our system (which is large compared to the couplings and therefore the characteristic bandwidth) it is a good approximation to extend the lower limit to $\omega = -\infty$. We proceed first by solving for the time evolution of $b(\omega)$. Using the standard bosonic commutation relations

$$[b(\omega), b^\dagger(\omega')] = \delta(\omega - \omega') \quad (2.14)$$

and the basic operator identity

$$[AB, C] = A[B, C] + [A, C]B, \quad (2.15)$$

we obtain the Heisenberg equation of motion

$$\dot{b}_t(\omega) = \frac{i}{\hbar} [H, b_t(\omega)] = -i\omega b_t(\omega) + f^*(\omega) A(t), \quad (2.16)$$

where the subscript on $b_t(\omega)$ explicitly denotes time dependence. Following the approach of Collett and Gardiner [40, 41], we integrate this ordinary differential equation to obtain

⁵The spectral density of modes is implicit in our definition rather than explicitly kept track of.

⁶We make the rotating wave approximation here to ignore terms proportional to $Ab(\omega)$ and $A^\dagger b^\dagger(\omega)$, which are present in the most general linear coupling between cavity and bath modes.

the solution

$$b_t(w) = e^{-i\omega(t-t_0)}b_0(\omega) + f^*(\omega) \int_{t_0}^t e^{-i\omega(t-t')}A(t')dt', \quad (2.17)$$

where the first term represents free evolution of the bath and the second term represents waves emitted from the cavity into the bath. We choose $t_0 < t$ to be an arbitrary time in the distant past when the input signals we care about have yet to be sent to the cavity. We use this solution to solve for the time evolution of our cavity mode A :

$$\begin{aligned} \frac{dA}{dt} &= \frac{i}{\hbar} [H, A(t)] = \frac{i}{\hbar} [H_{\text{Kerr}}, A(t)] - \int_{-\infty}^{\infty} f(w)b_t(\omega)d\omega \\ &= \frac{i}{\hbar} [H_{\text{Kerr}}, A(t)] - \int_{-\infty}^{\infty} f(\omega)e^{-i\omega(t-t_0)}b_0(\omega)d\omega - \int_{t_0}^t A(t') \int_{-\infty}^{\infty} |f(\omega)|^2 e^{-i\omega(t-t')}d\omega dt', \end{aligned} \quad (2.18)$$

where we have interchanged the time and frequency integrations in the final term. Following [39], we make a partial Markov approximation by treating $f(\omega)$ to be a constant f over a band of frequencies close to the characteristic resonance frequency of the system, which as mentioned before is where the frequency integrals carry the most weight and is valid for our system containing a high- Q coupling capacitance. This allows the concept of an ‘input’ and ‘output’ mode to be of great utility. Namely, we define the input mode

$$a_{\text{in}}(t) \equiv \frac{1}{\sqrt{2\pi}} \int_{-\infty}^{\infty} e^{-i\omega(t-t_0)}b_0(\omega)d\omega, \quad (2.19)$$

which has the interpretation of a wave propagating towards the cavity⁷, for example in a transmission line, as it is simply the free (pre-interaction) evolution of the bath modes relative to the initial conditions at t_0 . Similarly, we can define the output mode

$$a_{\text{out}}(t) \equiv \frac{1}{\sqrt{2\pi}} \int_{-\infty}^{\infty} e^{-i\omega(t-t_1)}b_1(\omega)d\omega, \quad (2.20)$$

where $t_1 > t$ is a time in the future when our input signals are no longer interacting with the cavity. This operator is simply the (backwards) free evolution of the bath from the distant future, associated with a solution of the form (2.17) but with the integration performed from t to t_1 , and can therefore be interpreted as the outgoing signal. We note, importantly,

⁷Often in the literature, this mode is defined differing by a minus sign. The sign is inconsequential as long as it is kept track of, but can lead to errors otherwise (for example, some of the typographical errors in [42]). We attempt to give a careful treatment and avoid sign errors in this thesis, although some mistakes are likely to have been made here as well.

that these operators obey the necessary bosonic algebra. For example,

$$\begin{aligned}
[a_{\text{in}}(t), a_{\text{in}}^\dagger(t')] &= \frac{1}{2\pi} \int_{-\infty}^{\infty} \int_{-\infty}^{\infty} d\omega d\omega' e^{-i\omega(t-t_0)} e^{i\omega'(t'-t_0)} [b_0(\omega), b_0^\dagger(\omega')] \\
&= \frac{1}{2\pi} \int_{-\infty}^{\infty} \int_{-\infty}^{\infty} d\omega d\omega' e^{-i\omega(t-t_0)} e^{i\omega'(t'-t_0)} \delta(\omega - \omega') \\
&= \frac{1}{2\pi} \int_{-\infty}^{\infty} e^{-i\omega(t-t')} d\omega = \delta(t - t'),
\end{aligned} \tag{2.21}$$

where we have used (2.14) and the inverse Fourier transform of the Dirac delta distribution. Defining⁸

$$\gamma \equiv \pi f^2, \tag{2.22}$$

using our Markov approximation and Fourier analysis we can rewrite (2.18) as

$$\begin{aligned}
\frac{dA}{dt} &= \frac{i}{\hbar} [H_{\text{Kerr}}, A(t)] - f \int_{-\infty}^{\infty} e^{-i\omega(t-t_0)} b_0(\omega) d\omega - f^2 \int_{t_0}^t \int_{-\infty}^{\infty} e^{-i\omega(t-t')} A(t') d\omega dt' \\
&= \frac{i}{\hbar} [H_{\text{Kerr}}, A(t)] - \sqrt{2\gamma} a_{\text{in}} - f^2 \int_{t_0}^t A(t') 2\pi \delta(t - t') dt' \\
&= \frac{i}{\hbar} [H_{\text{Kerr}}, A(t)] - \sqrt{2\gamma} a_{\text{in}}(t) - \gamma A(t),
\end{aligned} \tag{2.23}$$

a quantum stochastic Langevin equation for the intra-cavity field in which the Markovian approximation has manifested itself as a linear damping term that depends only on the state of the system at time t and not at previous times⁹¹⁰. We can similarly obtain an

⁸For future convenience, we uniformly redefine the phase of the relevant modes so that $f = |f|$ is real within the band of the Markov approximation. Also note that the definition of γ in the literature is sometimes defined to be twice as large. In this thesis, we will sometimes use $\kappa = 2\gamma$ to denote this (we will see later that this is the difference between the full width at half maximum [FWHM] and half width at half maximum [HWHM] of the associated resonance peak).

⁹Note the factor of $1/2$ that arises in the final term due to the one-sided integral with an upper limit exactly at the spike of the δ kernel. This can be intuitively understood by thinking of the δ kernel as a limit of integrals of half of a Gaussian curve. Although we have been somewhat haphazard with our manipulation of the Dirac delta distribution. For a rigorous yet accessible introduction to the theory of distributions, see [43].

¹⁰We should pause and note that despite the apparent discrepancy, the units in this equation of motion are consistent. From the fact that the Hamiltonian must have units of energy, using “[ω]” as a shorthand for “angular frequency” we see from (2.12) that $b(\omega)$ has units of [ω]^{-1/2}, so that since A is unitless, (2.13) implies that f has units of [ω]^{1/2} and therefore γ has units of [ω]. Finally, from our definition (2.19), a_{in} has units of [ω]^{1/2}. The asymmetry of units between A and a_{in} derives both from convention and the fact that our cavity has discrete modes whereas we model the transmission line bath as a continuum of modes.

equation of motion involving a_{out} ,

$$\frac{dA}{dt} = \frac{i}{\hbar}[H_{\text{Kerr}}, A(t)] - \sqrt{2\gamma}a_{\text{out}}(t) + \gamma A(t). \quad (2.24)$$

Subtracting (2.24) from (2.23) then yields the main result of this section,

$$a_{\text{out}}(t) - a_{\text{in}}(t) = \sqrt{2\gamma}A(t), \quad (2.25)$$

which together with (2.23) will allow us to calculate the cavity output as a function of the cavity input and cavity parameters.

2.2.2 Pumping the Oscillator

We now have the tools necessary to understand the parametric amplification of inputs to a Kerr cavity. We model the cavity as being coupled to *two* ports, one capacitively coupled to an input/output port and one to a linear dissipation port, which models the loss of energy from the imperfect cavity to the environment¹¹. We label the traveling wave modes of the input/output port as a_1 and those of the linear loss port as a_2 , with couplings to the cavity of γ_1 and γ_2 respectively as schematically illustrated in Figure 2.1.

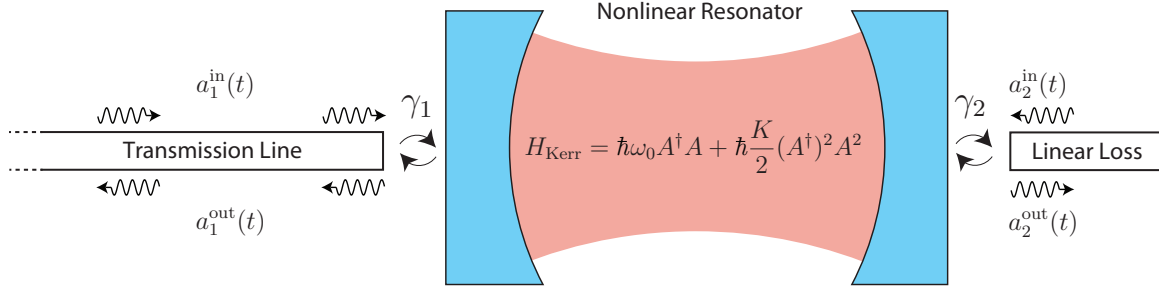


Figure 2.1 Pumping a nonlinear Kerr cavity with a single “pump” tone. γ_1 is the coupling strength associated with the port connecting to the main input/output transmission line, while γ_2 represents a coupling strength associated with an effective port representing linear loss. The intra-cavity field obeys the bare Kerr Hamiltonian in the absence of these couplings.

¹¹More generally, there could be a nonlinear dissipation port through which a bath couples to A^2 rather than A . Such ports are usually negligible, but we will later quote a modification of our result to account for this.

Upon evaluating the commutator

$$\begin{aligned} [H_{\text{Kerr}}, A] &= \hbar\omega_0[A^\dagger A, A] + \hbar\frac{K}{2}[(A^\dagger)^2 A^2, A] = \hbar\omega_0[A^\dagger, A]A + \hbar\frac{K}{2}[A^\dagger A^\dagger, A]AA \\ &= -\hbar\omega_0 A - \hbar K A^\dagger AA \end{aligned} \quad (2.26)$$

the Langevin equation (2.23) with two independent sets of coupled bath modes yields

$$\frac{dA}{dt} = -i\omega_0 A - iK A^\dagger AA - \sqrt{2\gamma_1} a_1^{\text{in}} - \sqrt{2\gamma_2} a_2^{\text{in}} - (\gamma_1 + \gamma_2)A, \quad (2.27)$$

and (2.25) yields the boundary conditions

$$a_1^{\text{out}}(t) - a_1^{\text{in}}(t) = \sqrt{2\gamma_1} A(t), \quad (2.28a)$$

$$a_2^{\text{out}}(t) - a_2^{\text{in}}(t) = \sqrt{2\gamma_2} A(t). \quad (2.28b)$$

To utilize the cavity as a parametric amplifier, we need to input a strong classical pump tone, which will provide the energy (and oscillating parameter) for the parametric gain of small input signals. That is, the amplification scheme involves inputting a pump plus small signal perturbation,

$$a_1^{\text{in}} = a_1^{\text{in,p}} + a_1^{\text{in,s}}. \quad (2.29)$$

We will follow the analysis of [21] by first calculating the cavity response to the classical pump, and afterwards treating the signal as a perturbation. We write the incoming pump (assumed to be in the coherent limit¹²) as

$$a_1^{\text{in,p}} = b_1^{\text{in}} e^{-i(\omega_p t + \phi_p)}, \quad (2.30)$$

where b_1^{in} is a real constant, and the reflected signal as

$$a_1^{\text{out,p}} = b_1^{\text{out}} e^{-i(\omega_p t + \phi_p)}, \quad (2.31)$$

where b_1^{out} is in general complex. Analogously to the case of a classical Duffing oscillator [34],

¹²As studied in quantum optics, a coherent state is the classical limit of a sinusoidal drive, consisting of an infinite sum of all Fock number states. The amplitude-phase uncertainty product of such a state is the minimum possible for the harmonic oscillator. The expectation value rotates clockwise about the origin of the $\text{Re}[a]$, $\text{Im}[a]$ plane and the “wavepacket” in this phase space is very localized for mean photon number $n \gg 1$, allowing the state to be treated as a complex number proportional to $e^{-i\omega t}$.

we posit¹³ a steady-state zeroth-order response of A in the form

$$A = B e^{-i(\omega_p t + \phi_B)}, \quad (2.32)$$

where B is real and ϕ_B encodes the internal cavity phase response. Note that we are treating the pump mode solution operators as commuting c-numbers, when in reality the steady state response is something more like a harmonic oscillator coherent state. Plugging these three equations into (2.27) and (2.28a) in the absence of signal and noise, we obtain respectively

$$[i(\omega_0 - \omega_p) + \gamma_1 + \gamma_2]B + iKB^3 = -\sqrt{2\gamma_1}b_1^{\text{in}}e^{i(\phi_B - \phi_p)} \quad (2.33)$$

and

$$b_1^{\text{out}} = b_1^{\text{in}} + \sqrt{2\gamma_1}B e^{-i(\phi_B - \phi_p)}. \quad (2.34)$$

In the special case of a linear cavity with no Kerr term (or for sufficiently low drive powers with a nonlinear cavity, such as the black curves in Figure 2.2), we can analytically solve for the output in terms of the input by combining (2.33) and (2.34) with $K = 0$, obtaining a reflection coefficient of

$$\begin{aligned} \Gamma &\equiv \frac{b_1^{\text{out}}}{b_1^{\text{in}}} = 1 - \frac{2\gamma_1}{i(\omega_0 - \omega_p) + \gamma_1 + \gamma_2} = \frac{\gamma_2 - \gamma_1 + i(\omega_0 - \omega_p)}{\gamma_1 + \gamma_2 + i(\omega_0 - \omega_p)} \\ &\equiv \frac{\Gamma_0 - 2iQ\frac{\delta\omega}{\omega_0}}{1 - 2iQ\frac{\delta\omega}{\omega_0}}, \end{aligned} \quad (2.35)$$

where $\delta\omega \equiv \omega_p - \omega_0$, Q is the loaded quality factor

$$\frac{1}{Q} = \frac{1}{Q_{\text{ext}}} + \frac{1}{Q_{\text{int}}} \equiv \frac{2\gamma_1}{\omega_0} + \frac{2\gamma_2}{\omega_0} \quad (2.36)$$

¹³We are ignoring the possibility exciting higher harmonics characteristic of the response of nonlinear oscillators – in our fundamental assumption of the Kerr Hamiltonian (2.10), we have ignored potential cross-Kerr terms (of the form $\hbar K_{ij} A_i^\dagger A_i A_j^\dagger A_j$) that may weakly couple to higher modes of the cavity, and also in our rotating wave approximation we have ignored a small third harmonic contribution to the pump solution. This is ignored in [15, 21], although it is usually discussed in treatments of the classical Duffing oscillator [34, 42]. We should make sure that our single-harmonic zeroth-order pump response is accurate. To do so, note that adding a term of order $\hbar \frac{K}{2} A^3$ to (2.27), plugging in the zeroth-order solution (2.32), and then integrating to obtain a more accurate solution yields a term of order $\frac{K}{2} B^3 e^{-i(3\omega_p t + 3\phi_B)}$, which will be small compared to the zeroth-order solution when $\frac{K}{\omega_p} B^2 \ll 1$. As we will see, in our implementation $K/\omega_p \approx 10^{-6}$ to 10^{-5} , and we will operate at photon numbers B^2 less than the so-called critical number (2.46) of order 10^3 in a cQED implementation. We can therefore treat the zeroth-order classical pump solution (2.32) as accurate.

and

$$\Gamma_0 = \frac{\gamma_2 - \gamma_1}{\gamma_1 + \gamma_2} \quad (2.37)$$

is the reflection coefficient on resonance. Note that being on resonance yields the minimum amount of reflected signal, as

$$|\Gamma| = \frac{\Gamma_0^2 + 4Q^2 \left(\frac{\delta\omega}{\omega_0}\right)^2}{1 + 4Q^2 \left(\frac{\delta\omega}{\omega_0}\right)^2}. \quad (2.38)$$

In particular, in the limit $\gamma_1 = \gamma_2$, we have $\Gamma_0 = 0$ indicating full leakage of the input signal through the linear loss port, analogous to the full transmission of a standard cQED two-port $\lambda/2$ resonator on resonance. But in the limit $\gamma_1 \gg \gamma_2$ (which is the case for our paramp), $\Gamma_0 \approx 1$, meaning that nearly all information about the resonance is contained in the reflected phase rather than in the reflected amplitude. In either case, $\Gamma \rightarrow 1$ as ω_p is detuned far from ω_0 relative to the linewidth, $\gamma_1 + \gamma_2$.

Returning to the general case of $K \neq 0$, we follow [21] by taking the magnitude of both sides of (2.33) and defining the cavity pump photon number

$$N \equiv B^2, \quad (2.39)$$

obtaining the following cubic equation for N ,

$$K^2 N^3 + 2(\omega_0 - \omega_p)KN^2 + [(\omega_0 - \omega_p)^2 + (\gamma_1 + \gamma_2)^2]N = 2\gamma_1 (b_1^{\text{in}})^2. \quad (2.40)$$

We can also obtain an equation for the phase of the steady-state internal pump field relative to the input pump field using equation (2.33) and Euler's formula,

$$\tan(\phi_B - \phi_p) = \frac{(w_0 + KN) - w_p}{\gamma_1 + \gamma_2}. \quad (2.41)$$

Note that this phase response is nonlinear, depending the internal field amplitude N . We have grouped this N -dependent term together with ω_0 so that it can be interpreted as a power-dependent shift KN of the resonance frequency of the cavity. For negative K (which as we will see is the case in our implementation), the cavity resonance is pulled downward in frequency with increasing pump power. The expression KN for this shift also coincides with the point of the maximum intracavity response N , as is easily verified by solving for $\partial N / \partial \omega_p = 0$ in (2.40). Equation (2.40) can be numerically solved for the steady-state amplitude of the internal pump field. There are two possible regimes for this polynomial equation; either there exist three real solutions for N , or there exist one real solution and

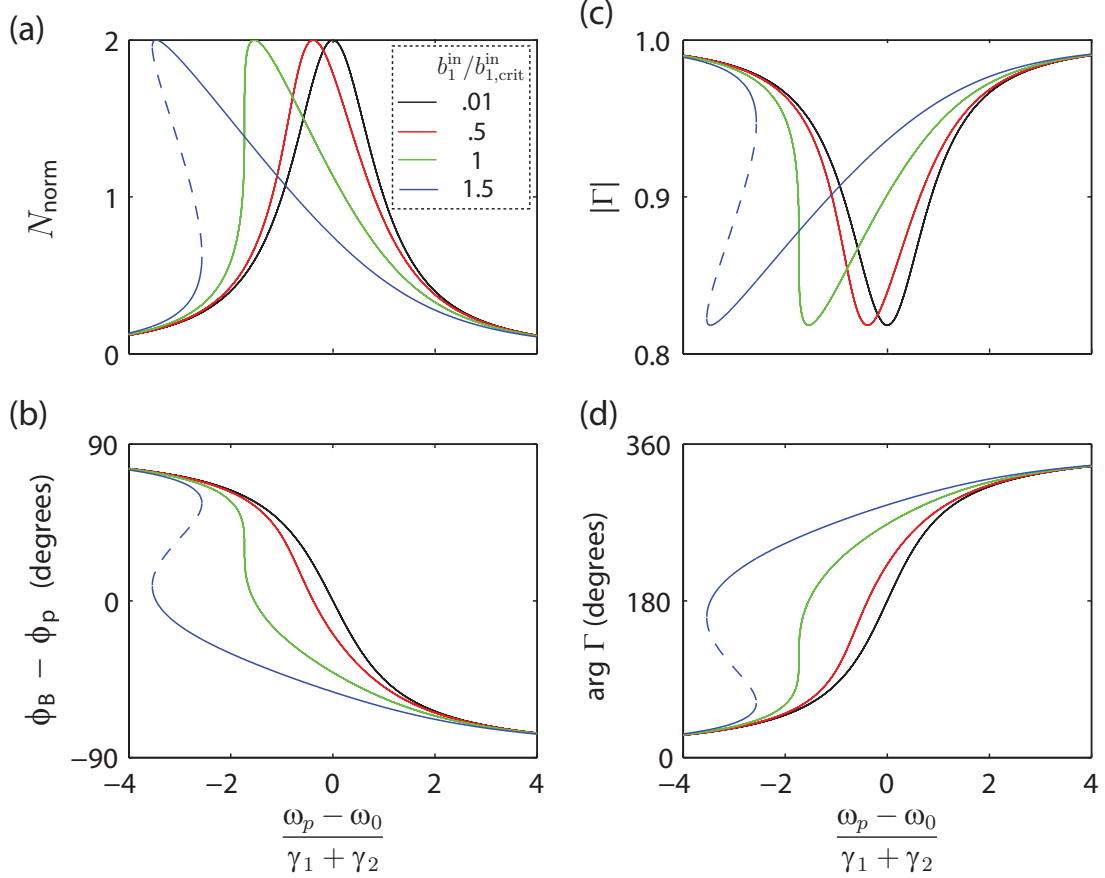


Figure 2.2 MATLAB plots of system response to a single pump input tone as a function of frequency (in units of linewidths) with $K = -10^{-5}\omega_0$ and $\gamma_2 = .1\gamma_1$, for drive amplitudes b_1^{in} equal to $.01b_{1,\text{crit}}^{\text{in}}$ (black), $.5b_{1,\text{crit}}^{\text{in}}$ (red), $b_{1,\text{crit}}^{\text{in}}$ (green), and $1.5b_{1,\text{crit}}^{\text{in}}$ (blue). For strong drives $b_1^{\text{in}} > b_{1,\text{crit}}^{\text{in}}$, dashed lines in the bistable regime indicate the unstable solution. (a) Intracavity pump response N_{norm} [N normalized by $\frac{(\gamma_1 + \gamma_2)^2}{\gamma_1}(b_1^{\text{in}})^2$]. The actual (unnormalized) response of course increases in maximum amplitude in addition to having a distorted shape. (b) Intracavity phase response. (c) Magnitude of the reflection coefficient. (d) Phase of the reflection coefficient.

two complex solutions. In the latter case, we take the real solution to be the physical one. In the former case, it can be shown that two of the solutions will be stable, while one will be unstable, leading to the feature of bistability [21]. We can obtain some intuition behind this by plotting the behavior of the pump solution at different strengths of incident b_1^{in} as a function of frequency. The response is that of a driven Duffing oscillator (which we have arrived at in the Fourier domain). Figure 2.2 contains MATLAB plots¹⁴ of the theoretical pump solutions we have just calculated. The left column depicts the steady-state

¹⁴The MATLAB function “roots” is quite useful in solving for the pump response in all regimes.

intracavity amplitude and phase, while the right column depicts the amplitude and phase of the reflected signal. Note that the system resonance is pulled downward in frequency, as expected for a negative value of K . We would like to operate our parametric amplifier with a pump power slightly below the critical input power, so that the system will be sensitive to small perturbations but not yet bistable. The bistable regime in which there are two stable solutions occurs above this bifurcation point. Although we will not operate at such powers, this bistable regime has been successfully used to create sensitive “Josephson bifurcation amplifiers” [20, 44–46].

We can calculate the critical point at which the distorted Lorentzian response transitions into the bistable regime; i.e., when the slope of the response first becomes vertical as the system transitions into the bistable regime, as in the green curves in Figure 2.2. There are two conditions that are satisfied at this point. One is that the slope $\partial N/\partial\omega_p$ diverges, or rather $\partial\omega_p/\partial N = 0$. Well, differentiating (2.40) with respect to N and collecting the terms involving $\partial\omega_p/\partial N$ yields

$$\frac{\partial\omega_p}{\partial N} [2KN^2 + 2N(\omega_o - \omega_p)] = 3K^2N^2 + 4KN(\omega_0 - \omega_p) + (\omega_0 - \omega_p)^2 + (\gamma_1 + \gamma_2)^2, \quad (2.42)$$

which means (completing the square on the right-hand side) that the critical point occurs when

$$(\omega_0 - \omega_p + 2KN)^2 - K^2N^2 + (\gamma_1 + \gamma_2)^2 = 0. \quad (2.43)$$

In the bistable regime, this will be satisfied at two pump frequencies. The critical point occurs when these two points coincide, which will happen when in addition $\partial^2\omega_p/\partial N^2 = 0$. Differentiating both sides of (2.42) using the product rule and setting $\partial\omega_p/\partial N$ to zero, we obtain the additional condition

$$6K^2N + 4K(\omega_0 - \omega_p) = 0. \quad (2.44)$$

Combining these equations then yields the critical values of ω_p and N ,

$$\omega_{p,\text{crit}} = \omega_0 + \sqrt{3} \frac{K}{|K|} (\gamma_1 + \gamma_2) \quad (2.45)$$

and

$$N_{\text{crit}} = \frac{2}{\sqrt{3}} \frac{\gamma_1 + \gamma_2}{|K|}. \quad (2.46)$$

We will also find it useful to calculate [using (2.40) along with (2.45) and (2.46)] the input

power corresponding to the critical intracavity field,

$$(b_{1,\text{crit}}^{\text{in}})^2 = \frac{4}{3\sqrt{3}} \frac{(\gamma_1 + \gamma_2)^3}{\gamma_1 |K|}. \quad (2.47)$$

2.2.3 Parametric Amplification of Small Perturbations

We are finally ready to calculate the parametric amplification of small signals. Intuitively, if the pump is operated near the critical point, small perturbations will lead to a relatively large change in the system's response. Suppose a small signal $a_1^{\text{in},s} = c_1(t)^{\text{in}} e^{-i\omega_p t}$, with $|c_1^{\text{in}}| \ll |b_1^{\text{in}}|$. Here, c_1^{in} can be time-dependent – the factor of $e^{-i\omega_p t}$ is there simply for calculational convenience, allowing us to “peel off” the time-dependence of the pump and define c in a rotating frame (as we will explicitly see when we move into the Fourier domain). Our input mode now takes the form

$$a_1^{\text{in}}(t) = b_1^{\text{in}} e^{-i(\omega_p t + \phi_p)} + c_1^{\text{in}}(t) e^{-i\omega_p t}, \quad (2.48)$$

with the output and internal resonator modes taking the form

$$\begin{aligned} a_1^{\text{out}}(t) &= b_1^{\text{out}} e^{-i(\omega_p t + \phi_p)} + c_1^{\text{out}}(t) e^{-i\omega_p t} \\ A(t) &= B e^{-i(\omega_p t + \phi_B)} + c(t) e^{-i\omega_p t}, \end{aligned} \quad (2.49)$$

where b_1^{out} and B are the solutions to the classical unperturbed pump as derived above. This decomposition of input and output signals is illustrated schematically in Fig. 2.3. We

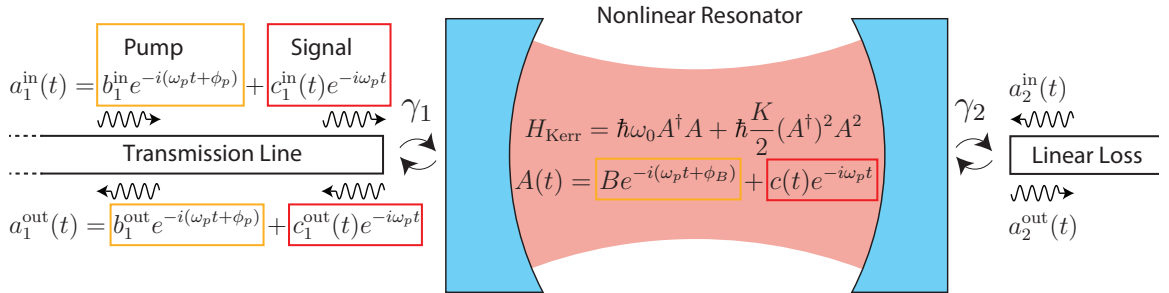


Figure 2.3 Illustration of input, output, and loss for a parametric amplifier based on a nonlinear Kerr oscillator. The main input-output port connecting to a transmission line is shown on the left, while an extra port representing linear loss to the environment (as described above) is shown on the right. The decomposition of the input/output signals into a large classical pump and small quantum signal is also illustrated.

assume that perturbations to the pump are small so that we can treat $c_1^{\text{in}}, c_1^{\text{out}}$, and c as perturbations to linear order, which can include both a small signal and also noise. To derive the behavior of the resonator as an amplifier of input signals, we will assume the input from the loss mode a_2^{in} is comparably small, so that plugging (2.48) and (2.49) into the Langevin equation of motion (2.27) and subtracting out the pump response from both sides [which still approximately obeys (2.33)] yields, after dropping all quadratic and cubic appearances of $c(t)$ (which is justified when $\langle c^\dagger c \rangle \ll N$), the linearized equation

$$-i\omega_p c(t) + \frac{dc}{dt} = -i\omega_0 c(t) - iK \left(c^\dagger(t) N e^{-2i\phi_B} + 2c(t)N \right) - \sqrt{2\gamma_1} c_1^{\text{in}}(t) - (\gamma_1 + \gamma_2)c(t). \quad (2.50)$$

Note that peeling off the $e^{-i\omega_p t}$ term from the signal allowed us to divide out a common factor of $e^{-i\omega_p t}$ in this equation. We then define the frequency-domain signals

$$\begin{aligned} c_1^{\text{in}}(\omega) &= \frac{1}{\sqrt{2\pi}} \int_{-\infty}^{\infty} dt c_1^{\text{in}}(t) e^{i\omega t} \\ c_1^{\text{out}}(\omega) &= \frac{1}{\sqrt{2\pi}} \int_{-\infty}^{\infty} dt c_1^{\text{out}}(t) e^{i\omega t} \\ c(\omega) &= \frac{1}{\sqrt{2\pi}} \int_{-\infty}^{\infty} dt c(t) e^{i\omega t} \end{aligned} \quad (2.51)$$

in the rotating frame of the pump. It is important to remember this: because of how we have defined the signal term in (2.49), ω refers to the frequency *relative to the pump frequency*; that is, the physical signal has a frequency of $\omega_p + \omega$. Using the basic properties of the Fourier transform (in particular, how it acts on time-derivatives and under complex conjugation), we obtain after Fourier-transforming and rearranging (2.50)

$$i[(\omega_0 - \omega_p) - \omega - i(\gamma_1 + \gamma_2) + 2KN]c(\omega) + iKN e^{-2i\phi_B} c^\dagger(-\omega) = -\sqrt{2\gamma_1} c_1^{\text{in}}(\omega). \quad (2.52)$$

Defining

$$W = i(\omega_0 - \omega_p) + (\gamma_1 + \gamma_2) + 2iKN \quad (2.53)$$

$$V = iKN e^{-2i\phi_B}, \quad (2.54)$$

(2.52) can be written as

$$(W - i\omega)c(\omega) + V c^\dagger(-\omega) = -\sqrt{2\gamma_1} c_1^{\text{in}}(\omega). \quad (2.55)$$

As is often the case with working in the frequency domain, a little algebraic manipulation can allow us to solve for the variable under question. In our case, we can solve for the perturbed internal cavity field $c(\omega)$ by using the complex conjugate version of (2.55) with $\omega \rightarrow -\omega$,

$$(W^* - i\omega)c^\dagger(-\omega) + V^*c(\omega) = -\sqrt{2\gamma_1}c_1^{\text{in}\dagger}(-\omega), \quad (2.56)$$

combined with (2.55) to yield the combined equation

$$(W - i\omega)c(\omega) + V \frac{\left(-\sqrt{2\gamma_1}c_1^{\text{in}\dagger}(-\omega) - V^*c(\omega)\right)}{W^* - i\omega} = -\sqrt{2\gamma_1}c_1^{\text{in}}(\omega), \quad (2.57)$$

which after collecting terms yields the solution

$$c(\omega) = \frac{-\sqrt{2\gamma_1} \left[(W^* - i\omega)c_1^{\text{in}}(\omega) - Vc_1^{\text{in}\dagger}(-\omega) \right]}{|W|^2 - 2\text{Re}[W]i\omega - \omega^2 - |V|^2}. \quad (2.58)$$

We will find it instructive to factor the denominator, which is simply a quadratic polynomial in the variable $x = i\omega$. The quadratic formula then gives the roots

$$\lambda_{\pm} = (\gamma_1 + \gamma_2) \pm \sqrt{K^2N^2 - (w_0 - w_p + 2KN)^2}, \quad (2.59)$$

where we have used the definitions (2.53) and (2.54). Thus, (2.58) becomes

$$c(\omega) = \frac{-\sqrt{2\gamma_1} \left[(W^* - i\omega)c_1^{\text{in}}(\omega) - Vc_1^{\text{in}\dagger}(-\omega) \right]}{(i\omega - \lambda_-)(i\omega - \lambda_+)}. \quad (2.60)$$

Finally, using this intra-cavity signal solution, we can calculate the cavity output c_1^{out} [as defined in (2.49)] in response to the perturbation via the input-output boundary condition (2.28a),

$$\begin{aligned} c_1^{\text{out}}(\omega) &= \left(1 - \frac{2\gamma_1(W^* - i\omega)}{(i\omega - \lambda_-)(i\omega - \lambda_+)}\right) c_1^{\text{in}}(\omega) + \frac{2\gamma_1V}{(i\omega - \lambda_-)(i\omega - \lambda_+)} c_1^{\text{in}\dagger}(-\omega) \\ &\equiv \mathcal{G}(\omega)c_1^{\text{in}}(\omega) + \mathcal{M}(\omega)c_1^{\text{in}\dagger}(-\omega). \end{aligned} \quad (2.61)$$

This result shows something very interesting: if the signal is incident on a pumped Kerr resonator with detuning ω from the pump, (2.61) implies that the reflected output will contain not only a frequency component at $\omega_p + \omega$, but also at $\omega_p - \omega$. In effect, the pumped nonlinear resonator couples the two symmetrically detuned modes via a mixing process. Note that the output signal at frequency $\omega_p - \omega$ only occurs when a Kerr nonlinearity is

present; i.e., $K \neq 0 \rightarrow V \neq 0$. We will refer to this tone as the “image” tone (or sometimes as the “intermodulation” tone).

Analogy to Classical Parametric Resonance

Before delving into the properties of the amplification we have just derived, we take a brief but enlightening aside in order to understand the correspondence between our result and conventional parametric resonance in the classical limit. In quantum optics, the term “parametric” generally refers to processes in which different frequencies of light are mixed via a nonlinear refractive medium [15, 39]. But if we put in a little effort, we can in fact see how our parametric amplifier formally maps onto a conventional classical driven parametric oscillator (2.6); i.e., an oscillator with a time-varying resonance frequency of the form (2.3) capable of exhibiting parametric resonance.

We can do this by temporarily returning to the time-domain (2.27) and temporarily considering the intracavity signal perturbation $\delta(t) \equiv c(t)e^{-i\omega_p t}$ in the laboratory frame. We will show that the equation of motion for $\delta(t)$ maps onto equation (2.6) in a certain classical limit. As in our derivation of the rotating-wave perturbation equation of motion (2.50), inserting the pump plus signal ansatz into (2.27) and subtracting out the pump response from both sides yields

$$\dot{\delta}(t) = -i\omega_0\delta(t) - iK[N\delta^\dagger(t)e^{-2i\omega_p t}e^{-2i\phi_B} + 2N\delta(t)] - \sqrt{2\gamma_1}\delta_1^{\text{in}}(t) - (\gamma_1 + \gamma_2)\delta(t). \quad (2.62)$$

Differentiating and then substituting this equation yields [using the shorthand definitions (2.53) and (2.54)]

$$\begin{aligned} \ddot{\delta}(t) + (W + i\omega_p)\dot{\delta}(t) + e^{-2i\omega_p t}V\dot{\delta}^\dagger(t) - 2i\omega_p V\delta^\dagger(t) &= -\sqrt{2\gamma_1}\dot{\delta}_1^{\text{in}}(t) \\ \Rightarrow \ddot{\delta}(t) + (W + i\omega_p)\dot{\delta}(t) + V[-\sqrt{2\gamma_1}\dot{\delta}_1^{\text{in}}(t) - W^*\delta^\dagger(t) - V^*\delta(t)] &= -\sqrt{2\gamma_1}\dot{\delta}_1^{\text{in}}(t) \\ \Rightarrow \ddot{\delta}(t) + (W + i\omega_p)\dot{\delta}(t) + e^{-2i\omega_p t}V[-\sqrt{2\gamma_1}\dot{\delta}_1^{\text{in}\dagger}(t) - (W^* - i\omega_p)\delta^\dagger(t) - e^{2i\omega_p t}V^*\delta(t)] \\ &\quad - 2i\omega_p e^{-2i\omega_p t}V\delta^\dagger(t) = -\sqrt{2\gamma_1}\dot{\delta}_1^{\text{in}}(t) \\ \Rightarrow \ddot{\delta}(t) + (W + i\omega_p)\dot{\delta}(t) - e^{-2i\omega_p t}V\sqrt{2\gamma_1}\dot{\delta}_1^{\text{in}\dagger}(t) - (W^* - i\omega_p)[- \sqrt{2\gamma_1}\dot{\delta}_1^{\text{in}}(t) - \dot{\delta}(t) \\ &\quad - (W + i\omega_p)\delta(t)] - |V|^2\delta(t) - 2i\omega_p e^{-2i\omega_p t}V\delta^\dagger(t) = -\sqrt{2\gamma_1}\dot{\delta}_1^{\text{in}}(t) \\ \Rightarrow \ddot{\delta}(t) + 2\text{Re}[W + i\omega_p]\dot{\delta}(t) + \left[|W + i\omega_p|^2 - |V|^2 + 2K N\omega_p e^{-2i\omega_p t - 2i\phi_B}\right]\delta^\dagger(t) &= \Gamma(t), \end{aligned} \quad (2.63)$$

where $\Gamma(t)$ is an effective driving term for the intracavity perturbation field. If we make the classical approximation that $\delta(t)$ is a c-number and in fact real, then taking the real part

of this equation of motion and using the definitions of V and W yields

$$\frac{d^2\delta}{dt^2} + 2(\gamma_1 + \gamma_2)\frac{d\delta}{dt} + \omega_{\text{eff}}^2(N, t)\delta = \Gamma(t), \quad (2.64)$$

where, assuming $\omega_p/\omega_0 \approx 1$ and $K^2/\omega_0^2 \ll 1$ we have

$$\omega_{\text{eff}}^2(N, t) = \omega_0^2 \left(1 + (\gamma_1 + \gamma_2)^2 + \frac{4NK}{\omega_0} \right) \left[1 + \frac{2NK/\omega_0}{1 + (\gamma_1 + \gamma_2)^2 + 4NK/\omega_0} \cos(2\omega_p t + 2\phi_B) \right]. \quad (2.65)$$

This is precisely the form (2.6), with $\omega_0^2 (1 + (\gamma_1 + \gamma_2)^2 + 4NK/\omega_0)$ being the shifted natural frequency of a damped nonlinear oscillator as in (2.3)! [The damping arises from the coupling of the resonator through the input and loss ports γ_1 and γ_2 .] We can therefore say that in some sense, the strong pump acts to modulate the effective resonance frequency seen by a small perturbation, which is possible because of the nonlinear Kerr term. This provides energy to the perturbation when it is near parametric resonance. Along with our discussion in section 2.1, this gives a bit of intuition (however small) behind the amplifier gains we will now study.

Amplifier Gain and Bandwidth

Returning to our quantum mechanical result (2.61), we would like to understand the properties of our parametric amplifier based on a quantum Kerr oscillator. The bare minimum way of characterizing an amplifier is of course calculating its gain and bandwidth, which we will do presently. After this, we will characterize other important properties such as dynamic range and noise performance. We define the signal and image power gains

$$G_s(\omega) \equiv \frac{|c_1^{\text{out}}(\omega)|^2}{|c_1^{\text{in}}(\omega)|^2} = |\mathcal{G}(\omega)|^2 = \frac{|(i\omega - \lambda_-)(i\omega - \lambda_+) - 2\gamma_1(W^* - i\omega)|^2}{(\omega^2 + \lambda_-^2)(\omega^2 + \lambda_+^2)} \quad (2.66)$$

and

$$G_i(\omega) \equiv \frac{|c_1^{\text{out}}(-\omega)|^2}{|c_1^{\text{in}}(\omega)|^2} = |\mathcal{M}(\omega)|^2 = \frac{4\gamma_1^2|V|^2}{(\omega^2 + \lambda_-^2)(\omega^2 + \lambda_+^2)} \quad (2.67)$$

respectively. We see that the gains are highest when the signal frequency is close to the pump frequency, $\omega \approx 0$, and also when the cavity is driven close to its critical bifurcation point [at which point the denominator diverges, as can be seen from equation (2.43)]. As noted in [15, 42], the 3-dB bandwidth of this peak is of the order of the linewidths γ_1, γ_2 . Following [42], we can straightforwardly estimate this bandwidth, assuming the cavity is pumped close to (but not at) the bifurcation point discussed earlier. For $\omega \approx 0$, we can

approximate (2.66) and (2.67) as

$$G_s(\omega \approx 0) \approx G_i(\omega \approx 0) = G(\omega \approx 0) \approx \frac{4\gamma_1^2|V|^2}{\lambda_-^2\lambda_+^2 + (\lambda_-^2 + \lambda_+^2)\omega^2} \equiv \frac{G(0)}{1 + (\frac{2\omega}{B_\omega})^2}, \quad (2.68)$$

from which we can extract the 3-dB bandwidth

$$B_\omega = \frac{2}{\sqrt{G(0)}} \sqrt{\frac{4\gamma_1^2|V|^2}{\lambda_-^2 + \lambda_+^2}}. \quad (2.69)$$

Using equations (2.45) and (2.46) for the values of various parameters near the critical pumping point, we have $\lambda_+ \approx 2(\gamma_1 + 2\gamma_2)$ and $\lambda_- \approx 0$, so that (2.69) becomes in the near-critical limit

$$\begin{aligned} B_\omega &\approx \frac{2}{\sqrt{G(0)}} \sqrt{\frac{4\gamma_1^2 \cdot \frac{4}{3}(\gamma_1 + \gamma_2)^2}{4(\gamma_1 + \gamma_2)^2}} \\ &= \frac{4}{\sqrt{3}} \frac{\gamma_1}{\sqrt{G(0)}}. \end{aligned} \quad (2.70)$$

We see, as is usually the case with amplifiers, that there is a tradeoff between gain and bandwidth [in fact, we also see this in the classical case of parametric amplification via equation (2.8)]. This key result states more specifically that the gain-bandwidth product $\sqrt{G}B_\omega$ is proportional to γ_1 , the rate at which photons can leak out of the output port of the cavity (it is interesting to note that although γ_2 will broaden the resonance peak of the pump, it doesn't affect the bandwidth of amplification under our approximations). In other words, the bandwidth is roughly given by that of a Lorentzian with the same linewidth as the resonator, divided by \sqrt{G} . This is an important reason why implementing a parametric amplifier with SQUIDs is so appealing: as we will explicitly see later, tuning the frequencies of the SQUIDs embedded in the centerpin of a $\lambda/4$ resonator via magnetic flux allows one to tune the resonance frequency of the system, and therefore the amplified band. This is one approach to overcoming the small bandwidths that are characteristic of a large class of these amplifiers. Figure 2.4 shows MATLAB plots of the calculated gains, in which the gain-bandwidth tradeoff is visually apparent.

Dynamic Range

Even if we increase the cavity linewidth and compromise by decreasing the bandwidth, we cannot increase the gain indefinitely. The dynamic range of an amplifier refers to the range of amplified signal powers for which the device functions well as a linear amplifier. In our

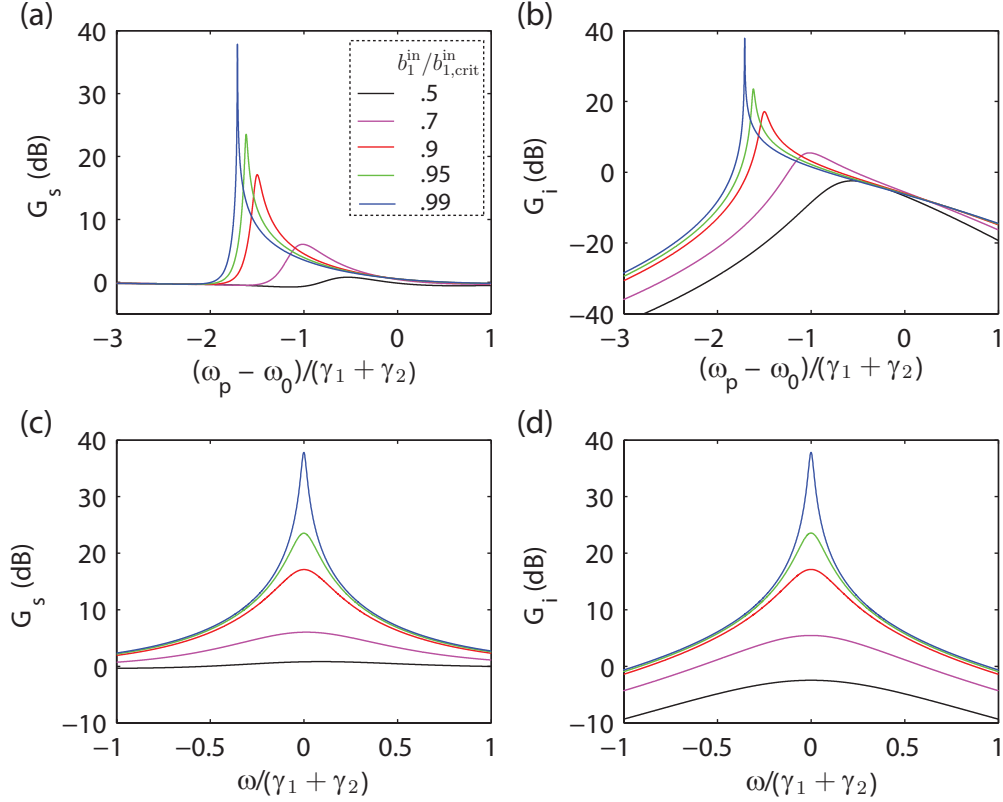


Figure 2.4 Theoretical signal and image gains (in logarithmic power units of decibels [dB]) with $K = -10^{-5}\omega_0$ and $\gamma_2 = .1\gamma_1$, for pump amplitudes b_1^{in} equal to $.5b_{1,\text{crit}}^{\text{in}}$ (black), $.7b_{1,\text{crit}}^{\text{in}}$ (purple), $.9b_{1,\text{crit}}^{\text{in}}$ (red), $.95b_{1,\text{crit}}^{\text{in}}$ (green), and $.99b_{1,\text{crit}}^{\text{in}}$ (blue). In (a) and (b), a signal frequency of $\omega = 0$ relative to the pump was used. In (c) and (d), the pump frequency for each drive power was chosen based on what gave the maximum gain in (a) and (b).

previous derivation, we assumed that the pump tone is “stiff” in that it is unchanged by any perturbing signals or quantum fluctuations, whereas in reality the pump is ultimately what supplies the energy for signal amplification in the first place and could in principle be depleted. This not only imposes a limit on the power of the input signal, but also imposes a limit on the power of the output signal and therefore on the dynamic range of the amplifier. At the very least, the amplifier must be able to function in the face of noise due to both quantum and thermal fluctuations at the input port. To be safe, heuristically we would want this amplified noise to be two orders of magnitude smaller than the pump power. We can roughly estimate the amplified vacuum noise from frequencies near the pump frequency

(ignoring γ_2) as

$$P_{\text{noise}} \approx \frac{\hbar\omega_p}{2} \int_{2B_\omega} G(0)df, \quad (2.71)$$

which for $\omega_p/2\pi = 6$ GHz, a power gain of 100 (i.e., 20 dB), and $\gamma_1/2\pi \approx 15$ MHz yields a rough value of -120 dBm, meaning that the critical power of the pump should at least be on the order of -100 dBm for such operating parameters. With this satisfied, it is then up to the user of the device to ensure that the signal input power is not an appreciable fraction of the pump power. In particular, when designing the amplifier, one should ensure that the critical pump input power $P_{\text{in,crit}} = \hbar\omega_p(b_{1,\text{crit}}^{\text{in}})^2$ is greater than this value. With these same parameters, by (2.47) this would require the Kerr constant $|K|/2\pi$ to be less than on the order of 100 KHz.

Quantum-Limited Noise Performance

In this section, we will arrive at a very important property of a parametric amplifier based on a quantum Kerr oscillator – at zero temperature, its added noise output is limited by quantum fluctuations to the minimum amount allowed by quantum mechanics. More precisely, besides just amplifying quantum (or classical) fluctuations at the input as briefly discussed above, any linear amplifier is required by quantum mechanics to add a certain minimum amount of extra noise to its output. We will show that the parametric amplifier theoretically reaches this limit. We first (non-rigorously) introduce the concept of a noise spectral density, which characterizes how much of a noise signal is contained in a region of frequency space. Intuitively, this number would be proportional to the measured output power if the output port was followed by a narrow bandpass filter centered on the frequency in question. Classically, the energy carried by a signal (such as a voltage) $x(t)$ in the time domain is proportional to $\int |x(t)|^2 dt$. By Parseval's theorem [47], this is equal to (modulo a factor of 2π depending on the convention used) $1/2\pi \int |\hat{x}(\omega)|^2 d\omega$, where $\hat{x}(\omega)$ denotes the Fourier transform of the signal. By the orthogonality of Fourier components, it makes sense to divide the total power into independent contributions from each frequency, which could be physically measured for example by a spectrum analyzer. Classically, we therefore identify the spectral density $S_{x,x}$ with $|\hat{x}|^2$, modulo a constant factor. Quantum mechanically, we can deduce a similar structure due to the orthogonality of (the continuum of) bath modes (although, the quantum mechanical spectral density is not in general real, making its interpretation a little more intricate). Namely, the energy of a given mode $a(\omega)$ is a multiple of $\hbar(\omega_p + \omega)$ determined by the thermal occupation. For bosonic modes each obeying a harmonic oscillator Hamiltonian, we use the Bose-Einstein distribution [48] to

deduce the symmetrized spectral density¹⁵ in the approximation $\omega_p + \omega \approx \omega_p$

$$\begin{aligned}\hbar\omega_p S_{a,a}(\omega) &= \hbar\omega_p \left\langle a^\dagger(\omega)a(\omega) + a(\omega)a^\dagger(\omega) \right\rangle = \hbar\omega_p \left\langle a^\dagger(\omega)a(\omega) + \frac{1}{2} \right\rangle \\ &= \hbar\omega_p \left(\frac{1}{e^{\hbar\omega_p/k_B T} - 1} + \frac{1}{2} \right) = \frac{\hbar\omega_p}{2} \coth \left(\frac{\hbar\omega_p}{2k_B T} \right).\end{aligned}\quad (2.72)$$

We can now calculate the added fluctuation noise at the output of our amplifier. Using (2.61), we have

$$S_{a_{\text{out}},a_{\text{out}}}(\omega) = G_s(\omega)S_{a_{\text{in}},a_{\text{in}}}(\omega) + G_i(\omega)S_{a_{\text{in}},a_{\text{in}}}(-\omega), \quad (2.73)$$

which shows that for a signal at ω , extra noise at the image frequency $-\omega$ will be generated in accordance with the general mixing properties of the parametric amplifier. Now, it can be shown that the signal and intermodulation gains of (2.66–2.67) satisfy [45]

$$G_s(\omega) = G_i(\omega) + 1. \quad (2.74)$$

The noise spectrum (2.73) then becomes

$$\begin{aligned}S_{a_{\text{out}},a_{\text{out}}} &= G_s(\omega)S_{a_{\text{in}},a_{\text{in}}}(\omega) + [G_s(\omega) - 1]S_{a_{\text{in}},a_{\text{in}}}(-\omega) \\ &= G_s(\omega) \left[S_{a_{\text{in}},a_{\text{in}}}(\omega) + \left(1 - \frac{1}{G_s(\omega)} \right) S_{a_{\text{in}},a_{\text{in}}}(-\omega) \right].\end{aligned}\quad (2.75)$$

So, interpreting the signal at ω as the signal and $S_{a_{\text{out}},a_{\text{out}}}(\omega)$ as the input noise, the *added* output noise will arise in the image channel, so that using (2.72) we obtain an added output noise spectral density for frequencies near the pump ($\omega \ll \gamma_1$), in units of $\hbar\omega_p$ and normalized by the gain,

$$A_N = \left[1 - \frac{1}{G(\omega)} \right] \frac{1}{2} \coth \left(\frac{\hbar\omega_p}{2k_B T} \right) \quad (2.76)$$

Note that in the limit $k_B T \ll \hbar\omega_p$, for large gains this approaches

$$A_N \rightarrow \frac{1}{2}, \quad (2.77)$$

¹⁵We can intuitively view this as the sum of the absorption and emission spectrum (respectively) of the mode of frequency ω , which is also equal to the expectation value of fluctuations of the harmonic oscillator energy as shown by the second equality. For a more rigorous treatment of quantum spectral densities based on correlation functions (which in quantum mechanics can be imaginary), see [49].

meaning that for large gains the parametric amplifier will always add half a quantum of noise (i.e., half a photon of energy $\hbar\omega_p$) at its output. Conversely, in the classical limit $k_B T \gg \hbar\omega_p$, we obtain the classical result $A_N \propto k_B T$.

We now show that this is in fact the best we can do; that is, this is the minimum amount of added noise allowed by quantum mechanics for *any* kind of phase-preserving, phase-insensitive amplifier (these terms will be defined shortly). This is a key reason why Josephson parametric amplifiers are so appealing in circuit QED experiments – they can be used to amplify signals such that quantum noise becomes even more important than the otherwise significant noise at later stages of commercial HEMT-based amplification. This fundamental limit is partially a consequence of the uncertainty principle for Hermitian operators on a Hilbert space [47,50] (along with the identification of physical observables with Hermitian operators in quantum theory): if A and B represent two self-adjoint observables, then

$$\sigma_A^2 \sigma_B^2 \geq \left(\frac{1}{2i} \langle [A, B] \rangle \right)^2. \quad (2.78)$$

To utilize this relation, we must connect the language of quantum mechanics to familiar laboratory microwave voltage signals. If the frequency of the input signal is close to the fundamental resonance of the cavity and far away from other resonances, we can model an ac drive by mapping the coherent classical signal onto a quantum operator given by¹⁶

$$V_s(t) = V_0(a_s(t) + a_s(t)^\dagger) \rightarrow V_0(a_s e^{-i\omega_s t} + a_s^\dagger e^{i\omega_s t}) \quad (2.79)$$

where V_0 represents the amplitude of the signal. We can rewrite this as

$$V_s(t) = 2V_0 (X_1 \cos(\omega_s t) + X_2 \sin(\omega_s t)), \quad (2.80)$$

where

$$X_1 = \frac{a_s + a_s^\dagger}{2}, \quad X_2 = \frac{a_s - a_s^\dagger}{2i} \quad (2.81)$$

are identified as quadrature operators. These two operators are Hermitian and therefore observable, and represent the amplitude of each of the two quadratures of a classical signal oscillating 90° out of phase from each other, just like the quadratures that can be measured or manipulated by a microwave IQ mixer. Signal modulation (on timescales long compared with $2\pi/\omega_s$) is achieved by varying X_1 and X_2 . But as quantum mechanical

¹⁶We use the electric field phase convention of (B.10), which we take to be proportional to the voltage operator. Note that we use the trajectories of $a_s(t)$ and $a_s(t)^\dagger$ in the coherent limit and explicitly include the time-dependence. We also use a and a^\dagger as shorthands for $a_s(0)$ and $a_s^\dagger(0)$ respectively.

operators, these variables do not commute. Using the commutation relations for a and a^\dagger we straightforwardly calculate

$$[X_1, X_2] = \frac{i}{2}, \quad (2.82)$$

so that by the Heisenberg uncertainty principle (2.78) we have

$$\langle \Delta X_1^2 \rangle \langle \Delta X_2^2 \rangle \geq \frac{1}{4}. \quad (2.83)$$

We can use this general fact about quadratures to deduce a limit on the performance of linear amplifiers imposed by quantum mechanics. Let us write the quadrature operators of the output (i.e., amplified) signal as

$$Y_1 = \sqrt{G_1}X_1 + F_1, \quad Y_2 = \sqrt{G_2}X_2 + F_2, \quad (2.84)$$

where X_1 and X_2 now denote the input quadratures, G_1 and G_2 denote their (potentially different) power gains, and F_1 and F_2 are operators that denote quantum fluctuations, which are necessary for the output operators to obey the canonical quadrature commutation relation (2.82). Specifically, imposing this commutation relation on the output and input quadratures, we see¹⁷

$$\begin{aligned} [Y_1, Y_2] = \frac{i}{2} &\Rightarrow \sqrt{G_1}\sqrt{G_2}\frac{i}{2} + [F_1, F_2] = \frac{i}{2} \\ &\Rightarrow [F_1, F_2] = \frac{i}{2} \left(1 - \sqrt{G_1}\sqrt{G_2}\right). \end{aligned} \quad (2.85)$$

The uncertainty principle (2.78) then yields

$$\langle \Delta F_1^2 \rangle \langle \Delta F_2^2 \rangle \geq \frac{1}{16} \left(1 - \sqrt{G_1}\sqrt{G_2}\right)^2. \quad (2.86)$$

Normalizing this to the gain product $G_1 G_2$ yields the amplifier uncertainty principle for added noise, as described in 1982 by Carlton M. Caves [51],

$$A_1 A_2 \geq \frac{1}{16} \left(1 - \frac{1}{\sqrt{G_1}\sqrt{G_2}}\right)^2. \quad (2.87)$$

For the special case of equal gain for both quadratures, ($\sqrt{G_1} = \sqrt{G_2} = \pm\sqrt{G}$, $A_1 = A_2 = A_N/2$ [the factor of two is there because each quadrature contributes to half of the total added noise when both quadratures are treated on equal footing]), this reduces to the

¹⁷We assume $[X_i, F_j] = 0$, meaning that the input and internal noise fluctuation modes are independent.

fundamental theorem for so-called phase-insensitive amplifiers,

$$A_N \geq \frac{1}{2} \left| 1 \mp \frac{1}{G} \right|. \quad (2.88)$$

If the upper sign applies, we use the term “phase-preserving,” while if the lower sign applies, we use the term “phase-conjugating.” We see that this is precisely equation (2.76) in the zero-temperature limit, which shows that our parametric amplifier when operated in the phase-preserving limit is quantum-limited (we would obtain the analogous result for the phase-conjugating limit, which would involve considering the idler frequency $-\omega$ as the output frequency). In particular, this means that increasing the gain of the parametric amplifier (within the range in which it functions as an ideal one) allows us to increase the signal to noise ratio to very high levels. Of course, there will emerge practical issues in achieving ideal parametric amplifier performance in any real device – in particular, in our device based on SQUID loops, we should be cautious of magnetic flux noise, which can lead to a fluctuating resonance frequency and therefore a fluctuating gain (we will mention a few precautions taken for this in the experimental chapter of this thesis).

Above we have in fact glossed over an important scenario – what happens when the signal is exactly resonant with the pump? In this case, the intermodulation tone in (2.61) in fact has the same frequency as the signal and pump. In this case, the gain will actually depend on the phase of the signal relative to the pump, which makes sense since a relative phase can be defined between two signals of the same frequency. It might seem strange at first that there is only a phase dependence when the signal is exactly on resonance with the pump. However, real signals have a finite (yet potentially very small) bandwidth. In addition, the phase dependence can in fact be seen at other frequencies if we allow for a *multimode* signal and define so-called generalized quadratures that are linear combinations of two modes symmetrically placed above and below the pump frequency (such quadratures exist essentially because they consist of positive and negative frequencies in the rotating frame of the pump. For a brief treatment of such generalized multimode quadratures, see [42].). We will here continue to consider a single tone, this time correctly treating the case $\omega = 0$ on resonance with the pump, leading to phase-dependent gain and added noise essentially due to squeezing of the output mode.

To account for arbitrary quadrature angles, we generalize (2.81) to the (still single-mode) quadrature operators for a mode a

$$X_\theta = \frac{ae^{-i\theta} + a^\dagger e^{i\theta}}{2}, \quad (2.89)$$

so that X_1 and X_2 in (2.81) correspond to the special cases $\theta = 0$ and $\theta = 90^\circ$ respectively. We wish to see what dependence (if any) there is on the phase of the signal relative to the pump; i.e., the input quadrature. To do this, let's decompose the output (2.61) into two amplified input quadratures that are 90° out of phase, with respective quadrature gains \mathcal{A}_θ and \mathcal{B}_θ [we drop the frequency arguments here so that, for example, $\mathcal{M} = \mathcal{M}(0)$ and $c_1^{\text{in}} = c_1^{\text{in}}(0)$]:

$$\begin{aligned} c_1^{\text{out}} &= \mathcal{G}c_1^{\text{in}} + \mathcal{M}c_1^{\text{in}\dagger} \\ &\equiv \mathcal{A}_\theta \frac{c_1^{\text{in}}e^{-i\theta} + c_1^{\text{in}\dagger}e^{i\theta}}{2} + \mathcal{B}_\theta \frac{c_1^{\text{in}}e^{-i(\theta+\pi/2)} + c_1^{\text{in}\dagger}e^{i(\theta+\pi/2)}}{2}. \end{aligned} \quad (2.90)$$

We can then solve for the quadrature gains by equating the coefficients of the input signal mode and its adjoint, leading to two linear equations in two unknowns,

$$\begin{aligned} \mathcal{G} &= \frac{1}{2}e^{-i\theta}\mathcal{A}_\theta - \frac{i}{2}e^{-i\theta}\mathcal{B}_\theta, \\ \mathcal{M} &= \frac{1}{2}e^{i\theta}\mathcal{A}_\theta + \frac{i}{2}e^{i\theta}\mathcal{B}_\theta \end{aligned} \quad (2.91)$$

with the solution

$$\mathcal{A}_\theta = \mathcal{G}e^{i\theta} + \mathcal{M}e^{-i\theta} \quad (2.92)$$

(since θ is arbitrary there is no need to solve for \mathcal{B}_θ). We can then calculate the phase-dependent gain

$$\begin{aligned} G_\theta \equiv |\mathcal{A}_\theta|^2 &= (\mathcal{G}e^{i\theta} + \mathcal{M}e^{-i\theta})(\mathcal{G}^*e^{-i\theta} + \mathcal{M}^*e^{i\theta}) \\ &= |\mathcal{G}|^2 + |\mathcal{M}|^2 + 2\text{Re}\left[\mathcal{G}\mathcal{M}^*e^{2i\theta}\right] \\ &= 2G_s - 1 + 2\sqrt{G_s(G_s - 1)}\cos(2[\theta - \phi]), \end{aligned} \quad (2.93)$$

where we have used the definitions (2.66) and (2.67), the identity (2.74) and defined the relative phase ϕ between the “signal” and “image” contributions to the gain,

$$\mathcal{G}\mathcal{M}^* \equiv |\mathcal{G}||\mathcal{M}|e^{-2i\phi}. \quad (2.94)$$

We therefore see that there exist quadratures 90° out of phase which maximize and minimize the gain (through the cosine term). In the high-gain limit $G_s \gg 1$, we obtain the asymptotic

expressions

$$\begin{aligned}
 G_{\max} &\rightarrow 4G_s, \\
 G_{\min} &\approx 2G_s - 1 - 2G_s\left(1 - \frac{1}{2G_s} - \frac{1}{8G_s^2} + \dots\right) \\
 &\rightarrow \frac{1}{4G_s}.
 \end{aligned} \tag{2.95}$$

In a more general sense (with multimode quadratures), this phase-dependence arises from

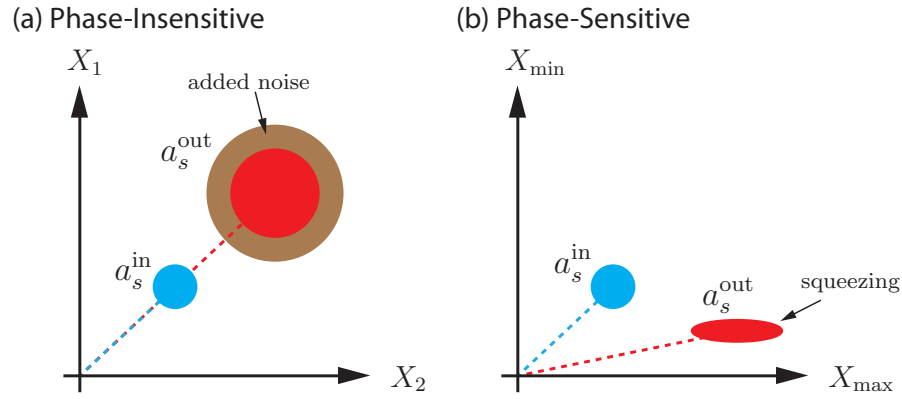


Figure 2.5 Illustration of phase-insensitive and phase-sensitive modes of linear amplification. (a) In the non-degenerate case, the parametric amplifier acts as a phase insensitive amplifier, both amplifying the signal noise (blue circle mapped to red circle) and adding at least one-half quantum of noise (brown circle) in accordance with our above result. (b) In the ideal degenerate case, due to interference between Fourier modes symmetrically placed about the pump there could theoretically be no added noise in accordance with Caves' theorem (2.87). In this case, the amplifier must also amplify one quadrature at the cost of de-amplifying the other.

interference between reflected and squeezed output tones positively and negatively detuned from the pump [15, 42]. In the $\omega = 0$ and more general degenerate multimode case, the amplifier squeezes the output, amplifying one quadrature while de-amplifying (i.e., squeezing) the other. In the single-tone case, we saw earlier that the amplifier must add at least half of a quantum of noise to the output signal via the image channel. However, in the degenerate case, by choosing the correct (generalized) input phase, the added noise can be made arbitrarily small in the desired signal quadrature. To learn more about such interesting squeezing phenomena, see for example [15, 40, 42].

Chapter 3

Implementation with Superconducting Circuits: Theory

The results of the previous chapter are very promising, but they assume that we have a nonlinear quantum oscillator in the first place. In this chapter, we will show how one can construct a system with a Kerr Hamiltonian out of a $\lambda/4$ superconducting microwave coplanar waveguide resonator terminated with a series of Josephson junction-based superconducting SQUIDs. An implementation with Josephson junctions is very appealing for several reasons. The Josephson junction, which is based on superconductivity, is essentially the only known nonlinear circuit element that is practically lossless and functions at the cryogenic temperatures from which the signals we wish to pre-amplify originate in the first place. In addition, Josephson junctions can be fabricated on a chip using standard clean room fabrication techniques that have been developed over the past several decades. This naturally fits in with the circuit QED paradigm, in which superconducting qubits are similarly fabricated. Embedding the Josephson junctions in a coplanar waveguide resonator allows us to control the coupling (both wanted and unwanted) to the parametric oscillator and have good control over the amplified frequency and bandwidth. In the implementation we will explore, the Josephson junctions modify the boundary conditions of the resonator and through their nonlinear inductance give rise to an effective Kerr constant for the system. Capacitively coupling to the input port of the resonator allows one to input pump and signal tones, and then measure the amplified signal via this same port. We note that this is not the only way to make a parametric amplifier with Josephson junctions (for example, a design with particularly good frequency tunability was achieved with an array of many SQUIDs in series, forming the centerpin of a $\lambda/2$ resonator with separate output and input ports [22, 42]), but it is one that requires a reasonable pump power and has recently

enabled the demonstration of interesting quantum optics experiments characterizing states of microwave radiation at the single-photon level [15, 24, 31].

3.1 Superconductivity

3.1.1 Background

The phenomenon of superconductivity was first observed in 1911 by H. Kamerlingh Onnes, due to the ability to induce low temperatures thanks to his 1908 achievement of liquifying helium for the first time [52]. Below a critical temperature T_c and applied magnetic field H_c characteristic to the material, the DC resistance of many metals is observed to abruptly drop to an unmeasurably small value – perpetual supercurrents have been observed to flow for over a year without any measurable dissipation! It is also observed that the superconducting metal becomes a perfect diamagnet – not only are magnetic field lines prohibited from penetrating into the metal (which might have been explained by perfect conductivity alone), but also upon the transition to the superconducting state, any magnetic flux lines originally penetrating the metal are ejected. This is known as the *Meissner effect*.

To give a microscopic derivation of the intriguing properties of the types of superconductors that are currently (approximately) understood is a very formidable task and certainly beyond the scope of this thesis (for a detailed treatment of the features of superconductors discussed here, see for example [53]). We will take as our starting point the results of the BCS quantum theory of superconductivity, put forward by Bardeen, Cooper, and Schrieffer in 1957. This theory describes how a phonon-mediated attractive force between electrons allows the system to condense into a nondegenerate ground state separated from excited states by a significant energy gap 2Δ [52], unlike in an ideal Fermi gas. This gap is of order kT_c and centered at the Fermi energy. Put very broadly, an electron deforms the atomic lattice, allowing a second electron to indirectly interact with it by adjusting to the deformation. The BCS ground state involves pairs of electrons anticorrelated in momentum and spin forming bosonic *Cooper pairs* of charge $-2e$ and zero spin. The BCS theory predicts that it takes an energy of 2Δ to break a Cooper pair. If the temperature is low enough so that the energy gap 2Δ of this Cooper pair fluid is larger than order kT , Cooper pairs will not be scattered by the lattice. For aluminum, $\Delta_{\text{Al}} \approx 3.4 \times 10^{-4}$ eV near absolute zero [52], so that at $T = 10$ mK, $\frac{\Delta_{\text{Al}}}{kT}$ is a few hundred. For niobium, $\Delta_{\text{Nb}} \approx 31 \times 10^{-4}$ eV [52], so that $\frac{\Delta_{\text{Nb}}}{kT}$ is a few thousand. Also, compared to cavity drive photon energies, which are on the order of $h\nu_d = h \times 10$ GHz, $\frac{\Delta_{\text{Al}}}{h\nu_d} \approx 10$ and $\frac{\Delta_{\text{Nb}}}{h\nu_d} \approx 100$. Shielding the sample and filtering input lines also prevents stray radiation from breaking Cooper pairs. It is thus

a good approximation to say that Cooper pairs will remain unbroken.

If we wish to create a nonlinear (i.e., anharmonic) system out of tiny superconducting metallic parts, simple LC oscillators alone will not do. Being a form of harmonic oscillator, LC oscillators lead to equally spaced energy spectra. If we wish to create a qubit out of tiny circuit elements, or in our case provide an effective Kerr constant, we will need a non-linear element. Luckily, superconductivity not only provides us with low dissipation (allowing cQED to satisfy (D3)), but also provides us with a circuit element known as a Josephson junction which unlike other known non-linear circuit elements is dissipationless and consistently retains its non-linear properties down to our required cryogenic temperatures. We will more specifically see that the Josephson junction acts as a non-linear inductor.

The key feature of the BCS theory of superconductivity that we will use is the fact that since the Cooper pairs behave like bosons, condensation into an overlapping common ground state is possible. We can describe this unique ground state with a probability amplitude

$$\psi(\mathbf{r}) = \sqrt{n(\mathbf{r})}e^{i\phi(\mathbf{r})}, \quad (3.1)$$

where $n = |\psi(\mathbf{r})|^2$ is the density of Cooper pairs.

3.1.2 Josephson Junctions

A Josephson junction is simply a thin insulating layer (usually a layer of oxide) sandwiched in between two superconductors (usually two evaporated metal films), as schematically shown in Figure 3.1(a). The two superconducting wavefunctions decay rapidly in the insulator, but there is still the possibility of tunneling as usual in quantum mechanics. To start, imagine a Josephson junction along a superconducting wire, with the wavefunctions of each (identical) superconductor given by $\psi_1 = \sqrt{n_1}e^{i\phi_1}$ and $\psi_2 = \sqrt{n_2}e^{i\phi_2}$. Suppose also that there is an electric potential difference V applied across the junction. As shown in [52], using the coupled Schrödinger equations of motion

$$i\hbar\frac{\partial\psi_1}{\partial t} = \hbar T\psi_2 - eV\psi_1; \quad i\hbar\frac{\partial\psi_2}{\partial t} = \hbar T\psi_1 + eV\psi_2 \quad (3.2)$$

(where T represents the coupling rate between the Cooper pairs of different superconductors) along with the assumption $n_1 \approx n_2$ for identical superconductors, one can arrive at the famous Josephson relations predicted by Brian Josephson in 1962 for the current I and

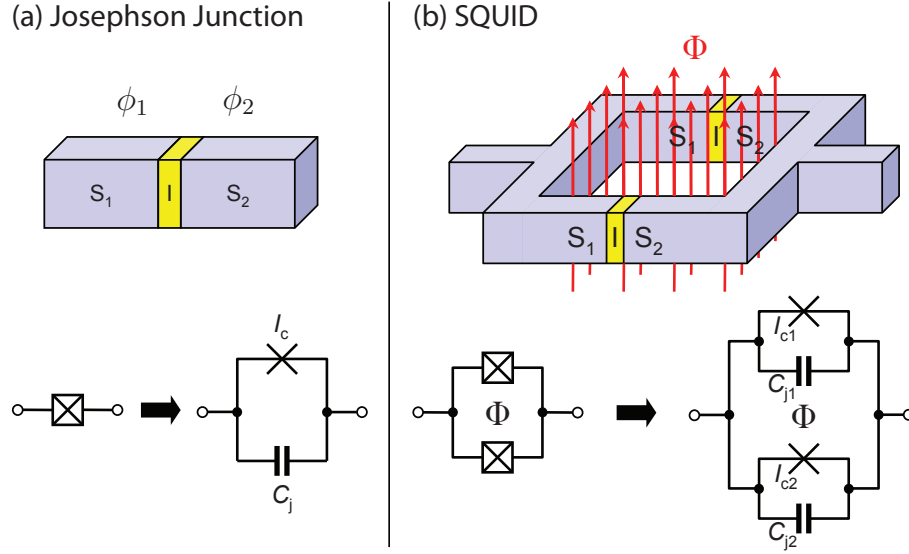


Figure 3.1 (a) Schematic of a Josephson junction consisting of two superconducting electrodes coupled via a thin insulating layer. In our implementation, the insulating layer is formed between two evaporated metal films, not between two metal blocks as drawn. (b) Schematic of a SQUID, consisting of a superconducting loop interrupted by two Josephson junctions. Φ denotes the magnetic flux threading this loop. Figure modified from [54].

phase difference¹ $\phi \equiv \phi_2 - \phi_1$ across the junction:

$$I = I_c \sin \phi \quad (3.3)$$

and

$$\frac{\partial \phi}{\partial t} = \frac{2e}{\hbar} V, \quad (3.4)$$

where I_c is the *critical current*, proportional to the interaction T . This describes the “AC Josephson effect,” which gets its name from the fact that, as can be seen by combining the two equations, a constant applied voltage leads to an alternating current – a quite nonintuitive feature of the quantum world (similar to Bloch oscillations of electrons under the influence of a constant electric field studied in conventional solid-state physics, although these are almost always washed out by scattering of electrons due to imperfections such as impurities, defects, and phonons [52,55])! We can also see how the Josephson junction acts as a non-linear inductor. Differentiating the first Josephson equation with respect to time

¹The superconducting wavefunction $\psi(\mathbf{r})$ for an eigenstate in the bulk of the superconductor behaves like a plane wave, with the phase increasing linearly with position except for phase slips at material interfaces. In the lumped circuit element approximation of a Josephson junction, the relevant wavelengths are usually much larger than the size of the circuit elements, so that we can effectively assign a phase to each element and consider only phase slips at junction interfaces.

and substituting in the second one yields

$$V = \frac{\hbar}{2eI_c \cos \phi} \frac{dI}{dt} \equiv L_J \frac{dI}{dt}, \quad (3.5)$$

indicating an effective phase-dependent (i.e., *nonlinear*) inductance L_J .

We would like to have a Hamiltonian describing the energy associated with Josephson junctions and the time evolution of systems involving Josephson junctions. The electrostatic part of the classical Hamiltonian $\mathcal{H}_{J,\text{el}}$ can be easily written down. As in Figure 3.1, the two superconducting electrodes are capacitively coupled via a shunting capacitance C_j , so that if $n = \frac{Q}{-2e}$ denotes the number of excess Cooper pairs on one of the electrodes, the electrostatic contribution to the classical Hamiltonian becomes

$$\mathcal{H}_{J,\text{el}} = \frac{4e^2 n^2}{2C_j}. \quad (3.6)$$

Next is the most important term in the Hamiltonian, the Josephson contribution. The potential energy stored in the junction purely due to Josephson coupling can be obtained by inserting the Josephson equations into the usual expression for the energy in a circuit element:

$$\begin{aligned} E_{JJ} &= \int_0^t IV dt' = \int_0^t I_c \sin \phi \frac{\hbar}{2e} \frac{\partial \phi}{\partial t'} dt' \\ &= \frac{I_c \hbar}{2e} \int_{\phi(0)}^{\phi(t)} \sin \phi d\phi \rightarrow -E_J \cos \phi, \end{aligned} \quad (3.7)$$

where we have ignored a constant offset in the last step so that

$$E_J = \frac{I_c \hbar}{2e} \quad (3.8)$$

is the *Josephson energy* and the Josephson contribution to the Hamiltonian is

$$\mathcal{H}_{J,j} = -E_J \cos \phi. \quad (3.9)$$

3.1.3 SQUIDS

With a single Josephson junction, the zero- ϕ energy is fixed along with the critical current I_c . However, there is a clever and simple scheme based on what is known as a DC SQUID (*superconducting quantum interference device*, commonly used as an extremely sensitive magnetometer) which can act as an effective Josephson junction with the ability to tune the

effective Josephson energy via applied magnetic flux. If we have two Josephson junctions in a superconducting loop as in Figure 3.1(b), we can relate the difference between the phases across them to the magnetic flux Φ through the loop, due to the phenomenon of *flux quantization* [52]. To arrive at this, first note that the effect of gauge-transformations on the electromagnetic Hamiltonian (B.2), as discussed in Appendix B.1, leads to the velocity in semi-classical Hamiltonian mechanics being

$$\mathbf{v} = \frac{1}{m} (-i\hbar\nabla - q\mathbf{A}). \quad (3.10)$$

Plugging in a wavefunction of the form (3.1) yields a current density of

$$\mathbf{j} = q\psi^*\mathbf{v}\psi = \frac{nq}{m} (\hbar\nabla\phi - q\mathbf{A}). \quad (3.11)$$

Due to the Meissner effect, \mathbf{B} vanishes in the interior so that the current density also vanishes there by Ampère's law. Setting (3.11) to zero yields

$$\hbar\nabla\phi = q\mathbf{A}. \quad (3.12)$$

Now imagine traversing a closed path C through the interior of the superconducting loop. If we require the wavefunction to be single-valued, we need

$$\oint_C \nabla\phi \cdot d\mathbf{l} = 2\pi s, \quad (3.13)$$

where s is an integer. But by Stokes' theorem,

$$\oint_C \mathbf{A} \cdot d\mathbf{l} = \iint_D (\nabla \times \mathbf{A}) \cdot d\boldsymbol{\sigma} = \iint_D \mathbf{B} \cdot d\boldsymbol{\sigma} \equiv \Phi, \quad (3.14)$$

where D is any smooth two-dimensional surface having C as its boundary. Combining this with (3.12) and (3.13), and substituting the Cooper pair charge $q = 2e$, we obtain the condition

$$\Phi = \frac{\pi\hbar s}{e} \quad (3.15)$$

We thus see that flux is quantized in units of the *flux quantum*

$$\Phi_0 = \frac{h}{2e}. \quad (3.16)$$

Combining (3.13) and (3.15) yields a relation between phase and flux,

$$\oint_C \nabla \phi \cdot d\mathbf{l} = \frac{2\pi}{\hbar} \Phi = 2\pi \frac{\Phi}{\Phi_0}. \quad (3.17)$$

If $\phi_{s,1}$ and $\phi_{s,2}$ are the phase slips across junctions 1 and 2 respectively, we define the variables

$$\begin{aligned} \phi_s &\equiv (\phi_{s,1} + \phi_{s,2})/2 \\ \delta &\equiv \phi_{s,1} - \phi_{s,2} \end{aligned} \quad (3.18)$$

so that by flux quantization, $\delta = 2\pi\Phi/\Phi_0$. The Josephson part of the classical SQUID Hamiltonian is now just the sum of the two individual Josephson junction Hamiltonians:

$$\begin{aligned} \mathcal{H}_s &= -E_{J1} \cos \phi_{s,1} - E_{J2} \cos \phi_{s,2} \\ &= -E_{J1} \cos \left(\phi_s + \frac{\delta}{2} \right) - E_{J2} \cos \left(\phi_s - \frac{\delta}{2} \right) \\ &= -E_{J1} \left(\cos \phi_s \cos \frac{\delta}{2} - \sin \phi_s \sin \frac{\delta}{2} \right) \\ &\quad - E_{J2} \left(\cos \phi_s \cos \frac{\delta}{2} + \sin \phi_s \sin \frac{\delta}{2} \right) \\ &\equiv -E_J^{\text{sum}} \left(\cos \left(\pi \frac{\Phi}{\Phi_0} \right) \cos \phi_s + d \sin \left(\pi \frac{\Phi}{\Phi_0} \right) \sin \phi_s \right), \end{aligned} \quad (3.19)$$

where in the last line we have used our flux quantization condition, introduced $E_J^{\text{sum}} = E_{J1} + E_{J2}$ and $d \equiv (E_{J1} - E_{J2})/E_J^{\text{sum}}$. If the Josephson junctions are made to be symmetric², this effectively acts as a single Josephson junction with an effective Josephson energy

$$E_J^{\text{eff}} = E_J^{\text{sum}} \left| \cos \left(\pi \frac{\Phi}{\Phi_0} \right) \right|, \quad (3.20)$$

which is *tunable by magnetic flux* and has a maximum that is twice as large as the single-junction energy.

²An asymmetry parameter of $|d| \lesssim 1\% - 10\%$ is feasible with current fabrication techniques, as the energies depend critically on the thickness of the Josephson junction barrier and other variations in the oxidation process, although current efforts are pushing towards mass manufacturability of nearly identical Josephson junctions for quantum integrated circuits

3.2 Circuit Quantization

3.2.1 Linear Part

We are now ready to describe our physical implementation of a quantum Kerr oscillator, which is schematically illustrated in Figure 3.2. We first find the linear part of the Hamiltonian of the isolated resonator. Our starting point is a circuit model for the joint coplanar waveguide segment + SQUID system shown in Figure 3.2. We first give a classical treatment

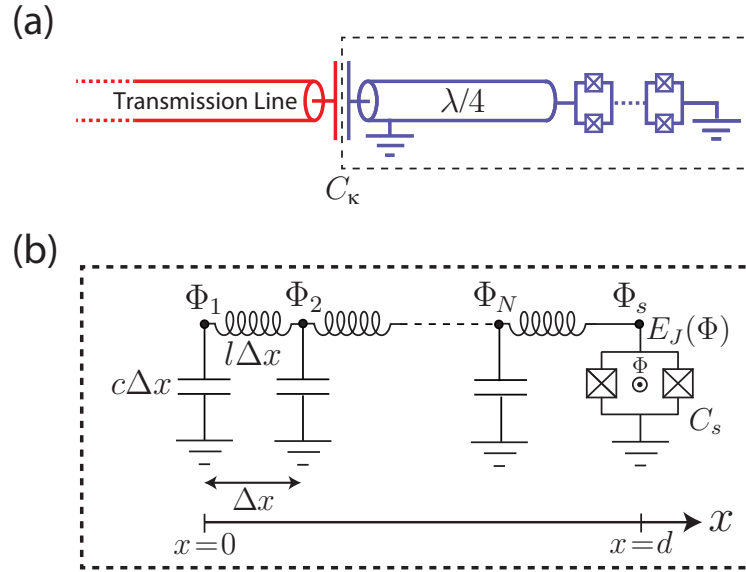


Figure 3.2 (a) Schematic depiction of the nonlinear oscillator system coupled to a transmission line. (b) Circuit model for the nonlinear oscillator system, consisting of a segment of coplanar waveguide transmission line terminated to ground by one or more SQUIDs corresponding to the region within the dashed box in (a). The coplanar waveguide segment is modeled by an infinitesimal chain of capacitors and inductors as shown, with c and l being the capacitance and inductance per unit length of the waveguide respectively.

of this circuit model, and then quantize the Hamiltonian to obtain a quantum mechanical model. This quantization will also give us an approximate picture of the spatial mode structure and root mean square voltages of the transmission line segment. It may seem surprising that we should even be able to notice the quantum-mechanical behavior of a transmission line resonator at all, but at cryogenic temperatures, these tiny superconducting circuits reach such a low level of dissipation that discrete energy levels become observable. It is also true that the superconducting gap limits the degrees of freedom of the system, making them even simpler. Not only is the energy scale of thermal fluctuations small compared to

the relevant transition frequencies ($kT \ll \hbar\omega_0$) and also to the superconducting gap, but the resonator has a high enough quality factor that the finite widths of the energy levels are less than the separation between them. This also requires that the electronic noise temperature from room laboratory equipment coupled to the device be low, which requires careful filtering of signals.

That we model the resonator as a transmission line reflects the fact that we are treating it as an essentially one-dimensional system. This is valid since the width and height of the resonator are several orders of magnitude smaller than its length. This means that many modes along the length of the resonator will be excited before any non-fundamental lateral mode is excited, because the small wavelengths of the lateral modes are associated with correspondingly much higher photon energies. Lumped circuit analysis by itself is not a priori accurate for our resonator, since its length is on the order of the wavelength of the microwaves propagating within it. We will instead be justified in describing the transmission line as a one-dimensional series of infinitesimal lumped LC circuits, using the 1D decomposition of the transmission line from Figure 3.2(b). Our approach will be to consider the microwave oscillations in each of the infinitesimal LC circuits (keeping in mind that we shouldn't consider these circuits so small that a continuous charge distribution approximation breaks down). Due to the superconducting nature of the system, we will ignore resistances (which would require LCR circuits rather than LC circuits) in order to simply understand the ideal quantum behavior of these degrees of freedom using the procedure of canonical quantization.

We follow the treatment given by Wallquist *et al.* [56], filling in the gaps of the derivation and using the language of generalized flux for the transmission line to obtain some intuition from classical circuits. We will also generalize the treatment to the case of $M \geq 1$ SQUIDS. We will first calculate the Hamiltonian in the linear regime (we will see what this means in terms of current flowing through the SQUIDS), and later on calculate the Kerr constant from the leader order of nonlinearity. Let us divide our transmission line segment of length d into many small LC circuits of length Δx . We define the flux variable $\Phi_n(t) = \int_{-\infty}^t V(x_n, t') dt'$ for each node between the n^{th} capacitor and inductor. Then, by definition, the voltage at the n^{th} capacitor node will be $V(x_n, t) = \dot{\Phi}_n(t)$. The voltage drop across the n^{th} inductor is then $\dot{\Phi}_n(t) - \dot{\Phi}_{n-1}(t)$. By Faraday's law of induction, the current through the n^{th} inductor satisfies $\frac{dI}{dt} = -\frac{V}{L\Delta x}$. Integrating this with respect to time, we see that the current across the n^{th} inductor is $\frac{1}{L\Delta x}(\Phi_{n-1}(t) - \Phi_n(t))$. Now, using the familiar formulas from freshman physics [57] for the energies stored in a capacitor and inductor, we can write down a Lagrangian

for the coplanar waveguide portion of system:

$$\mathcal{L}_{\text{CPW}} = \sum_n \left[\frac{c\Delta x}{2} \dot{\Phi}_n^2(t) - \frac{(\Phi_n(t) - \Phi_{n-1}(t))^2}{2l\Delta x} \right]. \quad (3.21)$$

Next, the SQUID array will have a contribution to the system's Lagrangian. We first consider the case of one SQUID [as shown in Figure 3.2(b)] for simplicity, and later give a simple argument to generalize to M SQUIDs in series [as shown in Figure 3.2(a)]³. There will be a (small) electrostatic contribution from the shunting capacitance, equal to $\sum_{i=1,2} \frac{1}{2} (\frac{C_s}{2}) V_i^2$, where V_i is the voltage drop across the i^{th} junction in the two-junction SQUID loop and C_s is the (small) shunting capacitance across the split junctions (assumed to consist of equal contributions $C_s/2$ from each junction). By the second Josephson equation we can write this as $\frac{\hbar^2}{2(2e)^2} \frac{C_s}{2} (\dot{\phi}_{s,1}^2 + \dot{\phi}_{s,2}^2) = \frac{\hbar^2}{2(2e)^2} C_s \dot{\phi}_s^2$, where ϕ_s is the effective Josephson junction phase drop $(\phi_{s,1} + \phi_{s,2})/2$ of a SQUID loop with identical junctions, as discussed earlier⁴. We also have, most importantly of course, the Josephson energy contribution $-E_J(\Phi) \cos \phi_s$ stored in the junctions, which, as we will derive in the next section, gives a nonlinearity that manifests itself as a Kerr constant for the joint system. To make the dynamical variables of the system unitless and also to avoid potential confusion between the Φ_j (generalized flux at a node) and Φ (magnetic flux threaded through a SQUID loop), we will work with the unitless superconducting phases $\phi_j = \frac{(2e)}{\hbar} \Phi_j$. Finally, using this convention, there is one more term in the Lagrangian – the phase drop⁵ between the final circuit node ϕ_N and the SQUID node ϕ_s . Adding this final piece of bookkeeping gives us the total system Lagrangian⁶ in terms

³Keep in mind that the SQUIDs here are not drawn to scale – in reality they take up a length that is small compared to the relevant wavelength of the resonator so that they can be lumped into the boundary in our treatment. We will also of course show why more than one SQUID (rather than simply one SQUID with a larger inductance) would be desirable.

⁴Really we have $\dot{\phi}_s^2 = (\dot{\phi}_{s,1} + \dot{\phi}_{s,2})^2 = \dot{\phi}_{s,1}^2 + 2\dot{\phi}_{s,1}\dot{\phi}_{s,2} + \dot{\phi}_{s,2}^2$. But for static (or adiabatically changing) magnetic flux through a SQUID loop, we have $\dot{\phi}_{s,1} - \dot{\phi}_{s,2} = 0$, which when squared allows us to substitute for $\dot{\phi}_{s,1}\dot{\phi}_{s,2}$ above.

⁵There is nothing particularly special about this phase drop as opposed to the others, but it is an artifact of how we have labeled the $N + 1$ total nodes. Due to the second Josephson relation, the superconducting phase drop across the SQUID is related to voltage in the same way as the generalized phase defined for the circuit nodes, so that this term takes the same form; i.e., the square of the phase difference.

⁶It may seem strange to have factors of \hbar in a classical Lagrangian, but this simply stems from how we have redefined the unitless generalized flux to have units of phase, and the fact that the Josephson junction can be modeled as a nonlinear inductor only if it obeys the Josephson relations (which involve \hbar) to begin with.

of the unitless dynamical variables ϕ ,

$$\begin{aligned} \mathcal{L}_{\text{sys}} = \sum_n \left(\frac{\hbar}{2e} \right)^2 & \left[\frac{c\Delta x}{2} \dot{\phi}_n^2(t) - \frac{(\phi_n(t) - \phi_{n-1}(t))^2}{2l\Delta x} \right] \\ & + \frac{\hbar^2}{2(2e)^2} C_s \dot{\phi}_s^2 + E_J(\Phi) \cos(\phi_s) - \frac{\hbar^2(\phi_s - \phi_N)^2}{2(2e)^2 l \Delta x}. \end{aligned} \quad (3.22)$$

We now make two approximations limiting us to a linear regime for now. Namely, we approximate the SQUID as a harmonic oscillator by Taylor expanding the cosine in the Josephson energy to only second order and writing the SQUID part of the Lagrangian as

$$\mathcal{L}_{\text{SQUID}}^{\text{harm}} = \frac{\hbar^2 C_s}{2(2e)^2} \dot{\phi}_s^2 - \frac{1}{2} E_J(\Phi) \phi_s^2. \quad (3.23)$$

This is valid when $\phi_s \ll 1$, which is satisfied when the SQUID is in the so-called phase regime (like in a transmon qubit), $E_J \gg E_C$. Before deriving a quantum Hamiltonian under these approximations, we will use the principle of stationary action from classical mechanics [34] to derive boundary conditions for the system's modes of oscillation. To do this, we focus on the dynamics of ϕ_s at the boundary of the resonator. Replacing the cosine in (3.22) with its quadratic approximation and using the Euler-Lagrange equation for the dynamical variable ϕ_s , we have

$$\frac{d}{dt} \left[\frac{\partial \mathcal{L}}{\partial \dot{\phi}_s} \right] - \frac{\partial \mathcal{L}}{\partial \phi_s} = 0 \longrightarrow \frac{\hbar^2 C_s}{(2e)^2} \ddot{\phi}_s + E_J(\Phi) \phi_s + \frac{2\hbar^2(\phi_s - \phi_N)}{2(2e)^2 l \Delta x} = 0. \quad (3.24)$$

We recognize the last term as the difference quotient for the first spatial derivative of $\phi(x, t)$ at $x = d$, so that taking the continuum limit and recognizing that

$$\phi(d, t) = \phi_s(t) \quad (3.25)$$

by continuity yields the boundary condition

$$\frac{\hbar^2 C_s}{(2e)^2} \ddot{\phi}(d, t) + E_J(\Phi) \phi(d, t) + \frac{\hbar^2 d}{(2e)^2 L_{\text{cav}}} \phi'(d, t) = 0, \quad (3.26)$$

where for later convenience we have defined

$$L_{\text{cav}} \equiv ld, \quad C_{\text{cav}} \equiv cd. \quad (3.27)$$

Next, in the bulk of the transmission line segment, we have the classical Hamiltonian

$$\mathcal{H}_{\text{bulk}} = \sum_n \dot{\phi}_n \frac{\partial \mathcal{L}_{\text{bulk}}}{\partial \dot{\phi}_n} - \mathcal{L}_{\text{bulk}} \quad (3.28)$$

$$= \sum_n \left(\frac{\hbar}{2e} \right)^2 \left[\frac{c\Delta x}{2} \dot{\phi}_n(t)^2 + \frac{(\phi_n(t) - \phi_{n-1}(t))^2}{2l\Delta x} \right]. \quad (3.29)$$

We now introduce the conjugate momentum of the phase, $q_n(t) = \frac{\partial \mathcal{L}_{\text{bulk}}}{\partial \dot{\phi}_n} = c\Delta x \dot{\phi}_n(t)$, which is proportional to the charge on the n^{th} capacitor. Hamilton's equation of motion then gives

$$\left(\frac{\hbar}{2e} \right)^2 c\Delta x \ddot{\phi}_n = \dot{q}_n = -\frac{\partial \mathcal{H}}{\partial \phi_n} = \left(\frac{\hbar}{2e} \right)^2 \frac{\phi_{n+1} - 2\phi_n + \phi_{n-1}}{l\Delta x}. \quad (3.30)$$

Dividing both sides of this equation of motion by $c\Delta x$ and recognizing the difference quotient for the second spatial derivative, we obtain in the continuum limit of large N (i.e., $\Delta x \rightarrow dx$)

$$\frac{\partial^2 \phi(x, t)}{\partial t^2} = v^2 \frac{\partial^2 \phi(x, t)}{\partial x^2}, \quad (3.31)$$

where $v = 1/\sqrt{lc}$ is the speed of propagation. In the sinusoidal steady-state, we can take $\phi(x, t) = e^{i\omega t} g(x)$, which leads to an eigenvalue equation for $g(x)$

$$\frac{d^2 g}{dx^2} = -\frac{\omega^2}{v^2} g \equiv -k^2 g. \quad (3.32)$$

The solutions to this equation depend on the boundary conditions of the resonator. The open (or capacitively coupled) boundary condition at $x = 0$ dictates that we may take the current to vanish at the ends, so that the spatial eigenfunctions for ϕ have a vanishing derivative at the boundary (remember our expression above for the current through the n^{th} inductor) and so are cosines. We can therefore take $\phi(x, t) = \phi_0 \sin(kft) \cos(kx)$. Substituting this bulk solution into the boundary condition (3.26) and dividing through by $\phi_0 \sin(kft)$ then yields

$$\begin{aligned} & -\frac{\hbar^2}{(2e)^2} C_s (kf)^2 \cos(kd) - \frac{\hbar^2 kd}{(2e)^2 L_{\text{cav}}} \sin(kd) + E_J(\Phi) \cos(kd) = 0 \\ \Rightarrow & (kd) \tan(kd) = \frac{(2e)^2}{\hbar^2} L_{\text{cav}} E_J(\Phi) - L_{\text{cav}} C_s (kf)^2 \\ \Rightarrow & (kd) \tan(kd) = \frac{L_{\text{cav}}}{L_J(\Phi)} - \frac{C_s}{C_{\text{cav}}} (kd)^2, \end{aligned} \quad (3.33)$$

where in the last step we have used equation (3.5) for the effective Josephson inductance L_J and also the identity $f = d/\sqrt{L_{\text{cav}} C_{\text{cav}}}$. This result is quite interesting and very important:

it shows explicitly that we can tune the wavelength (and hence the frequency) of the allowed resonant modes of the system by tuning the Josephson energy of the SQUID through applied magnetic flux Φ . For realistic resonators and junctions used in cQED, C_s is generally negligible compared to C_{cav} – for the junction areas of $4 \mu\text{m}^2$ we will use, approximating the oxide thickness⁷ as 10 nm and its dielectric constant as 1, a simple parallel-plate capacitor model yields $C_s/2 \approx \epsilon_0(4 \mu\text{m}^2)/(10 \text{ nm}) = 3 \text{ fF}$, whereas (using parameters we will calculate later) our resonator will have $C_{\text{cav}} \approx (1.6 \times 10^{-10} \text{ F/m})(4 \text{ mm}) = .6 \text{ pF}$. Figure 3.3 shows

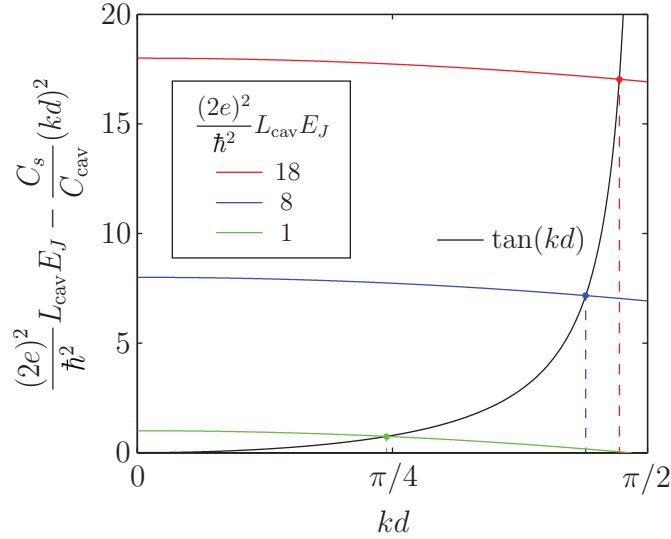


Figure 3.3 Plots of the left- and right-hand sides of equation (3.33). The black curve shows $\tan(kd)$, while the green, blue, and red curves denote the right-hand side of the equation for values $\frac{(2e)^2}{h^2} L_{\text{cav}} E_J = 1, 8, \text{ and } 18$ respectively. The small ratio $C_s/C_{\text{cav}} \sim .01$ is as in our crude estimate in the main text, and leads to a slight bend in the colored curves.

a plot of the left and right sides of this equation, for three different values of E_J relative to $\frac{h^2}{(2e)^2 L_{\text{cav}}}$. The intersections of a given colored curve with the black curve yields the solution for kd , which in turn determines the resonance frequency of the system when the resonator length d is specified⁸. The limit $E_J \rightarrow \infty$ can be understood as a disappearing junction, leading to a short of the centerpin to ground at $x = d$. Along with the open boundary condition at $x = 0$, it then makes sense that this corresponds to a $\lambda/4$ resonator according to Figure 3.3. As $E_J(\Phi)$ is lowered (comparable to $\frac{h^2}{(2e)^2 L_{\text{cav}}}$), the solution for k starts to drop at an increasing rate, leading to a resonance frequency that tends to zero. In between

⁷This value is quoted from Sri, as I have not measured it myself. Other junctions in the literature for similar devices also have thicknesses of a few nm (see for example [54, 58]).

⁸There are further intersections with the tangent curve for $kd > \pi/2$, but we'll only consider the low-frequency solutions in the range $0 < kd < \pi/2$.

these two limits, we can in principle interpolate to any resonance frequency we want by applying the right amount of magnetic flux Φ . However, the sensitivity to flux variations changes drastically over this range. For small E_J it is both the case that the solution for k becomes very sensitive to Φ , and is also the case that $E_J(\Phi)$ itself becomes very sensitive to Φ . Also, in real devices there is a finite amount of asymmetry between the two Josephson junctions in a SQUID loop, which puts a limit on how low the effective energy of the SQUID loop can be tuned. Also, earlier experiments implementing this kind of tunable resonator have observed a decrease in the internal quality factor of the system when the SQUIDs are tuned to smaller energies, possibly due to increased power dissipated by subgap resistance⁹ in the junctions (not just from inhomogeneous broadening due to flux noise) [59]. On the other hand, if E_J is too large, the k is essentially independent of E_J , with $kd \approx \pi/2$. For moderate values of E_J (say, L_{cav}/L_J around 3 to 12; for example, the blue curve in Figure 3.3), there is in some sense a balance between tunability and stability. In the experimental part of this thesis (the aim of which is to read out a system of a known, fixed frequency), we will aim to fabricate SQUIDs whose maximum energies are at or slightly above this middle regime. For energies in this regime or higher, we can approximately solve the transcendental equation (3.33) for $C_s = 0$ by expanding its reciprocal about $kd = \pi/2$ [remembering that $\cot(x)$ about $\pi/2$ looks like $-\tan(x)$],

$$\begin{aligned} \frac{\cot(kd)}{kd} &\approx \frac{\frac{\pi}{2} - kd}{kd} = \frac{L_J(\Phi)}{L_{\text{cav}}} \Rightarrow k = \frac{\pi}{2d} \frac{1}{1 + \frac{L_J(\Phi)}{L_{\text{cav}}}} \\ &\Rightarrow f(\Phi) = \frac{kv}{2\pi} \approx \frac{f_0}{1 + \frac{L_J(\Phi)}{L_{\text{cav}}}}, \end{aligned} \quad (3.34)$$

where $f_0 = \frac{1}{4\sqrt{L_{\text{cav}}C_{\text{cav}}}}$ is the resonance frequency of the corresponding bare $\lambda/4$ resonator.

Continuing our analysis of the system's modes of oscillation, we focus on the trajectory of a single excited mode of oscillation for fixed k ,

$$\phi(x, t) = \phi_k(t) \cos(kx). \quad (3.35)$$

In the continuum limit, substituting this form for ϕ in equation (3.22) and integrating over the resonator (using the harmonic approximation for the SQUID energy and ignoring C_s)

⁹For voltages applied across a junction which are less than the so-called gap voltage (which is able to break Cooper pairs), the thermal energy $k_B T$ can create a small density of quasiparticles (essentially broken Cooper pairs) whose current is not in the superconducting state. This leads to a subgap resistance that depends on the number of excited quasiparticles [54]. As the Josephson energy is decreased, the SQUID inductance increases, causing more of the current to flow through the subgap channel, which acts as a shunt resistance.

yields the oscillator Lagrangian¹⁰

$$\begin{aligned}
\mathcal{L}_{\text{osc}} &= \left(\frac{\hbar}{2e}\right)^2 \int_0^d \left[\frac{1}{2} c \dot{\phi}_k^2 \cos^2(kx) - \frac{\phi_k^2 k^2 \sin^2(kx)}{2l} \right] dx - \frac{1}{2} E_J(\Phi) \phi_k^2 \cos^2(kd) \\
&= \frac{\hbar^2}{2(2e)^2} C_{\text{cav}} \left[\frac{1}{2} + \frac{\sin(2kd)}{4kd} \right] \dot{\phi}_k^2 - \frac{\hbar^2}{2(2e)^2} \frac{k^2 d}{L_{\text{cav}}} \left[\frac{d}{2} - \frac{\sin(2kd)}{4k} \right] \phi_k^2 - \frac{1}{2} E_J(\Phi) \phi_k^2 \cos^2(kd) \\
&= \frac{\hbar^2}{2(2e)^2} \frac{C_{\text{cav}}}{2} \left[1 + \frac{\sin(2kd)}{2kd} \right] \dot{\phi}_k^2 - \frac{\hbar^2}{2(2e)^2} \frac{(kd)^2}{2L_{\text{cav}}} \left[1 - \frac{\sin(2kd)}{2kd} \right] \phi_k^2 \\
&\quad - (kd) \frac{\tan(kd)}{2} \frac{\hbar^2}{(2e)^2 L_{\text{cav}}} \cos^2(kd) \phi_k^2 \\
&\equiv \frac{C_k}{2} \left(\frac{\hbar \dot{\phi}_k}{2e} \right)^2 - \frac{1}{2L_k} \left(\frac{\hbar \phi_k}{2e} \right)^2, \tag{3.36}
\end{aligned}$$

where in the third line we have used the boundary condition (3.33) for $E_J(\Phi)$, valid in the Lagrangian for static or adiabatically changing flux. We then see that in the linear approximation, the system acts like an LC oscillator with an effective capacitance and inductance

$$C_k = \frac{C_{\text{cav}}}{2} [1 + \text{sinc}(2kd)], \quad L_k = \frac{2L_{\text{cav}}}{(kd)^2 [1 + \text{sinc}(2kd)]} \tag{3.37}$$

that depend on k and therefore on Φ . This is consistent with (3.32), since

$$\omega_k = \frac{1}{\sqrt{L_k C_k}} = \frac{kd}{\sqrt{L_{\text{cav}} C_{\text{cav}}}}. \tag{3.38}$$

We now obtain the classical Hamiltonian of the oscillator through the Legendre transform,

$$\mathcal{H}_{\text{osc}} = \dot{\phi}_k \frac{\partial \mathcal{L}_{\text{osc}}}{\partial \dot{\phi}_k} - \mathcal{L}_{\text{osc}} = \left(\frac{\hbar}{2e}\right)^2 \left[\frac{C_k}{2} \dot{\phi}_k^2 + \frac{1}{2L_k} \phi_k^2 \right] \tag{3.39}$$

We introduce the charge number variable $n_k \equiv \frac{1}{\hbar} \frac{\partial \mathcal{L}_{\text{osc}}}{\partial \dot{\phi}_k} = \frac{\hbar C_k}{(2e)^2} \dot{\phi}_k$, so that $\hbar n_k$ is the canonically conjugate momentum to ϕ_k , allowing us to express the Hamiltonian in the very simple form

$$\mathcal{H}_{\text{osc}} = E_{C_k} n_k^2 + E_{L_k} \phi_k^2, \tag{3.40}$$

where we have defined the effective capacitive and inductive energies of the oscillator

$$E_{C_k} = \frac{(2e)^2}{2C_k}, \quad E_{L_k} = \frac{\hbar^2}{2(2e)^2 L_k}. \tag{3.41}$$

¹⁰When we factor out $\Delta x \rightarrow dx$ from the sum over nodes, the second term in the summand becomes a squared spatial derivative in the limit $\Delta x \rightarrow 0$.

n can then be interpreted as analogous to the excess charge (in units of Cooper pairs) on the effective “capacitor” necessary to give the oscillator’s charging energy. Since ϕ_k and $\hbar n_k$ obey Hamilton’s equations of motion as conjugate variables with Poisson bracket $\{\phi_k, \hbar n_k\} = 1$, under Dirac’s method of canonical quantization [60], they can be promoted to operators obeying the canonical commutation relation

$$[\phi_k, \hbar n_k] = i\hbar \Rightarrow [\phi_k, n_k] = i. \quad (3.42)$$

As is standard [61] for the treatment of quantum harmonic oscillators, we introduce the analogous dimensionless lowering and raising operators for our oscillation mode (dropping the subscript k),

$$A = \left(\frac{E_{L_k}}{4E_{C_k}} \right)^{\frac{1}{4}} \phi_k + i \left(\frac{E_{C_k}}{4E_{L_k}} \right)^{\frac{1}{4}} n_k, \quad (3.43a)$$

$$A^\dagger = \left(\frac{E_{L_k}}{4E_{C_k}} \right)^{\frac{1}{4}} \phi_k - i \left(\frac{E_{C_k}}{4E_{L_k}} \right)^{\frac{1}{4}} n_k, \quad (3.43b)$$

so that

$$\phi_k = \left(\frac{E_{C_k}}{4E_{L_k}} \right)^{\frac{1}{4}} (A + A^\dagger), \quad (3.44a)$$

$$n_k = i \left(\frac{E_{L_k}}{4E_{C_k}} \right)^{\frac{1}{4}} (A^\dagger - A), \quad (3.44b)$$

with

$$[A, A^\dagger] = 1 \quad (3.45)$$

(we assume k is fixed and drop the subscript from now on). Using (3.38), the quantum Hamiltonian for our oscillator in the harmonic approximation then takes the familiar form

$$H_0 = \hbar\omega_k \left(A^\dagger A + \frac{1}{2} \right). \quad (3.46)$$

3.2.2 Kerr Nonlinearity

In the previous section, we derived a simple harmonic oscillator Hamiltonian, which could have been done without any SQUID present in the system. In the harmonic approximation (3.23), the only role of the SQUID is to dictate the boundary condition of the system resonance, and to provide tunability of this resonance via magnetic flux. In a sense, all we’ve done so far is generalize a linear coplanar waveguide resonator. For making a parametric

amplifier, we of course need a source of nonlinearity. We will now show how an effective Kerr term is added to (3.46) when we consider the nonlinear part of the SQUID inductance (3.5).

Doing this is a simple extension of the machinery we developed in the previous section. We consider the next term in the expansion of the cosine in the Josephson energy term of (3.22), obtaining a correction to the Lagrangian of

$$\delta\mathcal{L} = \frac{E_J(\Phi)}{24}\phi_s^4 = \frac{E_J(\Phi)}{24}\cos^4(kd)\phi_k^4, \quad (3.47)$$

where we have used (3.25) and (3.35). This leads to the same change in the Hamiltonian $\dot{\phi}_k \frac{\partial[\delta\mathcal{L}]}{\partial\phi_k} - \delta\mathcal{L}$, except with a minus sign. Using the identification (3.44a), we obtain a Kerr term for the Hamiltonian,

$$\begin{aligned} \delta H_{\text{Kerr}} &= -E_J(\Phi) \frac{E_{C_k}}{96E_{L_k}} \cos^4(kd)(A + A^\dagger)^4 \\ &\approx -E_J(\Phi) \frac{E_{C_k}}{16E_{L_k}} \cos^4(kd)(A^\dagger)^2 A^2. \end{aligned} \quad (3.48)$$

We have now arrived at what we set out to obtain, a quantum nonlinear oscillator with a Hamiltonian of the form (2.10), with a Kerr constant of

$$K = -\frac{1}{\hbar} E_J(\Phi) \frac{E_{C_k}}{8E_{L_k}} \cos^4(kd). \quad (3.49)$$

We note that K is negative, which is why we chose a negative K for our plots in the previous chapter. This value of K is extremely important for the parametric amplification process, as we saw in the previous chapter. For moderate to large values of E_J (i.e., small values of L_J), we can more clearly obtain the dependence of K on the Josephson energy through the first line of (3.34),

$$K \approx -\frac{1}{\hbar} E_J(\Phi) \frac{E_{C_k}}{8E_{L_k}} \left(\frac{L_J}{L_{\text{cav}}} \right)^4 \propto \frac{1}{E_J^3}. \quad (3.50)$$

In general, a higher Josephson critical current will allow for the use of higher powers when driving the resonator, as more current is able to flow through the junctions in accordance with the Josephson relations. More specifically, because of the first Josephson equation, the critical current determines the range of currents that are considered “small” in that the phase drop across the junction is much less than unity. The small-phase limit was one of the important approximations we made in our derivations above, and so we must ensure that it is satisfied in experiments. From (3.35) and (3.44a), we can calculate a “saturation” pump photon number N_{sat} (not to be confused with N_{crit}) for which we have

the highly undesirable equality $\phi_s = 1$. More specifically, we can calculate

$$\frac{N_{\text{crit}}}{N_{\text{sat}}} = \frac{2}{\sqrt{3}} \frac{(\gamma_1 + \gamma_2)}{|K|} \cos^2(kd) \sqrt{\frac{E_{C_k}}{4E_{L_k}}} = \frac{2\sqrt{2}}{\sqrt{3}} \frac{(\gamma_1 + \gamma_2)}{\sqrt{|K|}} \sqrt{\frac{\hbar}{E_J}} \propto \frac{(\gamma_1 + \gamma_2)}{L_J}, \quad (3.51)$$

which we would like to keep much less than unity because we would like to drive the Kerr oscillator near its critical point for large gains without worrying about violating the small phase approximation. We could keep this value small by increasing L_J , but this would in fact decrease the dynamic range of the amplifier because N_{crit} is proportional to $1/|K|$, which decreases with L_J . And since $N_{\text{crit}}/N_{\text{sat}}$ also increases with γ_1 , this places a limit on the gain-bandwidth product of the resulting parametric amplifier.

It is therefore difficult to build a good parametric amplifier with a single SQUID. But, as hinted earlier, we can get around this problem by using an array of SQUIDs rather than one physical SQUID. First, we note that in the linear regime, inductances add in series. Therefore, if we use a series array of M SQUIDs (as depicted in Figure 3.2a), each with a Josephson energy M -times larger than what would have been used with a single SQUID, the linear Josephson inductance and therefore the resonance frequency and tunability of the resonator [remember equation (3.34)] will remain unchanged. However, the nonlinear part of the Josephson inductance will in fact decrease, essentially because we are diluting it with linear inductance. To see this, assume that the number of SQUIDs is small enough that the spatial region taken by them on the centerpin is still small compared to all wavelengths used to probe the resonator. When this is true, a lumped element circuit analysis still holds, and we can in addition assume that the phase drop across each junction is the same by symmetry¹¹. The quadratic term of the harmonic part of the Lagrangian (3.36) then inherits M terms, each of which is multiplied by M due to the assumed M -fold increase in E_J and then divided by M^2 due to the assumption of equal phase drop across the m^{th} SQUID, $\phi_{s,m} = \phi_N/M$ (referring to Figure 3.2b), which reduces to the same Lagrangian as for one SQUID. However, the non-harmonic quartic term (3.47) is proportional to the phase drop to the fourth power, leading to an uncompensated factor of $1/M^2$ under this same analysis. Therefore, the Kerr constant decreases as $1/M^2$, whereas the ratio $N_{\text{crit}}/N_{\text{sat}}$ depends only on the total linear Josephson inductance. In summary, using multiple SQUIDs allows us to maintain both dynamic range and tunability in the small phase limit. Note that derivations very similar to the ones in this subsection were independently given in [15].

¹¹We are implicitly assuming that the SQUIDs are identical, including identical couplings to external magnetic flux. Later we will see how we can experimentally attempt to make this a good approximation.

Chapter 4

Implementation with Superconducting Circuits: Experiment

In this chapter, we describe the process of designing, fabricating, and measuring an actual Josephson parametric amplifier according to the predictions of the previous two chapters. The most substantial (i.e., time-consuming) part of this thesis was the process of learning, practicing, and optimizing various cleanroom micro- and nanofabrication techniques, which would have taken much longer were it not for the gracious help of others (see Acknowledgments).

4.1 Design and Fabrication

In this section, we describe the process of designing and physically building a Josephson parametric amplifier on a chip. We will discuss the logic behind our chosen design parameters and the process of experimentally realizing these parameters, including the use of important tools ranging from electromagnetic simulation to electron beam lithography. A large part of this was engineering not only designs but also clean room fabrication recipes.

4.1.1 Coplanar Waveguide Resonators

Geometry

The type of resonator chosen for our implementation is a segment of coplanar waveguide (abbreviated CPW, incidentally the initials of its 1969 inventor, C. P. Wen), an approximately planar structure consisting of a centerpin surrounded by gaps of equal width on either side from ground planes as illustrated in Figure 4.1. The ground planes extend far enough out relative to the width and height of the centerpin and gaps that they can reasonably be treated as semi-infinite for the sake of resonator parameter calculations. We first consider a bare $\lambda/4$ resonator without any SQUIDs embedded at the shorted end. We will want to design and test such a functioning bare resonator before we attempt to embed SQUIDs. A schematic top and cross-sectional view of the resonator is shown in Figure

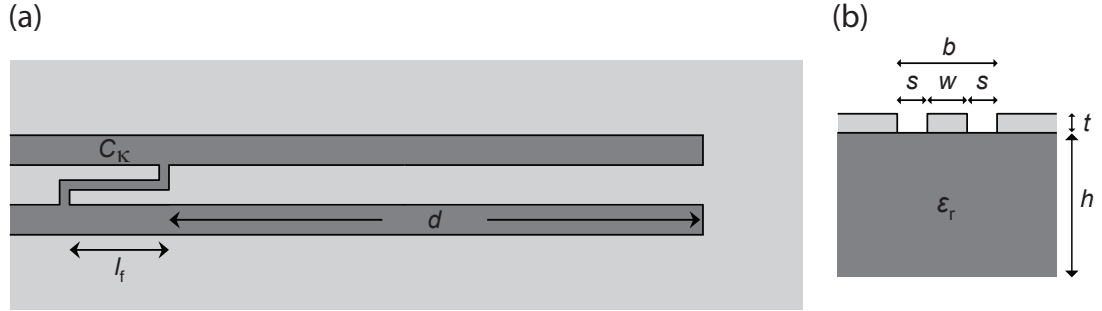


Figure 4.1 (a) Bare $\lambda/4$ CPW resonator. Light gray denotes a Nb film, while dark gray denotes the sapphire substrate beneath. Note that this is not drawn to scale – in reality $l_f \ll d$. Note also that the color chosen to represent the Nb film is somewhat accurate with respect to how it appears to the naked eye, but the sapphire substrate is not darker and is in fact transparent (pictures of real devices will be shown below). The left end of the CPW is coupled to an output line via a coupling finger capacitor of with capacitance C_K . (b) Cross-section view of the bulk of the CPW. Note that this is not drawn to scale – in reality $t \ll h$. ϵ_r denotes the dielectric constant (relative permittivity) of the substrate.

4.1(a) and 4.1(b) respectively. It is essentially a small two-dimensional version of a coax cable, with the gap at the left end acting like a mirror that can reflect or transmit photons. The centerpin height, width, and gaps ensure that the resonator can be treated as a one-dimensional system, as was done in the previous chapter in the context of embedded SQUIDs. The choice of such a resonator, which supports quasi-TEM waves (i.e., essentially transverse electric and magnetic fields, with small longitudinal components [16]), is a good one for several reasons. Both the centerpin and ground plane can be easily fabricated on a chip with standard clean room techniques in a single layer, without using any dielectric

thin films, which can be lossy. The CPW has a characteristic impedance that can be easily related to the ratio of the centerpin width to gap. This means that we can connect to the CPW from larger bonding pads while impedance-matched by gradually changing the width of the centerpin, as long as the ratio of centerpin width to gap remains constant during this change. Because of this, we are also essentially free to choose the width of the centerpin so that it is both easily fabricated with photolithography (described later) and so that it is of a convenient size for the embedding of SQUIDs. The use of niobium on sapphire is known to consistently yield high CPW resonator quality factors as well. And of course, the CPW allows a straightforward embedding of SQUIDs for inherited nonlinearity, as seen in the previous chapter, due to the presence of a centerpin close to the ground planes, as opposed to, say, a slotline waveguide.

Frequency

To design a CPW, we need to understand how its resonance frequency, characteristic impedance (determined by capacitance and inductance per unit length), and quality factors are determined by the CPW (plus coupling capacitor) geometry and material parameters. The resonance frequency of the bare $\lambda/4$ resonator is simply given by equation (3.38) [or equation (3.34)] in the limit of zero SQUIDs (i.e., zero SQUID inductance). However, unlike in Figure 3.2(b), we are now coupling the resonator at its $x = 0$ to a coax line via a coupling capacitor (as in Figure 3.2(a) and Figure 4.1). To a good approximation, this capacitive loading effectively adds to C_{cav} , yielding a downward-shifted resonance frequency of approximately [62]

$$f_r = \frac{1}{4\sqrt{L_{\text{cav}}(C_{\text{cav}} + C_{\kappa})}}. \quad (4.1)$$

As we will show, desirable coupling capacitances for our paramp are small enough compared to C_{cav} that we can essentially design the resonance frequency and coupling capacitance independently (to within $\sim 1\%$). If we wish to use our paramp to read out a superconducting qubit stored in a cavity of frequency 6.85 GHz¹, in order to reach a compromise between stability and tunability (as discussed in the context of Figure 3.3), we will aim for a bare quarter-wave resonance frequency of 8 GHz. This also conveniently coincides with the nominal maximum frequency specification for a circulator we will use in the experimental setup. To determine the resonance frequency, we therefore need to know the inductance l and capacitance c per unit length (or the *characteristic impedance*² $Z_c = \sqrt{l/c}$) of a

¹This is the cavity resonance frequency of a cQED sample from the Houck lab that we will use to practice operating the paramp for time-resolved cQED qubit state readout.

²See Appendix C for a brief explanation of characteristic impedance.

reasonable CPW, which along with the length d of the resonator determines its resonance frequency.

Characteristic Impedance

Defining the geometrical parameters [referring to the dimensions shown in Figure 4.1(b)]

$$k \equiv \frac{w}{b}, \quad k' \equiv \sqrt{1 - k^2}, \quad k_3 \equiv \frac{\tanh\left(\frac{\pi w}{4h}\right)}{\tanh\left(\frac{\pi b}{4h}\right)}, \quad k'_3 \equiv \sqrt{1 - k_3^2}, \quad \tilde{K} \equiv \frac{K(k')K(k_3)}{K(k)K(k'_3)}, \quad (4.2)$$

where K is the complete elliptic integral of the first kind (computable with the Mathematica function `EllipticK[]`), it can be shown using conformal mapping techniques that the characteristic impedance in the bulk of a CPW is given by [7, 63]

$$Z_c = \frac{Z_0/2}{\sqrt{\epsilon_{\text{eff}}}} \left(\frac{K(k)}{K(k')} + \frac{K(k_3)}{K(k'_3)} \right)^{-1}, \quad (4.3)$$

where Z_0 is the “impedance of free space,” $Z_0 = \sqrt{\mu_0/\epsilon_0} \approx 120\pi \, \Omega$, and

$$\epsilon_{\text{eff}} = \frac{1 + \epsilon_r \tilde{K}}{1 + \tilde{K}} \approx (1 + \epsilon_r)/2 \quad (4.4)$$

is approximately equal to the average of the free space and substrate dielectric constants and gives the speed of propagation $v_{\text{eff}} = c/\sqrt{\mu_{\text{eff}}\epsilon_{\text{eff}}} \approx c/\sqrt{\epsilon_{\text{eff}}}$ for nonmagnetic substrates.

Dielectric Substrate

To evaluate these expressions, we need to know the dielectric constant of our substrate. We chose a sapphire (Al_2O_3) substrate partially for different reasons. Our lab (with the aid of the Houck lab) has already demonstrated high-Q $\lambda/2$ resonators based on niobium (Nb) on sapphire. Our lab also already had two Nb-on-sapphire wafers but little remaining Nb on silicon (Si). Sapphire is also known to allow much higher internal quality factors (i.e., smaller linear loss γ_2 in the context of previous chapters). The choice of sapphire leads to some minor extra work in the fabrication process (it is harder to dice into chips and can lead to charging problems under a scanning electron microscope [SEM] and during e-beam lithography), but as described later these are overcome somewhat easily. The substrate originally came as a $53 \times 53 \text{ mm}^2$ square wafer of $h = .5 \text{ mm}$ thick polished c-plane Sapphire substrate of 5N purity from CrysTec Kristalltechnologie (then, $t = 200 \text{ nm}$ of Nb was sputtered on top by Star Cryoelectronics in a 2×2 square inch region). Sapphire in fact has an anisotropic dielectric constant which is different along different axes. For our c-plane-oriented crystal

substrate, we must in fact substitute an effective permittivity given by [64]

$$\epsilon_{r,\text{eff}} = \sqrt{\epsilon_{x,y} \cdot \epsilon_z} = \sqrt{9.3 \cdot 11.5} \approx 10.34 \quad (4.5)$$

and an effective height

$$h_{\text{eff}} = \sqrt{\frac{\epsilon_{x,y}}{\epsilon_z}} \cdot h \approx 0.90h \quad (4.6)$$

(the first of these modifications is much more important than the second).

We would like the centerpin to be wide enough to perform accurate photolithography while thin enough that superconducting vortices do not become trapped there³ (although, we will employ sufficient magnetic shielding so that the latter is no longer a limiting factor on our centerpin width). We also want the gap size to be as small as reasonable with photolithography, so that the electromagnetic field is confined to a small volume, which should help avoid certain parasitic modes and unwanted decay through surrounding lossy materials. We've seen that $w = 10 \mu\text{m}$ width worked well for $\lambda/2$ Nb resonators for a different experiment, so keeping this value, along with a gap $s = 4.2 \mu\text{m}$ yields $Z_c \approx 49.3 \Omega$, matching the standard 50Ω characteristic impedance of microwave equipment (a close match is not important since the CPW is somewhat decoupled from the laboratory transmission line through a coupling capacitor, although as we will shortly see, a small unaccounted amount of kinetic inductance should actually bring Z_c closer to 50Ω). For a short discussion of what characteristic impedance means, what impedance matching is, and how it relates to the velocity of wave propagation in the CPW, see (the brief) Appendix C.

Inductance

Next, we need to know l , the inductance per unit length, which along with Z_c can be used to calculate c and therefore the $\lambda/4$ resonance frequency. For a CPW, the expression for the familiar magnetic inductance l_m per unit length is, quite conveniently, purely geometrical, determined (through conformal mapping techniques) by the equation [7, 66]

$$l_m = \frac{\mu_0}{4} \frac{K(k')}{K(k)}. \quad (4.7)$$

For our designed ratio of $w/b \approx .543$, this yields $l = 391 \text{ nH/m}$. We can now indirectly calculate the capacitance per unit length via the relation $c = l/Z_c^2 \approx 1.62 \times 10^{-10} \text{ F/m}$,

³When an imperfect strip of thin superconducting film of width w is cooled through its critical temperature, the Meissner expulsion effect will completely occur only below a critical field $B_m \approx \Phi_0/w^2$ [65]. A width of roughly $5 \mu\text{m}$ would correspond to Earth's magnetic field. Otherwise, vortices could lead for example to flux noise in the SQUIDS.

justifying the comment we made in the previous chapter about the relative magnitudes of the cavity and SQUID capacitances.

However, in superconducting resonators, one cannot a priori neglect *kinetic inductance* associated with the inertia of Cooper pairs. Classically, kinetic inductance can be intuitively understood by comparing the equation for the energy stored in an inductor by a current with the kinetic energy associated with a current – both are proportional to the current squared (the latter because kinetic energy depends on velocity squared). Usually, in normal metals we don't have to worry about the energy stored in the motion of charge carriers, because it is dissipated into the metal on the timescale of scattering. However, in superconductors this can have a noticeable effect. It can be shown that the kinetic energy associated with the superconducting current in our centerpin is given by [7, 53]

$$E = \int_V \frac{1}{2} n_s m v^2 dV = \int \frac{1}{2} \frac{n_s m}{A e^2} I^2 = \frac{1}{2} \mu_0 \lambda_L^2 \frac{d}{A} I^2, \quad (4.8)$$

where $A = wt$ is the cross-sectional area, n_s is the density of Cooper pairs, and $\lambda_L = 1/\sqrt{\mu m/n_s e^2}$ is the so-called London penetration depth, the distance to which a magnetic field penetrates into the superconductor – essentially where supercurrents flow. Identifying the coefficient of $\frac{1}{2} I^2$ with the kinetic inductance (after conformal mapping taking into account the CPW geometry), it can be shown that the kinetic inductance per unit length l_k of the CPW is [66]

$$l_k = \mu_0 \frac{\lambda_L^2}{wt} g(s, w, t), \quad (4.9)$$

where

$$g(s, w, t) \equiv \frac{1}{2k^2 K(k)^2} \left[-\ln \left(\frac{t}{4w} \right) + \frac{2(w+s)}{b} \ln \left(\frac{s}{w+s} \right) - \frac{w}{b} \ln \left(\frac{t}{4b} \right) \right] \approx 3.1 \quad (4.10)$$

for our chosen geometrical parameters. This inductance depends somewhat on temperature and magnetic field due to the London penetration depth, and in fact this formula assumes that $t < \lambda_L$, but it can give us an order of magnitude approximation. Assuming $\lambda_L \sim 100$ nm in our Nb film [7], we estimate $l_k/l_m \approx 5\%$. We then have $l = l_m + l_k \approx 400$ nH/m, pushing Z_c to just over 50Ω . Using equation (4.1), we see that choosing a resonator length of 3.8 mm will yield an uncoupled (i.e., $C_\kappa = 0$) resonance frequency of 8.1 GHz.

Coupling Capacitance

The last, but by no means least, design parameter for the CPW is the coupling capacitance and its associated finger capacitor geometry. The capacitance C_κ determines the coupling

between the CPW and the transmission line that we use to send signals into and out of the resonator, as depicted in Figures 3.2(a) and 4.1(a). More precisely, it determines the coupling strength γ_1 (as assumed to exist in the context of quantum optics in Figure 2.1) as used in previous chapters.

How can we extract a coupling constant from a capacitor? To do this, we will use energy considerations to connect the languages of quantum optics and electrical engineering. As originally defined in the quantum Langevin equation (2.23) with a single port $\gamma = \gamma_1$, (setting input and output signals to zero), γ_1 can be interpreted as the rate of energy decay out of the resonator, relative to the energy stored in the resonator. To see this, treat A as a coherent-limit c-number, so that $|A|^2$ is the stored energy (normalized to the energy of a single photon). Identifying the time-derivative of this with the rate of energy decay through the port associated with γ_1 , we see that the dissipation rate (in angular frequency) normalized to $|A|^2$ is 2γ (the factor of 2 comes from the product rule).

We can perform a similar analysis for the CPW circuit. Suppose we have initially excited the coupled CPW oscillator and allow it to resonate freely. The electric energy stored in the CPW is

$$E_{\text{elec}} = \frac{1}{2}c \int_0^d \langle V^2(x, t) \rangle dx, \quad (4.11)$$

where $\langle \cdot \rangle$ denotes a time average. For $C_k \ll C_{\text{cav}}$, the normal modes of the CPW resonator are very close to those of the uncoupled $\lambda/4$ resonator, so that for the fundamental mode the integration takes place over one quarter of a sinusoidal envelope which has its maximum voltage near the coupling capacitor, leading to $E_{\text{elec}} = \frac{1}{2} \cdot \frac{1}{2}cd\langle V(0)^2 \rangle$, where the additional factor of $1/2$ comes from taking a spatial average over a quarter wavelength. As usual, the average magnetic energy stored is equal to the electric energy, yielding the total

$$E = \frac{1}{2}C_{\text{cav}}\langle V(0)^2 \rangle. \quad (4.12)$$

Next, we calculate the rate of energy loss through the coupling capacitor. Assuming that the capacitor dominates the CPW impedance (as we will see, we'll choose $1/\omega C_\kappa$ to be well above 50Ω), this is simply given by the power flowing out of the CPW and into the laboratory transmission line [the red transmission line in Fig. 3.2(a)] of characteristic impedance $Z_t \approx 50 \Omega$. Because an infinite (or properly terminated) transmission line acts like a resistor with a resistance equal to its characteristic impedance (as in Appendix C), since $I = \omega_0 C_\kappa V(0)$ is the associated current flowing out into this load on resonance we can write the dissipated power as

$$P = \langle I^2 \rangle Z_t = (\omega_0 C_\kappa)^2 \langle V(0)^2 \rangle Z_t, \quad (4.13)$$

so that we obtain

$$2\gamma_1 \equiv \frac{P}{E} = \frac{2\omega_0^2 C_\kappa^2 Z_t}{C_{\text{cav}}} = \frac{4}{\pi} Z_t Z_c C_\kappa^2 \omega_0^3, \quad (4.14)$$

where in the last equality we have used $Z_c = \sqrt{L_{\text{cav}}/C_{\text{cav}}}$ along with equation (3.38), which for a $\lambda/4$ resonator says $\omega_0 = \pi/(2\sqrt{L_{\text{cav}}C_{\text{cav}}})$.

We would like γ_1 to be small enough that the high- Q approximation holds reasonably well, while at the same time large enough that the gain-bandwidth product (2.70) of our paramp is useful, and also large enough that the system can respond fast enough to amplify pulsed readout tones used to probe cQED systems (usually on the order of a microsecond [or less with the aid of a paramp] in duration and 10 nanoseconds in risetime). The latter requirement is easily fulfilled for $\gamma_1/2\pi \gtrsim 5$ MHz. For a simultaneous gain of, say, 25 dB and a bandwidth of 2 MHz, equation (2.70) says that $2\gamma_1/(2\pi) = 30$ MHz is necessary. Plugging this into (4.14), along with $Z_c \approx Z_t = 50 \Omega$ and $\omega_0/(2\pi) = 7$ GHz yields $C_\kappa \approx 26.5$ fF. Plugging this value into equation (4.1) for the loaded resonator frequency then yields a resonance frequency of 7.9 GHz. To obtain such a capacitance, we must come up

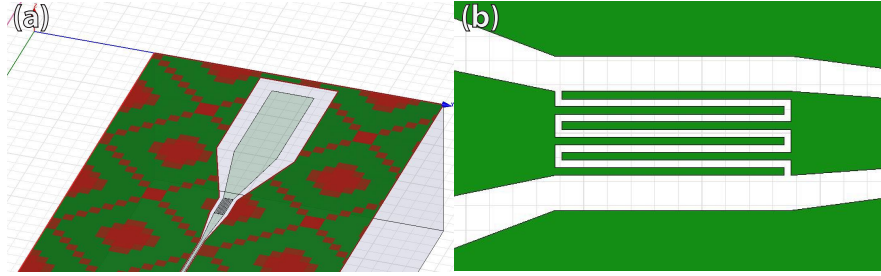


Figure 4.2 (a) Screenshot of ANSYS Maxwell software used for electrostatic simulation of capacitances. (b) 3+3 finger capacitors design used for paramps.

with the necessary physical geometry for the coupling capacitor. Using the commercial electromagnetic simulation software ANSYS Maxwell, it was found that for reasonable finger capacitor widths and separations, a 3+3 finger design as shown in Figure 4.2(b) gave capacitances in the 20-30 fF range. Using equal finger widths and separations of $3.3 \mu\text{m}$ and adjusting the lengths of the fingers (near $100 \mu\text{m}$) allowed the capacitance to be tuned to the desired value.

Photolithography

The technique of photolithography was used to make the resonators (along with the coupling capacitors) by patterning the pre-existing Nb on our chip. Some of the equipment used in this process is shown in Figure 4.3. The first step in the process was to pattern a “mask”

with a Heidelberg DWL66 ultraviolet laser writer at PRISM MNFL. This machine takes a design file and various parameters as input and exposes the desired pattern on a layer of photoresist that comes pre-deposited on top of a chrome-coated soda-lime square glass wafer. A 4 mm write head was used, which can nominally achieve a minimal feature size of ~ 800 nm, sufficient for our resonators. The exposed areas of photoresist were then dissolved away to expose the chrome below, by rinsing in a known amount of developer in a Laurell EDC650Mz Spin Processor, and then etching the exposed chrome with a similar tool. The remaining resist is then dissolved away with a resist-stripping solution, rinsed with water, and blown dry with a nitrogen gun. Before use it was further rinsed with acetone and isopropyl alcohol (IPA) and blown dry with a nitrogen gun.

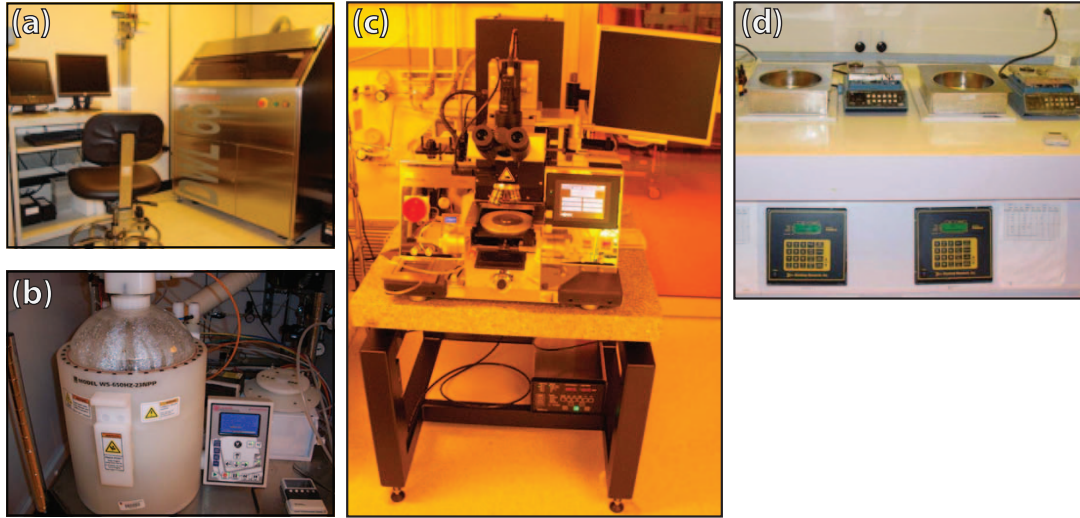


Figure 4.3 Photographs of equipment used for photolithography in PRISM MNFL cleanroom. All images are from the PRISM website. (a) Heidelberg DWL66 laser mask writer. (b) Laurell EDC650Mz Spin Processor. (c) Karl Suss MJB4 Mask Aligner. (d) Headway spinners.

The next step is to transfer this pattern onto our chip. To do this, the wafer was first cleaned by sonicating for 3 minutes in acetone followed by 3 minutes in IPA, immediately followed by blow-drying with a nitrogen gun. A layer of S1818 photoresist is then deposited on the wafer by vacuum-mounting it on a spinner, depositing enough to cover a good portion of the chip, and then spinning the resist at 4500 rpm for 60 seconds (with a 4500 rpm/s ramp-up), which corresponds to a thickness of roughly $2\ \mu\text{m}$. The resist is then immediately baked on a hotplate at 115°C for 2 minutes. We note that all photolithography for this thesis was performed on a single 1×1 square inch quarter of the 2×2 square inch Nb-on-sapphire wafer mentioned earlier, including the paramp resonators with gaps for SQUIDs

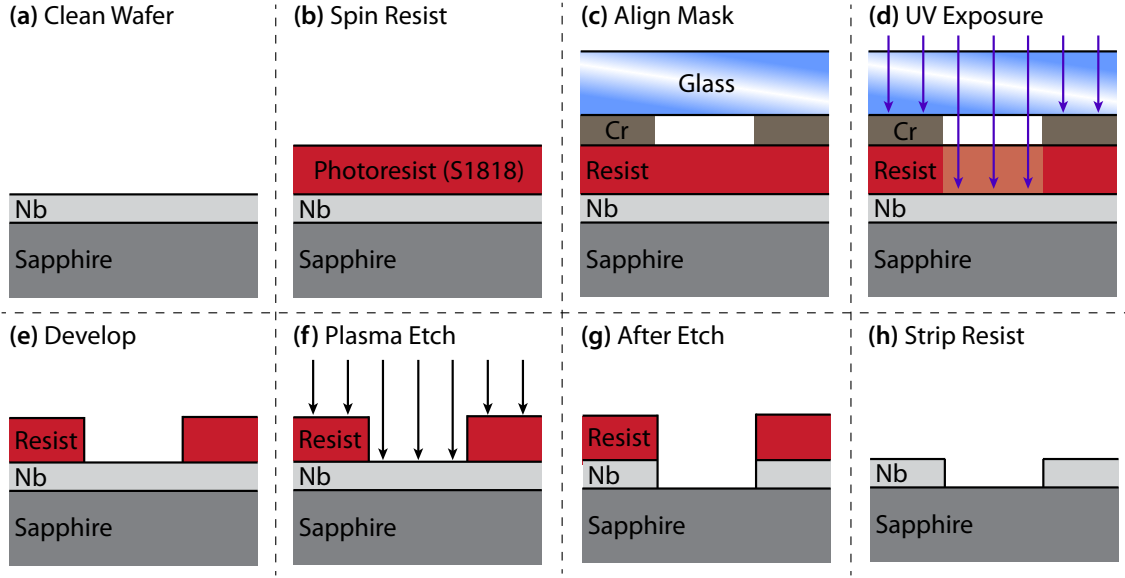


Figure 4.4 Idealized illustration of photolithography steps. Note: thicknesses are not to scale.

(described shortly) and chips specifically for the development and testing of SQUIDs (also described later). Accordingly, the pattern on the mask was a 3-by-10 grid of multiple designs spaced apart by $(\Delta x, \Delta y) = (7.25 \text{ mm}, 2.25 \text{ mm})$ to fill the wafer (which is later diced into individual chips). This has the advantage of diminishing the beading of thick photoresist on the edges of the chip, which could be more of a problem for smaller chips. It also of course has the advantage of only needing to align a mask and perform photolithography once. The photomask is described in Figure 4.5.

The resist-coated wafer is exposed to UV light in a Karl Suss MJB4 mask aligner, which exposes the sample through the photomask made earlier, in hard contact mode (which has a nominal best resolution of $1 \mu\text{m}$) with 5 s contact time and 5 s exposure time. Before mounting the mask in the aligner, it is a good idea to quickly blow it with a nitrogen gun in case there are any deposited airborne particles (even though the PRISM lithography room is a class 100 clean room⁴). The exposed areas of resist are then dissolved away by dipping the wafer in MF-319 developer for 90 seconds, followed by a quick rinse in DI water and nitrogen blow dry. The wafer was then observed under a microscope before the final niobium etching step. It was noticed that resonator finger capacitors came out better in the developed resist away from the lower corners of the wafer, with fingers on chips near the corner of the chip having a distorted width and edge profile (see Figure 4.6 for

⁴This is according to the PRISM website, and means (according to a now outdated standard) that there are fewer than 100 particles with greater size than 0.5 micron per cubic foot of air.

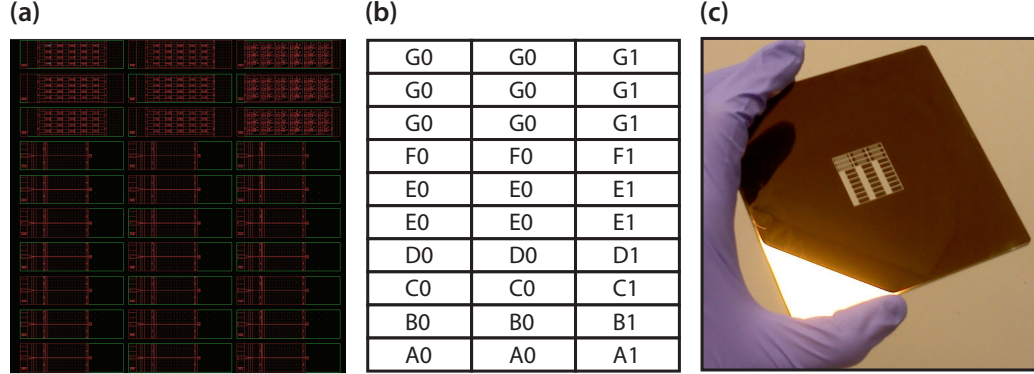


Figure 4.5 (a) Broad overview of .gds file of “Paramp_Mask_1” photomask made for paramp project. (b) Labels indicating the contents of the various chip designs on the mask. The letters A through F followed by the number of “0” have 3+3 finger capacitors (this column appears twice because it is our target), while those followed by the number “1” have 4+4 finger capacitors, for an approximate $2\gamma_1 \approx 30$ MHz and 50 MHz respectively at the desired operating point of 6.85 GHz. “A” denotes resonators with no gaps at the ends for SQUIDs (i.e., bare $\lambda/4$ resonators), “B” denotes a gap for ~ 1 SQUID, “C” for ~ 2 SQUIDs, “D” for ~ 3 SQUIDs, “E” for ~ 4 SQUIDs (this row is repeated since as discussed later it is our target), and “F” for ~ 5 SQUIDs. “G0” (repeated six times) is a chip for dose testing of SQUID e-beam lithography (as described in the next section). Each such chip contains 10 sites for a 4-SQUID array dose test and 10 sites for a single SQUID dose test. G1 (appearing three times) is a chip for probing the normal resistance of the junctions via a four-probe measurement to predict the Josephson energies (as described in the next section). (c) Picture of the photomask (inverted when viewed from chrome side).

photolithography result images). This is possibly due to the visible beading of resist near the edges (especially the corners) of the wafer, which may have led to uneven contact with the mask during exposure.

The niobium etch was then performed with an STS ICP Metal Etcher, which uses a beam of plasma to etch metal. This has the advantage of being directional (anisotropic) to produce nearly vertical Nb sidewalls. The process is also largely automated. For etching through 200 nm of Nb, the predefined recipe “Houck Nb” was used. After stripping the remaining resist, the wafer was covered in a protective layer of thick photoresist (AZ 4330) and then diced into 2×7 mm² chips with an ADT proVectus 7100 Wafer Saw. As sapphire is a relatively hard material to cut, a recipe with several passes at different cut depths had to be used.

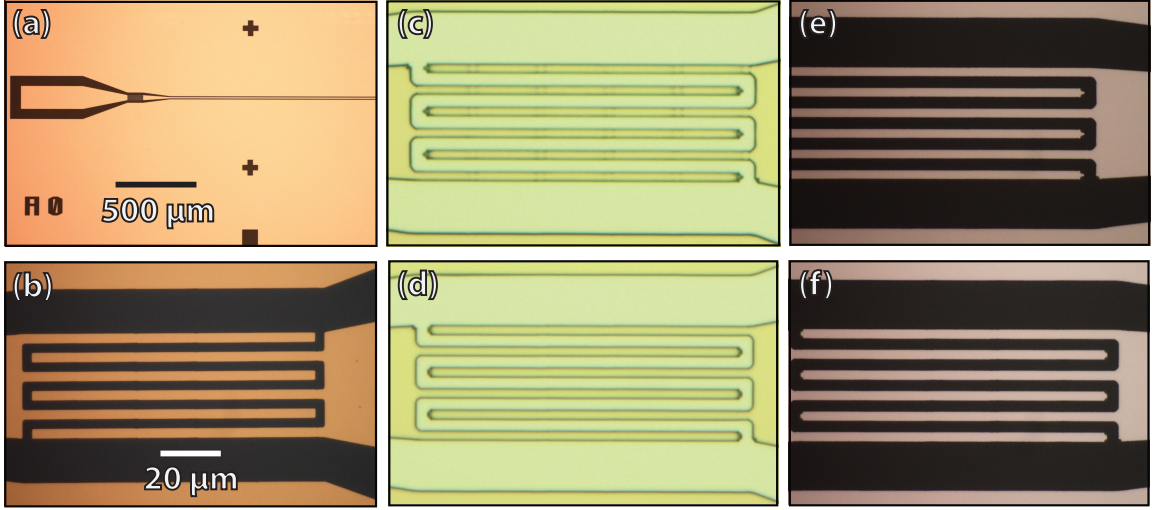


Figure 4.6 Optical images of resonator photolithography results. (a) Broad view of left side of $\lambda/4$ test resonator chip. The crosses and square in which Nb is etched form alignment marks for e-beam lithography (as described later) on all chips. (b) Finger capacitors (chrome) on photomask. (c) Developed resist for bare $\lambda/4$ resonator test chip near lower-left corner of wafer. The resulting pattern is imperfect (the capacitor in the chip right at the corner is worse and was not used). (d) Developed resist for paramp chip near center of wafer. The resulting pattern is less imperfect. (e) The resulting Nb capacitors after etching and resist strip of (c). (f) The corresponding capacitors for (d).

4.1.2 Fabrication of SQUIDs

Because the feature sizes of SQUIDs are generally on the order of 100 nm or smaller, photolithography is no longer sufficient – one can instead use electron beam lithography, in which a focused beam of electrons is used to beat the diffraction limit of light⁵. In several ways that will become apparent (especially with the tools used in this thesis work), e-beam lithography is much more difficult (and more time consuming) than photolithography.

⁵Electrons, unlike photons, are massive, and therefore have a different dispersion relation between their energy and momentum (and therefore their deBroglie wavelength, which characterizes the length scales at which well-defined features can be exposed via bombardment by such particles). Namely, non-relativistic massive particles have kinetic energy $E = \hbar^2 k^2 / 2m$, whereas photons have $E = \hbar c k$, where $k \propto 1/\lambda$ is the wavenumber characterizing its momentum. This means that for an energy of, for example, 10 keV, electrons can obtain roughly ten times a smaller wavelength than a photon of the same energy. This is also one of the crucial operating principles of electron microscopes.

Electron Beam Lithography

In a nutshell, electron beam lithography uses a different kind of resist (known as “e-beam resist”) that is sensitive to bombardment by electrons of certain energies, rather than to UV light. The Raith eLiNE e-beam lithography tool used in this thesis is essentially a scanning

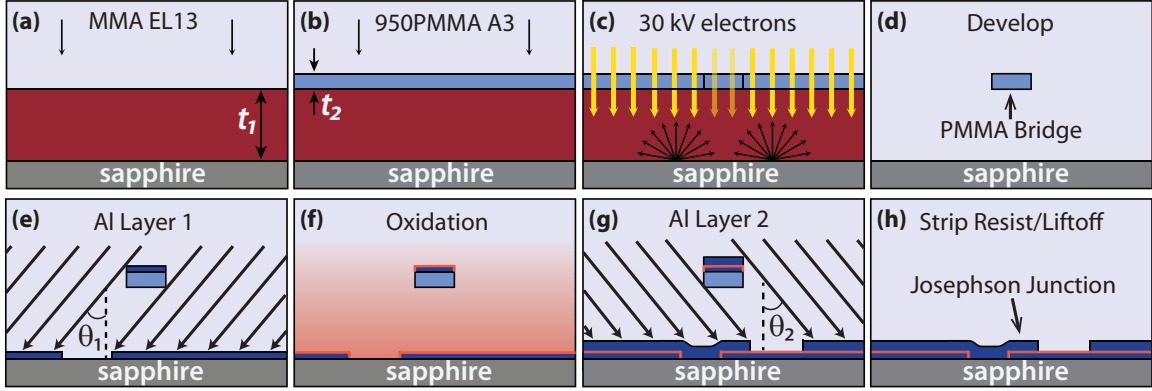


Figure 4.7 Rough illustration of the Dolan bridge technique used for paramp SQUID fabrication, leaving out Al charge layer step. Figure based on a similar one in [58]. (a) Spin bottom layer of e-beam resist. (b) Spin thin top layer of less sensitive resist. (c) Expose pattern to controlled beam of electrons. Faded yellow arrows in the central region denote a lower “undercut” dose intended to only significantly expose the bottom layer of resist. (d) Develop exposed resist in MIBK. (e) Evaporate first layer of aluminum, at angle θ_1 . (f) Expose surface to oxygen to create a thin layer of aluminum oxide. (g) Evaporate second layer of aluminum, at angle θ_2 . (h) Strip unwanted resist and lift off unwanted aluminum on top of resist.

electron microscope that has been modified and hooked up to control electronics to allow the beam to scan over a chip to expose user-defined patterns with a user-defined charge dose. The most common method of making Josephson junctions with e-beam lithography is known as the Dolan bridge technique [67], a bilayer process that is illustrated in Figure 4.7. In this process, a suspended bridge of thin resist blocks evaporated aluminum from being deposited on the substrate in its shadow. By evaporating metal at two different angles and exposing the metal to oxygen between these two evaporations, one can create Josephson junctions out of aluminum and aluminum oxide. The basic procedure is as follows. First, the photoresist protecting the $2 \times 7 \text{ mm}^2$ diced chip is stripped off and the chip is sonicated for 8 minutes in acetone and then 8 minutes in IPA. Next, a layer of copolymer resist MMA EL13 (methyl methacrylate, ethyl-lactate 13%) from *MicroChem* is spun at 5000 rpm (with a 1000 rpm/s ramp-up) for 60 s to a thickness of about 600 nm. The MMA layer is immediately baked on a hotplate at 175 °C for two minutes. The chip is then allowed to cool on the spinner’s vacuum chuck for 1 to 2 minutes so that there are no

problems depositing the second layer of thin resist. This second layer is 950PMMA A3 [i.e., poly(methyl methacrylate), molecular weight 950k, 3% in anisole] from *MicroChem* spun at 4000 rpm (with a 1000 rpm/s ramp-up) for 60 s to a thickness of ~ 120 nm. The chip is then baked for 30 min at 175 °C, and then checked under an optical microscope to ensure that no damage to the surface has accidentally occurred.

When using a sapphire substrate, there is one more step between depositing resist and writing a pattern. Because sapphire is a good insulator, it is susceptible to charging under an electron beam. This is detrimental to writing precise patterns with such a beam, which can move around under the influence of such charge. The niobium on top is also a relatively poor conductor and will in addition have poor electrical contact with the metal clip holding the chip in place during e-beam lithography, so that there is no sufficient conduction path off of the chip for the excess charge. To circumvent this, a thin (12 nm) anti-charging layer of aluminum is evaporated onto the surface of the chip before writing the pattern. Both thermal and e-beam evaporation (depending on the availability of the evaporators) were used successfully for this. As a minor note, it was found that for similar evaporator vacuum pressures, ebeam evaporation yielded a less granular aluminum layer than thermal evaporation did and also a lesser rate of cracking under the Raith's 30 kV, 20 nm spot size electron beam [see Figure 4.8(c) and 4.8(d)], although the reason for this difference is not known, as the two methods were performed in different evaporators and only a few times each. Figure 4.8 illustrates a few parts of the Raith process. The chip is first mounted on a sample holder with a metallic clip gently clamping the very edge of the chip, and loaded into the main vacuum chamber via a load-lock system. For SQUID fabrication, the beam was set to use a 20 μm aperture, 30 kV energy and 11 mm working distance. The SEM is then focused on ~ 50 nm gold particles deposited on the corner of the chip in order to optimize stigmation and aperture alignment. Then various steps are taken to align the system's coordinates with the chip axes, and define the plane of the chip along with a coordinate system using a three-point focusing method. Such three-point alignments were aided by the presence of square- and cross-shaped alignment marks from the previous photolithography step. One must be careful not to accidentally expose critical regions of the chip. Since the aluminum anti-charging layer tended to crack under a concentrated beam, the edges of the cracked aluminum were used to focus quite nicely on the surface for three-point alignment (the alternative, which was found to be quite difficult, was to "burn" a spot on the resist and focus on that). For thermally evaporated aluminum charging layers, it was also possible to focus on the relatively granular surface. After performing a write field alignment procedure to calibrate the coordinates and beam deflection, the beam current was measured via a Faraday cup on the sample holder in order to calibrate the exposure

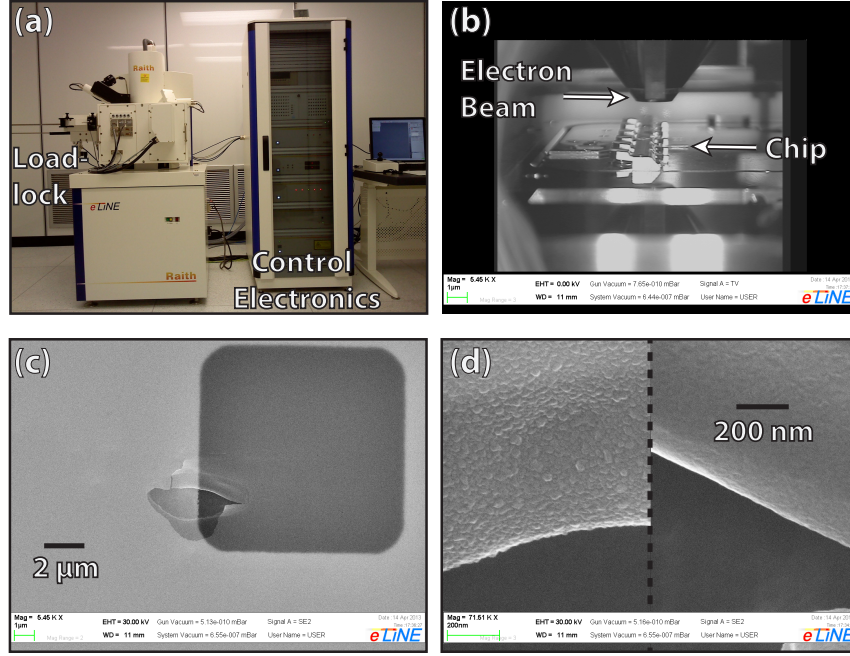


Figure 4.8 (a) Picture of the Raith eLiNE e-beam lithography system. (b) Picture of the inside of the vacuum chamber in which the chip resides during the e-beam exposure. (c) Cracked aluminum on one of the small alignment marks, conveniently used for focusing during three-point alignment. (d) High-magnification of cracked aluminum edge, for two different samples (left: thermally evaporated aluminum, right: e-beam-evaporated aluminum).

“dose.” Then the desired patterns were written from a user-defined .gds file and user-defined dose. At a given energy, the dose refers to the amount of charge deposited per area within the region in question. To create PMMA bridges, the region around the bridges needs to be fully exposed without significantly exposing the PMMA bridge region [green and blue boxes respectively of the SQUID-array design shown in Figure 4.9(b)]. However, it is also necessary for the MMA under the PMMA bridge to be exposed, without the PMMA on top itself being exposed above its threshold. Since the MMA has a relatively low threshold dose of around $60 \mu\text{C}/\text{cm}^2$ for a 30 kV beam, an “undercut” box of slightly over this dose was used at the bridges. Several rounds of dose tests were needed to figure out the optimal doses for the various exposure regions. An idea of what this looks like is given by Figure 4.9 (c) through (e), which show some of the results of the first (most coarse) dose test. This and all future dose tests used a constant dose of $70 \mu\text{C}/\text{cm}^2$ for the undercut regions. The first dose test gave the entire main SQUID exposure a single base dose to be proximity-corrected. Proximity correction is a built-in feature of the Raith software that attempts to correct for the *proximity effect*, in which primary beam electrons accelerated into a region

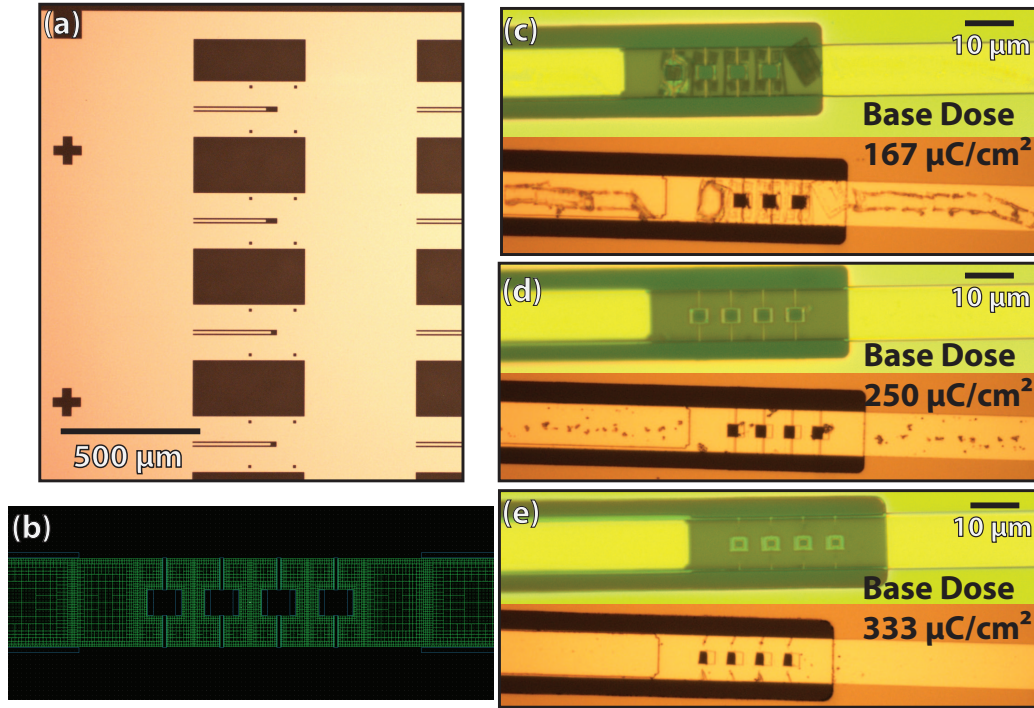


Figure 4.9 Results of first (coarse) dose test. (a) Partial image of one of the dose test chips on which dose tests of SQUID fabrication were performed. (b) Proximity-corrected four-SQUID design displayed in LayoutEditor. Smaller and denser green boxes correspond to higher doses in the main exposure. Blue boxes are low- and constant-dose undercut regions. (c) Underdeveloped resist (top) and resulting SQUID array after liftoff. Base dose used in proximity-corrected exposure indicated on right. (d) Best dose in first dose test for a proximity-corrected main exposure. (e) Result of overexposure (high dose). The PMMA bridges have visibly collapsed.

of resist can scatter and expose nearby regions of resist. As can be seen in Figure 4.9, with this dose strategy, by the time the base dose becomes high enough to sufficiently expose the regions directly surrounding the SQUIDs and also the Nb-Al overlap region, the PMMA bridges are damaged due to the nearby exposure. In a second round of dose tests, the Nb-Al overlap region was given its own large and constant dose of $390 \mu\text{C}/\text{cm}^2$, which was sufficient to circumvent any significant specks of undeveloped resist. In this second dose test, the SQUID region was still proximity-corrected, and had fewer undeveloped spots of resist near the SQUIDs. The first two dose tests were performed with PMMA bridges of length $3.5 \mu\text{m}$ and $\sim 350 \text{ nm}$ width. These 10:1 aspect ratio bridges would occasionally collapse with a dose that previously produced stable bridges. Reducing the bridge length a little bit made them more robust and also significantly reduced the amount of specks of undeveloped resist near the SQUID loops. Note that all dose tests were performed with

the exposure done in a region that emulates the actual environment used in a real paramp device (i.e., a centerpin and surrounding Nb ground plane), since the optimal dose could be sensitive to a significantly different immediate surrounding environment.

After exposure, the resist must be developed. The Al anti-charging layer is first removed by dipping the chip in AZ 300 MIF for 70 seconds, followed by a short rinsing dip in DI water and nitrogen blow-dry. The resist is then developed by gently dipping the chip in 1:3 MIBK:IPA for 50 seconds, followed by a 10 second IPA dip and nitrogen blow-dry. Care was taken not to collapse the bridges by swirling the chip or using too much pressure on the N₂ gun. Again, sample optical images of exposed resist are shown in Figures 4.9 (c) through (e). The next important step in SQUID fabrication is the double-angle evaporation illustrated in Figure 4.7 (e) through (g). For this, the sample is loaded into a metal evaporator on a stage that is capable of tilting at user-specified angles. Before the evaporation, a moderately strong plasma etch is performed to both clean the surface (for example organic residue and oxide) and attempt to shave the edge of the niobium step over which the evaporated Al must transition from the substrate to the niobium in a continuous manner. This extra etch was found not to damage the PMMA bridges, but it is not clear whether or not it smoothed the niobium edges [an SEM image of one of the resulting overlaps, which were found to be satisfactory for evaporation angles of $\pm 45^\circ$, is shown in Figure 4.10(c)]. The Al-Nb overlap was chosen to be large ($\sim 600 \mu\text{m}^2$) so that at paramp operating frequencies, the capacitance essentially acts as an ac short even if there is little dc contact. Large evaporation angles were used for the sake of Al-Nb contact and also to obtain a large SQUID area for desired Josephson energy, as will be discussed shortly. Figure 4.10 shows environmental SEM (in environmental mode, to avoid charging) images of the result of one of the dose tests. After the double-angle evaporation, the entire chip is covered with aluminum. We can “lift off” the unwanted aluminum (which is sitting on top of a bilayer of e-beam resist) by letting the chip sit in acetone. The junction aluminum deposited directly on the sapphire substrate and niobium will remain attached, whereas when the resist is stripped by the acetone the aluminum on top of it will be lifted off. Liftoff was performed for 3 hours at 70 °C. Care must be taken to make sure the acetone does not evaporate and expose the chip to air, as liftoff can be difficult or impossible if that happens. After 3 hours, a pipette is used to squirt the chip 50-100 times so that the aluminum visibly strips off, ideally in one piece (generally, it was found that smaller pieces would stick to the edges longer than the bulk). The chip is then sonicated for 5 seconds, dipped in IPA for 5 minutes, sonicated for 2 seconds, and then blown dry with a nitrogen gun. After optical inspection, the sample is now ready for resistance tests or packaging, depending on the purpose of the chip.

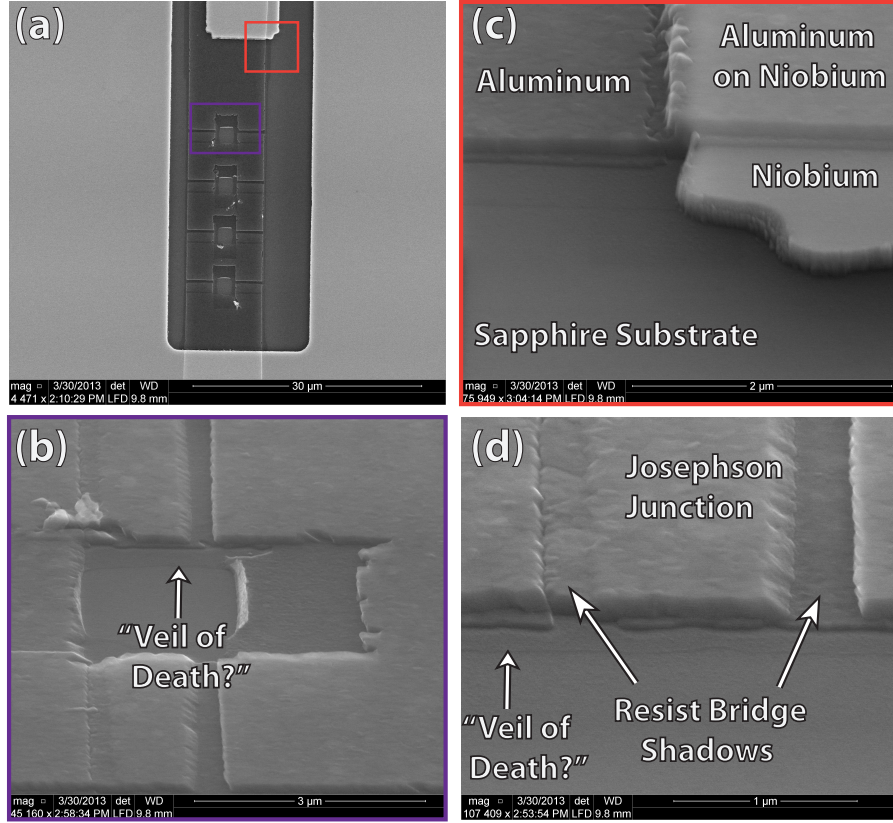


Figure 4.10 Environmental SEM images of a SQUID array from the second round of dose tests. (a) Overview of SQUID array and overlap with Nb centerpin and ground plane (the e-beam alignment was a little off on this run). Small artifacts presumably from specks of undeveloped resist are visible. (b) Side view of one of the SQUID loops. The thin film seen is possibly the “veil of death” (seen and colloquially named so by other groups [7]), potentially due to aluminum scattered by residual outgassing of resist. The rough edges of the SQUID loops are possibly due to imperfect liftoff or the brief sonication used after liftoff. (c) Side view of Al-Nb overlap. (d) Side view of one of the Josephson junctions.

SQUID Characterization

With optimal doses in hand, we can start to think about tuning the SQUID parameters to obtain the desired Josephson energies. In accordance with Figure 3.3 and equation (3.34), an effective SQUID energy of 1000 GHz (1 THz) would allow us to reach a compromise between tunability and stability, reaching the desired operating frequency of 6.85 GHz at around three-quarters of the maximum SQUID energy. To have a reasonable critical power in accordance with equations (2.47) and our discussion in section 3.2.2, an array with four SQUIDs (therefore each of energy 4 THz) was found to be sufficient to obtain a reasonably high critical input power of -100 dBm at an operating frequency of 6.85 GHz.

How can we predict the SQUID Josephson energies? Remarkably, it can be shown [53,68] that the critical current of a Josephson junction obeys the *Ambegaokar-Baratoff relation*

$$I_c = \frac{\pi \Delta(T)}{2eR_n} \tanh \left(\frac{\Delta(T)}{2k_B T} \right), \quad (4.15)$$

where $\Delta(T)$ is the (temperature-dependent) superconducting gap and R_n is the *normal state* resistance, which is measurable at room temperature! This resistance is very sensitive to the junction (i.e., oxide) thickness, and should also scale inversely with the area of the junction. To get the desired resistance ($73 \, \Omega$ per junction in a four-SQUID series array), we can therefore fabricate various SQUID sites while varying junction geometry and/or oxidation time. Based on the Houck lab's standard recipe for much smaller junctions (resistances of kilohms), a naive extrapolation by junction area would tell us that a junction area of roughly $4 \, \mu\text{m}^2$ is desired, which is why relatively long bridges and large evaporation angles were chosen. This neglects edge effects in the geometry, but is a reasonable starting point. This estimate turned out to perform better than expected. Two series of resistance test chips were iterated, in which a four-probe lock-in amplifier measurement (at 80 Hz) was used to measure the resistance of SQUID arrays of varying bridge lengths (and hence junction areas). A four-probe measurement was used because the desired SQUID resistances are relatively low (less than $100 \, \Omega$), and we want to isolate only their resistance by measuring the voltage drop across them with a known amount of current flowing through them. Furthermore, niobium is known to have a very high contact resistance when probed with the small electrodes of our Lakeshore probe station, so aluminum electrodes were fabricated over the initially deposited niobium electrodes [see Figure 4.11(a)]. For the electrode e-beam lithography step, an aperture of $120 \, \mu\text{m}$ was used for the sake of time. Care was taken to remain electrically grounded (through a wrist-strap and BNC tees that could be shorted at one end when contacting the probes) so that the SQUIDs do not become damaged from a large electrical discharge⁶. Figure 4.11(d) shows the measured four-probe resistances. The slope of the data with respect to bridge length makes sense, with the resistance roughly halving as the junction area doubles. These resistances are in the desired range ($\sim 150 \, \Omega$ for a series of four SQUIDs).

⁶Unless one is in the mood for fried calamari and bad puns.

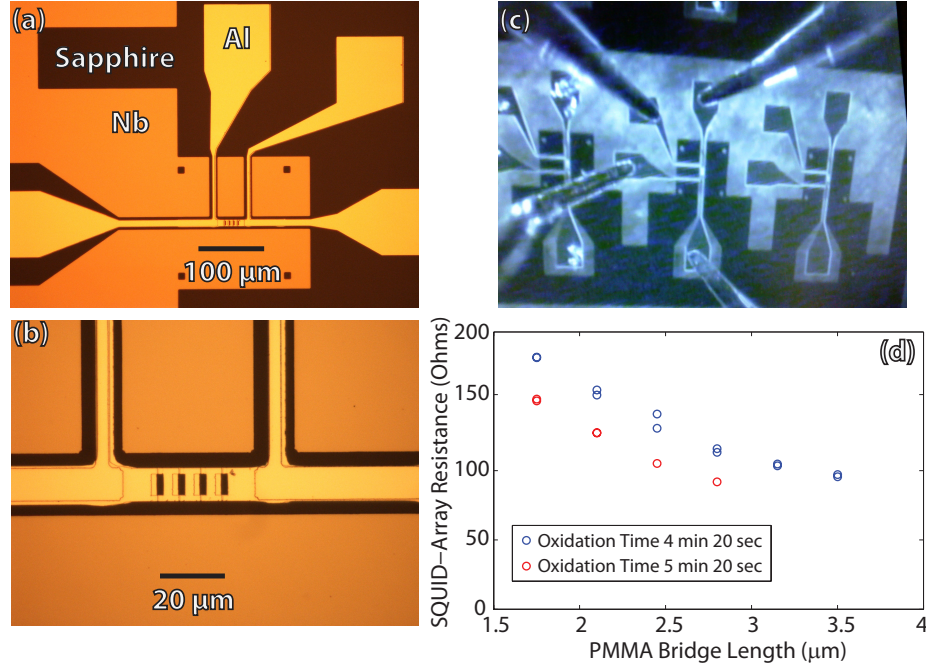


Figure 4.11 (a) Optical image of a four-probe resistance test site. (b) Closeup of electrode overlaps near SQUID array. (c) Picture (of a picture) of a four-probe measurement being performed with the Lakeshore probe station. The probes are manually lowered onto the bond pads for good electrical contact. (d) Results of resistance tests. Note that while the dependence on bridge length makes sense, the dependence on oxidation time was opposite from what would be expected. However, the variation was relatively small, and it seems that both oxidation times already exceed the saturation point of the oxidation process, so that the variation is due completely to unknown (or uncontrollable) variations between the two fabrications (it was checked that junction aging was not the reason.)

4.2 Amplifier Implementation and Characterization

After dialing in on a coupling capacitor, e-beam lithography dose, and SQUID-array resistance, we are ready to try and make a Josephson parametric amplifier. After the junctions are fabricated, the chip must be packaged in a way that allows us to connect the resonator input port to our laboratory equipment. This is done by mounting the chip in a notch of matching size on a custom printed circuit board (PCB) [see Figure 4.13(a)] with silver epoxy⁷. The launch pad leading to the centerpin of the resonator must be connected to

⁷For the epoxy to set, it was necessary to heat the PCB (along with the sample) to 120 °C in a vacuum oven. To make sure this wouldn't change the junction resistances, this was tested on one of the resistance test chips, and it was found that the process increased the resistances by only up to around 10 percent.

the centerpin of our coax, which is done via three wire bonds. A dense array of wire bonds was also used to connect the ground plane of the resonator to the ground of the PCB, in order to avoid unwanted resonances. In general, shorter bonds are desirable (though harder to achieve) because they add less inductance to the circuit and have better high-frequency properties. For the paramp measured in this thesis, extra wire bonds across the middle of the chip connecting the two sides of the ground plane across the centerpin were used to further reduce the chance of spurious modes. A picture of the wire bonding process is shown in Figure 4.12(a) and images of the resulting bonded chip are shown in Figure 4.13(a) through (c).

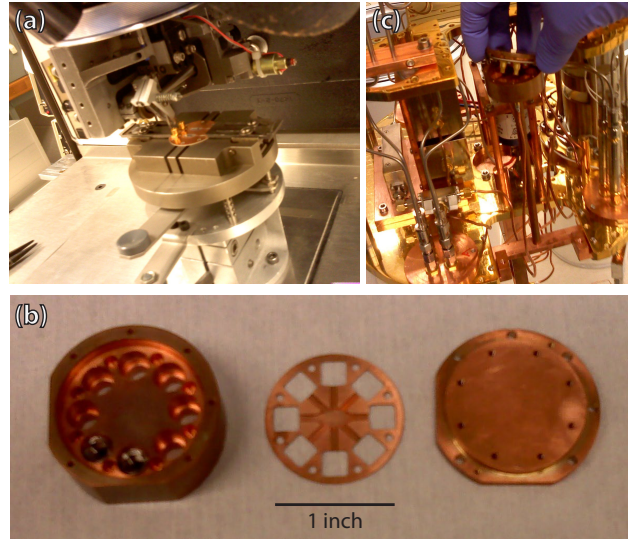


Figure 4.12 (a) Picture of the wirebonder in use. (b) From left to right: octobox, shim, and lid. (c) Illustration of how sample is mounted via surface mount SMP (subminiature coax) connectors and SMP bullets in the fridge via the octobox.

The PCB and sample are then covered with a shim [similar to the one shown in Figure 4.12(b)] and mounted to the cover piece of an “octobox,” which is capable of providing up to 8 SMP connections (hence the name). This reduces the volume that could contribute to unwanted parasitic modes. The cover piece is then mounted on the octobox in a manner that allows for the sample to connect to metal coax cables in the fridge on a rod that will hold it in place in a magnetic shield [see Figures 4.12(c) and 4.13(g)]. Bright field optical micrographs of the paramp device measured in this thesis are shown in Figure 4.13 (d) through (f). For the paramp, a PMMA bridge length of $2\ \mu\text{m}$ was used. The reader may have noticed that the region of niobium ground plane on the right hand side of the resonator has been removed, except for a square region right near the SQUID array termination. This was an attempt to minimize inhomogeneous SQUID-flux coupling that

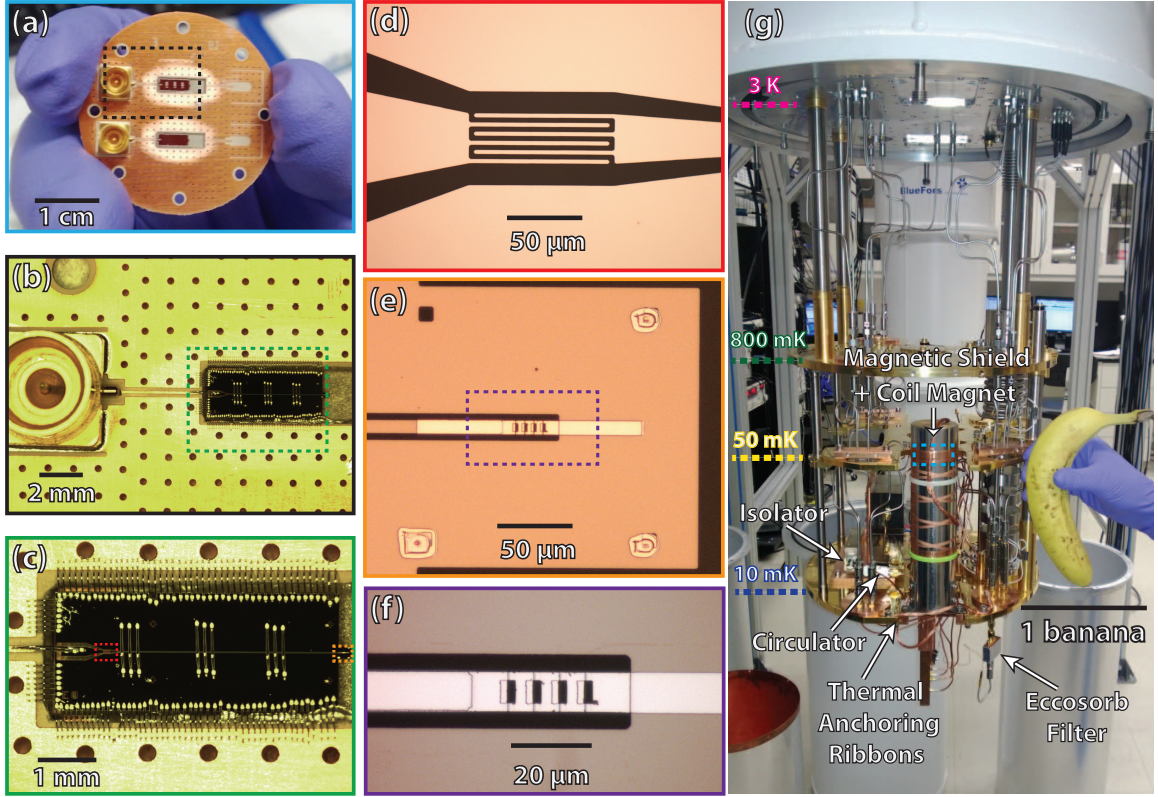


Figure 4.13 (a) PCB with connectors and two paramp samples mounted. The PCB copper directly surrounding the chip is shinier because it was polished with a fiberglass pen (and subsequently sonicated in acetone and IPA) in order to ensure good wire bonds. (b) Closeup of connection from SMP to chip. (c) Closeup of chip with individual wire bonds visible. (d) Bright field optical micrograph of paramp finger capacitors. (e) Bright field optical micrograph of paramp SQUID termination region. (f) Close-up bright field optical micrograph of paramp SQUIDs. There are a few small specks due to undeveloped resist near the SQUID loops, but they are away from the junctions. (g) Picture of experimental setup inside the dilution refrigerator; includes banana for scale.

had been observed in [15], and to prevent over-coupling to magnetic field via the flux focusing effect, whereby the effective magnetic field in the gap of the resonator could be two orders of magnitude larger than the applied magnetic field [7]. In the interest of time, an in-shield superconducting magnet was not obtainable, and for the first paramp tests we instead used an in-shield copper (non-superconducting) coil magnet, which turned out to provide insufficient magnetic flux through the SQUID loops (for our $12 \mu\text{m}^2$ loop area, a flux quantum corresponds to .17 millitesla at the SQUID) before significantly heating up the fridge, despite thermal anchoring of the flux bias line and of the magnet itself. In a second fridge cooldown, we used a superconducting magnet without a shield, demonstrating

much higher than its coupling quality factor, meaning in accordance with equation (2.38) essentially all of the information is contained in the reflected phase. As shown in Figure 4.14, the raw phase measured by the network analyzer has a large slope as a function of frequency simply due to the natural change in optical path length through the various coax cables as the frequency of propagation changes. Luckily, we can approximate the dispersion relation of our coax as linear and subtract off this large background, allowing us to observe a clear resonance at 7.26 GHz as expected with the zero applied magnetic flux through the SQUIDs (the predicted value of 7.2 GHz at maximum SQUID energy was surprisingly close). By fitting the phase response to theory, we can extract a quality factor of 198, meaning $2\gamma_1/(2\pi) \approx 37$ MHz. This is surprisingly close to the predicted value of 35 MHz at this operating frequency (remember, in accordance with equation (4.14), γ_1 depends on the resonance frequency in addition to the coupling capacitance).

4.2.1 Nonlinearity

To probe the Kerr nonlinearity of our resonator, we can crank up the probe power relative to the predicted critical input power. Figure 4.15 shows reflection spectroscopy measurements as a function of probe power and probe frequency. In the phase response, we see an increase in the slope of the phase jump, reaching and going through the critical point as described in the caption. In the amplitude response, for high powers we can start to see a small dip on resonance, presumably corresponding to the onset of a small nonlinear loss term. This term is presumed to be small because of the small dip it yields along with the fact that it was not needed to fit the functional form of the resonance frequency with respect to probe power. Namely, in both the phase and amplitude response, we can observe a small dip in the system's resonance frequency as a function of increasing probe power that agrees very well with the quadratic dependence of the resonance frequency on the input field discussed in Section 2.2.2, as shown by the fit to theory in the inset of Figure 4.15(b).

The probe powers shown in Figure 4.15 are based on a calibration of the coax lines (and a previous calibration of the lines in the fridge). From the onset of the critical point, we deduce a critical power of approximately -93.5 dBm, which is close to the predicted value [based on equations (3.49) and (2.47)] of -89 dBm. This is consistent with our uncertainty in the SQUID energy and in the performance of the circulator during the room-temperature calibration versus its performance while cold.

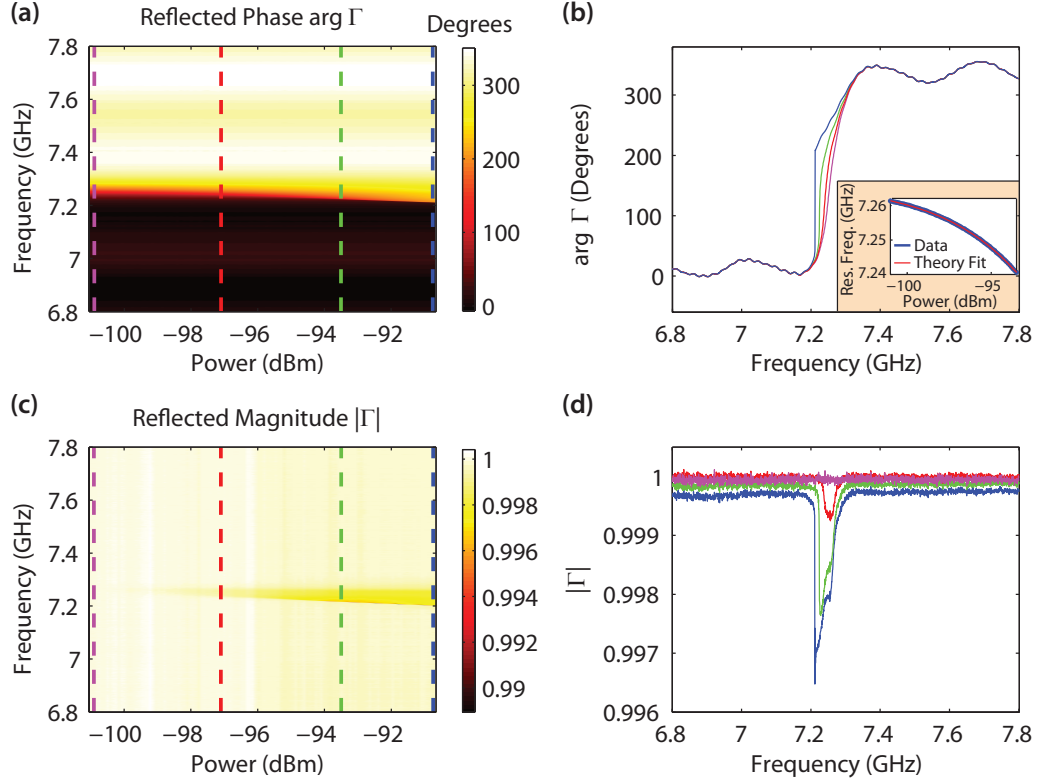


Figure 4.15 Reflection spectroscopy of the paramp with a single tone. (a) Reflected phase as a function of tone power (at the paramp) and frequency. (b) Vertical cuts of (a) with varying powers ranging from the linear regime (magenta) through the critical point (green) to the bistable regime (blue). Note that the resonance frequency decreases with power, as expected. The extracted resonance frequency along with a fit to theory is shown in an inset. (c) Magnitude of the reflection coefficient $|\Gamma|$, relative to the value in the linear regime (which was subtracted from each of the columns). Note the appearance of loss at high powers, suggesting a (small) amount of nonlinear loss. The fit of frequency to theory also suggests that the nonlinear loss is negligible. (d) Vertical cuts of (a) with various powers.

4.2.2 Parametric Gain

With the critical power known, we can now test the device's performance as a parametric amplifier. The setup for this measurement is also shown in 4.14, using two microwave signal generators combined at room temperature and a spectrum analyzer, rather than a network analyzer. For all measurements, the spectrum analyzer (an Agilent E4405B lent to us by the Houck lab) was operated with its minimum bandwidth resolution (i.e., a bin for power collection) of 1 KHz. Figure 4.16 shows the result of biasing the pump near its critical power and frequency, while also adding a much smaller test signal tone detuned 10 KHz above the pump. If all of the assumptions we made in Section 2.2 are satisfied, we could

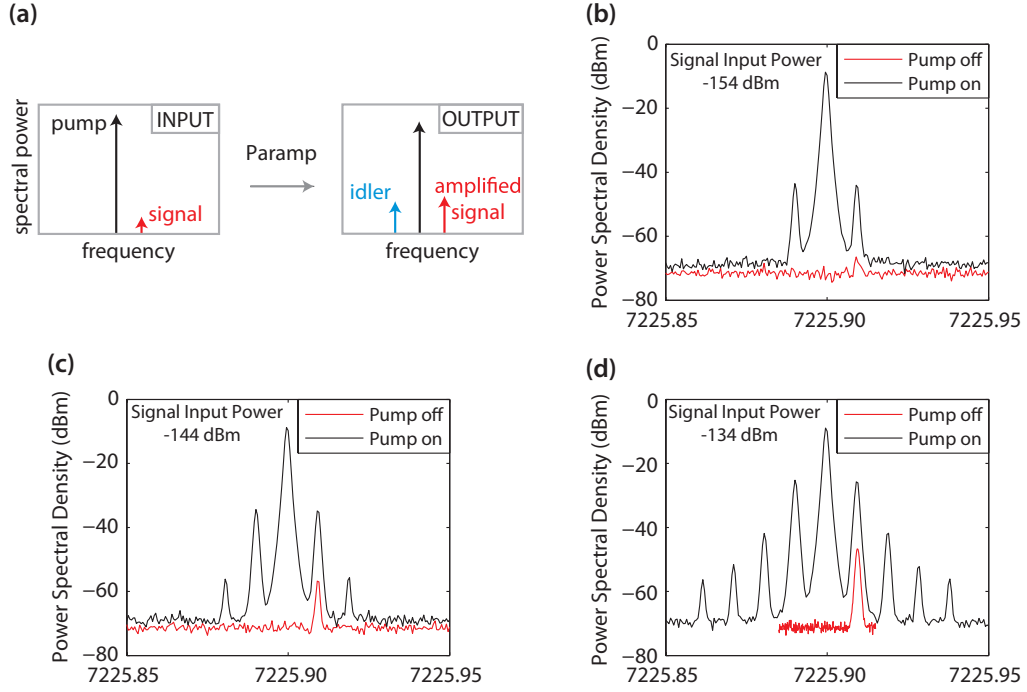


Figure 4.16 (a) Illustration of input and output spectrum for a non-degenerate paramp operated in the ideal linear regime. Figure adapted from [15]. (b) Observed spectral densities for a signal power 60 dB less than the pump power, with the paramp operating at a gain of about 20 dB. (c) Signal input 50 dB weaker than pump. (d) Signal input 40 dB less than pump.

expect to see amplification of the signal and the creation of an idler tone on the opposite side of the pump. This is precisely what is observed. For a signal tone approximately 60 dB below the pump critical power (and thus the pump) [Figure 4.16(b)], when the pump is off we observe a very small power spectral density just above the room-temperature noise floor corresponding to the small signal. When the pump is on, we observe a drastic increase in the signal power and also the appearance of an intermodulation tone on the other side of the pump as predicted by theory. However, if we increase the power of the signal relative to the pump as predicted by theory. However, if we increase the power of the signal relative to the pump [Figure 4.16(c) and (d)], other peaks in the spectrum appear. This is perhaps due to the violation of the stiff pump approximation, given that the signal is amplified by 20 dB, although the pump does not appear to be visibly depleted. Further experimental exploration of this phenomenon in addition to a theoretical understanding of the potential importance of terms beyond the linearized signal approximation are worth further pursuit⁸.

⁸A hand-wavey and perhaps incorrect intuition behind the appearance of these equally-spaced peaks is that the signal starts to act as a new pump for the original pump, causing a small amount of the original pump to appear as an idler relative to it and the signal, and so on with further

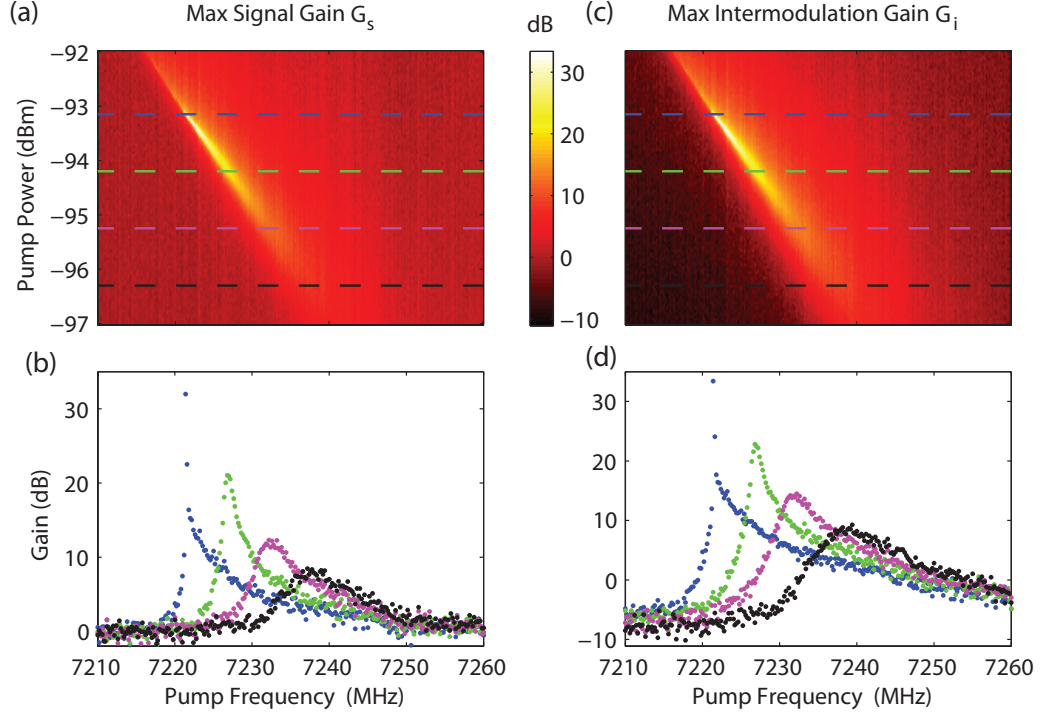


Figure 4.17 Maximum gains as a function of pump bias. (a) Maximum signal gain $G_s(10 \text{ KHz}) \approx G_s(0)$ as a function of pump power and pump frequency. Panels (a) and (c) share the same colorscale. (b) Cuts across the data in panel (a). (c) Maximum intermodulation gain $G_i(10 \text{ KHz}) \approx G_i(0)$ as a function of pump power and pump frequency. (d) Cuts across the data in panel (c).

To systematically test the system's performance as an amplifier, we can measure the maximum signal gain as a function of pump power and pump frequency. The results of such a measurement are shown in Figure 4.17. In this experiment, the signal is kept at a constant power 50 dB below the pump and at a detuning of 10 KHz from the pump frequency. Since this detuning is much less than γ_1 , measuring the signal gain will give a good approximation to the maximum gains $G_s(0)$ and $G_i(0)$. It is necessary to have some finite detuning $\omega \neq 0$, because otherwise we would be operating the amplifier in degenerate mode and would also need to worry about the relative phase of the signal and pump (this is explored in a later measurement). We see a maximum gain for a pump power of approximately -93.1 dBm, consistent with our (somewhat more ambiguous) spectroscopy measurements. We note that the intermodulation deamplification in Figure 4.17(d) would continue to decrease below -10 dB for low pump frequencies if it weren't for the noise floor becoming important harmonics. This could be related to classical intermodulation distortion [16].

at the spectrum analyzer.

After mapping out the pump bias landscape, we can explore the dependence of gain on signal frequency with a fixed pump; i.e., the bandwidth of the amplifier. We do this

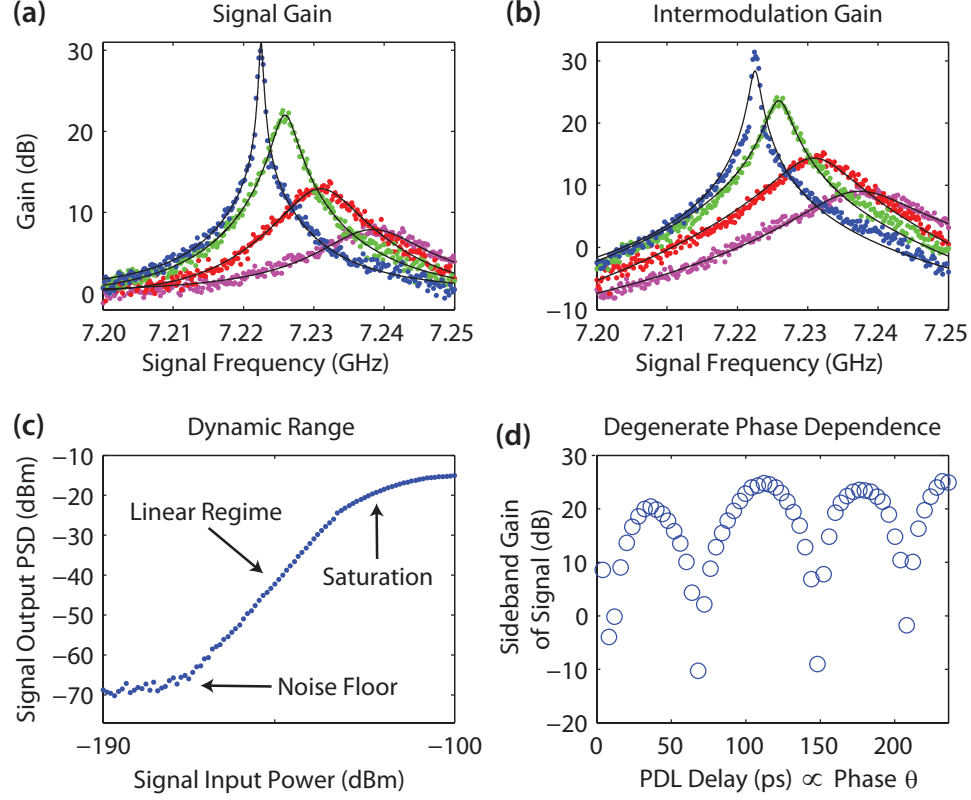


Figure 4.18 (a) and (b): Signal and intermodulation gains as a function of signal frequency, for four different pump biases (f_p, P_p): -96.3 dBm at 7237.8 MHz (magenta), -95 dBm at 7230.9 MHz (red), -94 dBm at 7225.9 MHz (green), and -93.4 dBm at 7222.5 MHz (blue). Equivalently, the ratios P_p/P_{crit} in increasing order are $\{.48, .65, .81, .94\}$. Each trace also shows a fit to theory (black curves). (c) Exploration of the dynamic range of the amplifier at a particular bias point [near the bias point of the green curves in (a) and (b)] such that the signal gain is 20 dB. (d) Phase-dependence of gain in degenerate mode (signal frequency the same as pump frequency, originating from the same microwave source).

by fixing the pump at one of the four points of maximum gain found at each of the four pump powers explored in Figure 4.17. Namely, the ratios P_p/P_{crit} in increasing order are $\{.48, .65, .81, .94\}$. The resulting gain curves, shown in Figure 4.18(a) and (b), are symmetric about the pump as expected, and fit to theory (black curves) quite well. We can clearly see that the bandwidth of the amplifier decreases with the maximum gain. From the fitted curves, we extract signal gain-bandwidth products of $\frac{\sqrt{3}}{4} \sqrt{G(0)} B_\omega / (2\pi) \approx \{19, 20, 22, 8\}$ MHz. The first three of these products agree surprisingly well with our high-gain prediction

(2.70), which says this should simply equal $\gamma_1/(2\pi) \approx 18.5$ MHz. The discrepancy for the highest gain could possibly be due to the onset of pump depletion. Either way, we have attained our designed performance of 2 MHz of bandwidth at 25 dB gain.

Figure 4.18(c) shows the power spectral density (at the spectrum analyzer) of the amplified signal as a function of input signal power, with the paramp operated with a gain of 20 dB. We see that the paramp performs well as a linear amplifier for circuit QED experiments, having a linear-regime dynamic range of at least 30 dB (the noise floor limits the probing of signals below the lower limit of this range). This range is limited by saturation of the amplifier at high signal input powers due to the onset of pump depletion (in the plot shown, this corresponds to the input signal being about 30 dB less than the pump [and then amplified by 20 dB to 10 dB less than the pump]).

Regarding the noise floor at the spectrum analyzer, it was usually found to be -73 to -70 dBm (although on the first day of measurements it was only -80 dBm for unknown reasons). This drops to -95 dBm when the output of the room temperature amplifiers is disconnected from the spectrum analyzer. If we instead leave the analyzer connected to the output of the room temperature amplifiers and instead unplug the input to the first room temperature amplifier, the noise floor is still -89 dBm. To extend paramp measurements to be able to observe lower deamplifications, one could try and bypass the room temperature amplifiers altogether. But with the paramp operated at 25 dB gain, we can then see the amplified signal on the analyzer but not the bare signal without the pump turned on. This means that the signal itself must have been below the noise floor.

Finally, we test our prediction for phase-dependent gain when the paramp is operated in degenerate mode. To do this, we operate the pump near the same bias point (19 dBm gain), but provide the signal through the same source as the pump via a splitter. The phase of the pump relative to the signal is then changed by routing the pump path through a Colby PDL-10A programmable delay line, which can provide delays (i.e., path length differences) for microwaves. Because the “signal” and “pump” are at the same frequency, in single-frequency degenerate mode we must define the signal gain as the gain in sideband modulation power when the signal is amplitude-modulated at a certain frequency. Namely, we amplitude-modulate the signal path at 20 KHz via a Marki mixer, and measure the sideband power spectral density with the pump on and off. The degenerate gain is then defined by these two relative powers. Figure 4.18(d) shows the results of this experiment. We can clearly see a strong periodic dependence on the PDL delay, which is ideally proportional to the path length difference (and hence phase difference) of the pump relative to the signal. However, there are some imperfections due to the imperfect nature of the delay line and the fact that changing the delay also sometimes slightly changes the pump power. It is quite interesting

to note that the maximum gain is greater than the nominal $G(10 \text{ KHz}) \approx G(0) = 19 \text{ dB}$, and reaches up to 25 dB. This is just as predicted by the quadrature squeezing relations (2.95). The de-amplified quadrature should have a correspondingly lower gain, but we are unable to observe the full dip due to both the finite resolution of the delay line and also the noise floor at the spectrum analyzer.

In a second fridge cooldown, we removed the magnetic shield from the sample and instead used a larger external superconducting magnet below the base plate of the fridge. This allowed us to thread enough flux through the SQUIDs without heating the fridge, so that we could observe the frequency-tunability of the paramp. The results of this experiment are shown in Figure 4.19. The resonance frequency as a function of applied magnetic field

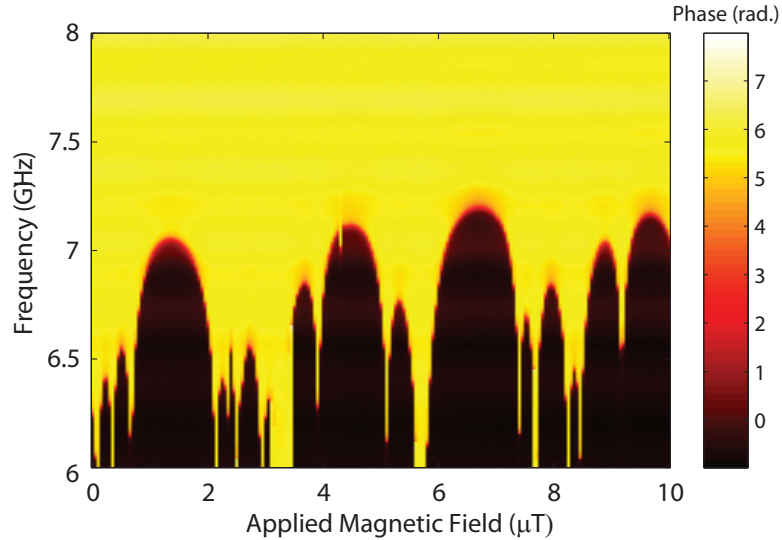


Figure 4.19 Reflected phase of a single tone in the linear regime, as a function of applied magnetic field. The quasi-periodic resonance indicates clear tunability of ω_0 .

is not strictly periodic [as would be predicted for a single SQUID by equation (3.20)], because there are in fact four SQUIDs that are not exactly identical. The quasi-periodic pattern is therefore to be expected. We note that, based on a previous calibration of the superconducting magnet, the applied magnetic field needed to tune through a period is roughly 50 times less than what would be expected without considering the flux focusing effect. This means that our attempts to reduce flux focusing by carving out the Nb ground plane near the SQUIDs had at most a factor of ~ 2 . Note that the zero-field value here leads to a different resonance frequency than the previous cooldown with the magnetic shield and no applied field. This is because during the second cooldown, magnetic flux was trapped in the superconductor due to lack of shielding, leading to a flux offset. The

maximum resonance frequency observed agrees with what we designed, and the desired operating point of 6.85 GHz is at a point with a good tradeoff between tunability and stability. We note that because there was no internal magnetic shield at the sample during the cooldown, the resonance frequencies drifted slightly, due to either external or internal (i.e., superconducting vortices from trapped flux) magnetic noise. Namely, for a resonance frequency of 7.1 GHz, the resonance drifted by about 5 MHz on the timescale of a minute, whereas at 6.2 GHz, the resonance drifted by about 100 MHz on this same timescale. It will therefore be necessary to implement an in-shield superconducting magnet to obtain a tunable paramp that is also stable.

4.3 Future Directions

This thesis has performed a theoretical analysis of parametric amplification and has presented preliminary data demonstrating the successful implementation of a paramp for circuit QED based on a superconducting resonator inheriting a Kerr nonlinearity from an array of SQUIDs. The paramp characterization measurements performed in section 4.2 were only started shortly before the completion of this thesis, so there are still further measurements that would be worth pursuing, including a more detailed analysis of the data shown and a verification that the second paramp device also works. It would also be desirable to see how quantum-limited the added noise of the amplifier is. The added noise could be probed for example through a so-called Y-factor measurement in which two calibrated noise sources are input to the paramp [16, 42]. Implementing a superconducting magnet (or perhaps an on-chip flux bias line) within the magnetic shield is the next design step if we wish to have a tunable and stable amplifier to use in actual circuit QED experiments. The most elegant and relatively localized solution would probably be modifying an octobox by shaving an indent around its circumference, allowing many layers of thin superconducting wire to be wrapped around it. Demonstrating that the paramp can be used to read out a superconducting qubit with a decreased number of averages would then be a proof-of-principle demonstration of paramp-based readout. A simple and effective readout scheme to use was recently demonstrated by Ristè *et al.*, whereby a small dispersive readout signal leads to a large change in the phase of the reflected pump when the paramp is operated in single-tone degenerate mode near its sensitive critical point [69].

After achieving readout of a superconducting transmon qubit with the paramp (as was done in [69]), we would like to develop paramps to be used in novel experiments involving quantum dots. Other spin qubit projects in our lab would also benefit from such a Josephson parametric amplifier; this will require lower ranges of operating frequencies (on the order

of 1 GHz) and would be an interesting engineering challenge (although presumably not as challenging as conversely going to higher frequencies). Realistic progress towards useful paramps in our lab is now in the foreseeable future.

Appendix A

Quantization of the Electromagnetic Field in a Perfectly Conducting Cavity

We briefly perform a variant of a standard method of field quantization based on Maxwell's equations (see for example [39]) that is accessible to someone with an understanding of undergraduate quantum mechanics and electromagnetism. In the main text we will give a rather different and specific treatment of cavity quantization by analyzing the modes of the particular type of resonator used in making a cQED paramp. However, the derivation in this section is quite general and will help us to understand where the Jaynes-Cummings Hamiltonian comes from in the next section. We start by examining the electromagnetic vector potential satisfying

$$\mathbf{B}(\mathbf{r}, t) = \nabla \times \mathbf{A}(\mathbf{r}, t) \tag{A.1a}$$

$$\mathbf{E}(\mathbf{r}, t) = -\frac{\partial \mathbf{A}(\mathbf{r}, t)}{\partial t} - \nabla \phi(\mathbf{r}, t), \tag{A.1b}$$

where ϕ is the scalar potential. As studied in an undergraduate course in electromagnetism [70], choosing the Coulomb gauge

$$\nabla \cdot \mathbf{A} = 0, \tag{A.2a}$$

$$\nabla^2 \phi = -\frac{\rho}{\epsilon_0} \tag{A.2b}$$

and combining with Maxwell's equations yields that the vector potential in vacuum obeys the wave equation

$$\nabla^2 \mathbf{A}(\mathbf{r}, t) = \frac{1}{c^2} \frac{\partial^2 \mathbf{A}(\mathbf{r}, t)}{\partial t^2}. \quad (\text{A.3})$$

The theory of harmonic analysis tells us that it is possible to express any solution of (A.3) as a linear combination of solutions of the form $\mathbf{A}(\mathbf{r}, t) = \mathbf{u}(\mathbf{r})T(t)$. Substituting such a separated solution into (A.3) yields for each Cartesian component of $\mathbf{u}(\mathbf{r})$

$$\frac{\nabla^2 u^{(i)}(\mathbf{r})}{u^{(i)}(\mathbf{r})} = \frac{\ddot{T}(t)}{c^2 T(t)}. \quad (\text{A.4})$$

Since the left-hand side depends only on \mathbf{r} and the right-hand side only on t , each side must be equal to a mutual constant. For an approximately non-leaky cavity, we expect that this constant should be a negative real number, say $-k^2$. Defining $\omega_k = c|k|$, this implies that $T_k(t) = e^{\pm i\omega_k t}$ and that

$$\left(\nabla^2 + \frac{\omega_k^2}{c^2} \right) \mathbf{u}_k(\mathbf{r}) = 0. \quad (\text{A.5})$$

For a field confined to well-defined cavity of finite volume V , the spectrum ω_k will be infinite but discrete, and the expression for \mathbf{A} takes the form of a unique discrete sum over a complete set of orthonormal modes. The Coulomb gauge condition (A.2a) takes away a degree of freedom, so that we expect the spatial vector eigenfunctions of (A.5) to have two independent orthogonal mode polarizations, indexed by $\mu = 1, 2$. We define these functions to be unitless and normalized so that

$$\frac{1}{V} \int_V \mathbf{u}_{k,\mu}^*(\mathbf{r}) \cdot \mathbf{u}_{k',\mu'}(\mathbf{r}) d\mathbf{r} = \delta_{kk'} \delta_{\mu\mu'}. \quad (\text{A.6})$$

The exact nature of these functions depends on the nature of the cavity boundary. For example, in a rectangular box with perfectly conducting walls, they take the familiar Fourier form $\hat{\mathbf{e}}_{k,\mu} e^{i\mathbf{k} \cdot \mathbf{r}}$, where $\hat{\mathbf{e}}_{k,\mu}$ is a unit polarization vector [necessarily perpendicular to the wavevector \mathbf{k} by (A.2a)]. More generally, (A.2a) dictates that

$$\nabla \cdot \mathbf{u}_{k,\mu}(\mathbf{r}) = 0. \quad (\text{A.7})$$

From now on, we will suppress the double index on $\mathbf{u}_{k,\mu}$ in favor of the more compact notation \mathbf{u}_m (m stands for a single mode). An arbitrary real solution for $\mathbf{A}(\mathbf{r}, t)$ can now be expressed as

$$\mathbf{A}(\mathbf{r}, t) = \sum_m [a_m(t) \mathbf{u}_m(\mathbf{r}) + a_m^*(t) \mathbf{u}_m^*(\mathbf{r})], \quad (\text{A.8})$$

where the a_m are complex mode amplitudes with time dependence absorbed into them and with SI units of $\text{V}\cdot\text{s}\cdot\text{m}^{-1}$. Substituting (A.8) into (A.1) yields

$$\begin{aligned}\mathbf{E}(\mathbf{r}, t) &= \sum_m i\omega_m [a_m(t)\mathbf{u}_m(\mathbf{r}) - a_m^*(t)\mathbf{u}_m^*(\mathbf{r})] \\ \mathbf{B}(\mathbf{r}, t) &= \sum_m [a_m(t)\nabla \times \mathbf{u}_m(\mathbf{r}) + a_m^*(t)\nabla \times \mathbf{u}_m^*(\mathbf{r})]\end{aligned}\quad (\text{A.9})$$

The classical field Hamiltonian is the electromagnetic energy

$$\mathcal{H} = \frac{\epsilon_0}{2} \int_V (\mathbf{E}^2 + c^2 \mathbf{B}^2) d\mathbf{r} = V\epsilon_0 \sum_m \omega_m^2 (a_m^* a_m + a_m a_m^*), \quad (\text{A.10})$$

where we have used (A.6) and (A.7), and in anticipation have withheld from simplifying the expression using the usual commutative property of complex multiplication¹. We can notice a similarity between the form of (A.10) and an infinite set of uncoupled harmonic oscillators of the kind studied in elementary quantum mechanics [50]. We postulate that the creation and annihilation operators should be defined by the promotion

$$a_m(t) \rightarrow \sqrt{\frac{\hbar}{2\omega_m V \epsilon_0}} \hat{a}_m, \quad a_m^*(t) \rightarrow \sqrt{\frac{\hbar}{2\omega_m V \epsilon_0}} \hat{a}_m^\dagger \quad (\text{A.11})$$

and obey the canonical bosonic commutation relation

$$[\hat{a}_m, \hat{a}_{m'}^\dagger] = \delta_{mm'}. \quad (\text{A.12})$$

The coefficients in (A.11) are chosen so that using (A.12), the quantum version of (A.10) can be written in the standard form

$$\hat{H}_{\text{cavity}} = \sum_m \hbar\omega_m \left(\hat{a}_m^\dagger \hat{a}_m + \frac{1}{2} \right). \quad (\text{A.13})$$

Each harmonic oscillator excitation corresponds to a photon, and as usual $\langle \hat{a}_m^\dagger \hat{a}_m \rangle$ is the expected number of photons of a given mode occupying the resonator. The energy eigenstates are the number states (also known as Fock states) with a definite number of excitations n_m

¹More specifically, for the magnetic part we have used the expansion $(\nabla \times \mathbf{u}^*) \cdot (\nabla \times \mathbf{u}) = \nabla \cdot [\mathbf{u}^* \times (\nabla \times \mathbf{u})] + \mathbf{u}^* \cdot [\nabla \times (\nabla \times \mathbf{u})]$ and then Stokes' theorem to convert the integral of the former term into a boundary term that vanishes for a perfectly conducting cavity wall at which $\mathbf{u} \times d\mathbf{S} = 0$. The integral of the latter term becomes $\int_V \mathbf{u}^* \cdot [\nabla \times (\nabla \times \mathbf{u})] d\mathbf{r} = (\text{using (A.7)}) \int_V \mathbf{u}^* \cdot (-\nabla^2 \mathbf{u}) = (\text{using (A.5) and (A.6)}) \omega_m^2 / c^2$.

in each mode, leading to energies

$$E = \sum_m \hbar \omega_m (n_m + 1/2). \quad (\text{A.14})$$

Appendix B

The Jaynes-Cummings Hamiltonian

B.1 Derivation

The problem we now want to address is this: how does a single atom interact with photons in a resonator? Under the approximations we are about to make, there turns out to be a rather simple Hamiltonian describing the evolution of the joint atom-cavity system.

Any atom is a many-electron system bound by an effective atomic potential $V_{\text{atm}}(\mathbf{r})$. The electronic wavefunction of an isolated atom will have a countable number of bound energy eigenstates $|j\rangle$ with energy E_j forming a complete orthonormal basis of its Hilbert space, so that the Hamiltonian takes the form $\sum_j E_j |j\rangle\langle j|$. If we truncate the atom's energy levels to the lowest two in order to obtain a two-level system (valid when the spectrum is anharmonic enough that the desired transition can be isolated), we obtain, after shifting the zero of energy to the average energy, the simple atomic Hamiltonian

$$\hat{H}_{\text{atm}} = \frac{1}{2}\hbar\omega_a \begin{pmatrix} 1 & 0 \\ 0 & -1 \end{pmatrix} = \frac{1}{2}\hbar\omega_a \sigma_z \quad (\text{B.1})$$

in the $\{|1\rangle, |0\rangle\}$ basis, where $\hbar\omega_a$ is the energy difference between the two energy eigenstates. We now have the atomic Hamiltonian and the cavity Hamiltonian (A.13), and would like a term \hat{H}_{int} describing atom-photon interactions.

The classical minimal coupling Hamiltonian describing the interaction of an electron

with the electromagnetic field is [61]

$$\mathcal{H}_{\text{EM}} = \frac{1}{2m_e} (\mathbf{p} + e\mathbf{A}(\mathbf{r}, t))^2 - e\phi(\mathbf{r}, t), \quad (\text{B.2})$$

where $-e$ is the electron charge and \mathbf{A} is the vector potential. It is easily verified that Hamilton's equations of motion with \mathcal{H}_{EM} yield the correct classical Lorentz force expressions. We now use the semi-classical version of (B.2), under which the electron is treated quantum-mechanically (neglecting spin) but the electromagnetic field is not, to write down the Hamiltonian for an atomic electron

$$\hat{H}_{\text{el}} = \left[-\frac{\hbar^2}{2m_e} \left(\nabla - \frac{ie}{\hbar} \mathbf{A}(\mathbf{r}, t) \right)^2 - e\phi(\mathbf{r}, t) + V_{\text{atm}}(\mathbf{r}) \right] \psi(\mathbf{r}, t) \quad (\text{B.3})$$

(the electric field due to the atom is contained in V_{atm}). We know from classical electromagnetism [or infer from (A.1)] that the electric and magnetic fields are invariant quantities under the gauge transformation

$$\begin{aligned} \mathbf{A} &\rightarrow \mathbf{A}' = \mathbf{A} + \nabla\Lambda \\ \phi &\rightarrow \phi' = \phi - \frac{\partial\Lambda}{\partial t} \end{aligned} \quad (\text{B.4})$$

for some scalar Λ . However, it is not obvious that such a transformation is consistent with Schrödinger's equation. Directly applying such a transformation yields a very different looking time evolution, but we can try to restore the original form by performing a local phase transformation on the position space wave function of the form

$$\psi(\mathbf{r}, t) \rightarrow \psi'(\mathbf{r}, t) = e^{i\chi(\mathbf{r}, t)} \psi(\mathbf{r}, t). \quad (\text{B.5})$$

Plugging this into (B.3) shows us that the Schrödinger equation retains its form provided we choose $\chi(\mathbf{r}, t) = \frac{e}{\hbar} \Lambda(\mathbf{r}, t)$. Observables will also remain unchanged provided we transform a given Hermitian operator A to UAU^\dagger , with $U = e^{i\chi(\mathbf{r}, t)}$.

With the semi-classical picture in hand, we choose again to start in the Coulomb gauge (A.2). We consider the interaction with photons in vacuum with no charge density in the vicinity other than that due to the atom, so we may take the instantaneous potential $\phi(\mathbf{r}, t)$ due to outside sources to be 0 as we did in our field quantization. The Schrödinger equation becomes

$$i\hbar \frac{\partial \psi(\mathbf{r}, t)}{\partial t} = \left[-\frac{\hbar^2}{2m_e} \left(\nabla - \frac{ie}{\hbar} \mathbf{A}(\mathbf{r}_0, t) \right)^2 + V_{\text{atm}}(\mathbf{r}) \right] \psi(\mathbf{r}, t), \quad (\text{B.6})$$

where we have made the *dipole approximation* [38] $\mathbf{A}(\mathbf{r}, t) \approx \mathbf{A}(\mathbf{r}_0, t)$, where \mathbf{r}_0 is the center

of the atom. This approximation is valid if the wavelength of the mode is large compared with the linear size of the bulk of the atomic wavefunction. Note that we can eliminate the $\mathbf{A}(\mathbf{r}_0, t)$ term in (B.6) by making the gauge transformation (B.4) with $\Lambda = -\mathbf{A}(\mathbf{r}_0, t) \cdot \mathbf{r}$, along with the required phase transformation

$$\psi(\mathbf{r}, t) \rightarrow \psi'(\mathbf{r}, t) = e^{-\frac{ie}{\hbar} \mathbf{A}(\mathbf{r}_0, t) \cdot \mathbf{r}} \psi(\mathbf{r}, t). \quad (\text{B.7})$$

Substituting these transformations into (B.6) yields, after rearrangement,

$$i\hbar \frac{\partial \psi'(\mathbf{r}, t)}{\partial t} = \left[-\frac{\hbar^2}{2m} \nabla^2 + V_{\text{atm}}(\mathbf{r}) - e\mathbf{r} \cdot \mathbf{E}(\mathbf{r}_0, t) \right] \psi'(\mathbf{r}, t), \quad (\text{B.8})$$

where we have used (A.1a) for the electric field. Summing over all of the atomic electrons (indexed by a), we arrive at the semi-classical interaction Hamiltonian in this gauge,

$$\hat{H}_{\text{int}} = -e \sum_a \mathbf{r}_a \cdot \mathbf{E}(\mathbf{r}_0, t). \quad (\text{B.9})$$

We can rewrite $e \sum_a \mathbf{r}_a$ as $= \sum_{i,j} e|i\rangle\langle i| \sum_a \mathbf{r}_a |j\rangle\langle j| \equiv \sum_{i,j} \mathbf{d}_{ij} |i\rangle\langle j| \equiv \sum_{i,j} \mathbf{d}_{ij} \sigma_{ij}$, where $\mathbf{d}_{ij} = e\langle i| \sum_a \mathbf{r}_a |j\rangle = \sum_a \iiint \Psi_i^*(\mathbf{r}_a) e\mathbf{r}_a \Psi_j(\mathbf{r}_a) d^3\mathbf{r}_a$ is the transition dipole moment. Using (A.9) and (A.11), we obtain after shifting each \hat{a}_m by an appropriate phase factor (this is just a convention and leaves the cavity Hamiltonian (A.13) unchanged) the electric field operator

$$\hat{\mathbf{E}} = \sum_m \sqrt{\frac{\hbar\omega_m}{2V\epsilon_0}} \mathbf{u}_m(\mathbf{r}_0) (\hat{a}_m^\dagger + \hat{a}_m). \quad (\text{B.10})$$

Combining these results, we therefore expect a fully quantized (non-relativistic) atom-photon interaction Hamiltonian of

$$\hat{H}_{\text{int}} = \hbar \sum_{i,j} \sum_m g_{ij,m} \sigma_{ij} \otimes (\hat{a}_m^\dagger + \hat{a}_m), \quad (\text{B.11})$$

where $g_{ij,m} = -\mathbf{d}_{ij} \cdot \mathbf{u}_m \sqrt{\frac{\hbar\omega_m}{2V\epsilon_0}}$ are dipole coupling factors. On timescales small compared to the transit time T_{transit} of the atom through the cavity, we can treat the position-dependent coupling factors as constants. This is not always valid in CQED, but is true for the stationary artificial atoms of cQED.

In general, the coupling strengths increase as the volume decreases, as could be seen directly for a rectangular box cavity by plugging in the aforementioned Fourier form of \mathbf{u}_m . More intuitively, this is due to the fact that at a given photon frequency, a smaller volume leads to a higher energy density because the total energy contained in the cavity

must take on the same quantized value. Circuit QED is usually concerned with systems in the *strong coupling regime* for which $g \gg \kappa, \gamma_\perp$. For simplicity, we take \mathbf{d}_{ij} to be real, so that $g_{ij,m} = g_{ji,m} \equiv g_m$ when there are only two atomic levels. Thus, for a two-level atom (qubit), we have

$$\hat{H}_{\text{int}} = \hbar \sum_m g_m (\sigma_+ + \sigma_-)(\hat{a}_m^\dagger + \hat{a}_m), \quad (\text{B.12})$$

where we have defined the atomic raising and lowering operators $\sigma_+ = |1\rangle\langle 0|$ and $\sigma_- = |0\rangle\langle 1|$ and dropped the explicit tensor product symbol. If electromagnetic signals are sent with frequencies and polarizations intended to excite only one photon mode, say one of the lowest ones of frequency ω_r , we only need to consider one mode in the sum (B.12). In the microwave cavities of cQED, the one-mode approximation is certainly possible for low electronic noise and cryogenic temperatures: at $T = 20$ mK and $\omega_r = 2\pi \times 7$ GHz, the Bose-Einstein distribution yields a thermal population of

$$\bar{n}_r = \frac{2}{e^{\hbar\omega_r/kT} - 1} \approx 10^{-8} \quad (\text{B.13})$$

for the lowest mode and even smaller numbers for higher modes. Thus we may take $m = 1$ and drop all other terms (along with the subscript). Finally, we make the *rotating wave approximation* [38], which keeps only the terms proportional to $\sigma_+\hat{a}$ and $\sigma_-\hat{a}^\dagger$ that conserve excitation number (and also energy, when the atom transition frequency matches that of the photon). For example, $\sigma_+\hat{a}$ represents the excitation of the atom with an annihilation of a photon. The name given to this approximation stems from the fact that in the interaction picture $H_I = e^{iH_{\text{cavity}}t/\hbar} H_d e^{-iH_{\text{cavity}}t/\hbar}$, the non-energy-conserving terms oscillate rapidly and average out to zero. Combining our interaction Hamiltonian with the atom and cavity Hamiltonians, we arrive at the well-known Jaynes-Cummings Hamiltonian of quantum optics for an atom interacting with a single mode of the electromagnetic field:

$$H_{\text{JC}} = \hbar\omega_r \left(a^\dagger a + \frac{1}{2} \right) + \frac{1}{2} \hbar\omega_a \sigma_z + \hbar g (\sigma_+ a + \sigma_- a^\dagger), \quad (\text{B.14})$$

where we have dropped the hats on operators and the identity operator is implied for the photon field in the purely atomic term and vice versa. We have arrived at this result using many approximations, but its predictions, some of which we will now explore, have been extremely well-verified by many CQED and cQED experiments.

B.2 Coupling Phenomena

Analytic Eigenstates and Eigenenergies

We now discuss the eigenstates and eigenenergies of the coupled atom-cavity system under the Jaynes-Cummings Hamiltonian. Still treating our atom as a two-level system, we will use the basis states $|g\rangle|n\rangle = |g, n\rangle$ and $|e\rangle|n\rangle = |e, n\rangle$, which denote atom in the ground and excited state (respectively) with n photons in the cavity. We should suspect that these basis states will no longer be eigenstates of the whole Hamiltonian due to the interaction term. We can easily solve for the eigenstates by first writing the Jaynes-Cummings Hamiltonian in matrix form. Since H_{JC} only couples neighboring atom and photon levels (i.e, swaps excitations between $|g\rangle|n\rangle$ and $|e\rangle|n-1\rangle$), the matrix takes a block diagonal form. Defining the detuning $\Delta = \omega_a - \omega_r$ and plugging into H_{JC} (we suppress the hats on Hamiltonians from now on), we see that the n^{th} block ($n \geq 1$) is

$$H^{(n)} = \hbar \begin{pmatrix} n\omega_r - \frac{\Delta}{2} & g\sqrt{n} \\ g\sqrt{n} & n\omega_r + \frac{\Delta}{2} \end{pmatrix} \quad (\text{B.15})$$

in the n -excitation subspace basis $\{|g\rangle|n\rangle, |e\rangle|n-1\rangle\}$. We can diagonalize the entire Hamiltonian by diagonalizing each of the two-dimensional $H^{(n)}$. This simple calculation yields eigenenergies

$$E_{\pm, n} = n\hbar\omega_r \pm \frac{\hbar}{2} \sqrt{4g^2n + \Delta^2}. \quad (\text{B.16})$$

For $n = 0$, we have the ground state energy of $-\frac{\hbar\Delta}{2}$ corresponding to the zero excitation eigenstate $|g\rangle|0\rangle$ (which wasn't formally included in our blocks). Since these are two-dimensional subspaces, we may find an angle θ_n such that the orthonormal eigenstates are

$$\begin{aligned} |+, n\rangle &= \sin \theta_n |g\rangle|n\rangle + \cos \theta_n |e\rangle|n-1\rangle \\ |-, n\rangle &= \cos \theta_n |g\rangle|n\rangle - \sin \theta_n |e\rangle|n-1\rangle. \end{aligned} \quad (\text{B.17})$$

To find the form of θ_n , note that we require $H^{(n)}|+, n\rangle = E_{+, n}|+, n\rangle$. Equating the components of $|g\rangle|n\rangle$ then yields

$$\tan \theta_n = \frac{2g\sqrt{n}}{\Delta + \sqrt{4g^2n + \Delta^2}} \rightarrow \theta_n = \frac{1}{2} \arctan \frac{2g\sqrt{n}}{\Delta}, \quad (\text{B.18})$$

where we have used the identity $\tan 2\theta = \frac{2 \tan \theta}{1 - \tan^2 \theta}$.

The Resonant Regime

At zero detuning (the so-called resonant regime), the eigenstates are equal superpositions of atom and photon states,

$$|\psi_{\pm}\rangle = (|g\rangle|n\rangle \pm |e\rangle|n-1\rangle)/\sqrt{2} \quad (\text{B.19})$$

Looking at (B.16), in this regime the once degenerate subspace of $|g\rangle|n\rangle$ and $|e\rangle|n-1\rangle$ is split into two energies differing by $2\hbar g\sqrt{n}$, a phenomenon known as *vacuum Rabi splitting*. Spectroscopically measuring the lowest such splitting is a common way of experimentally obtaining the value of the coupling strength g . We can also now predict the fundamental

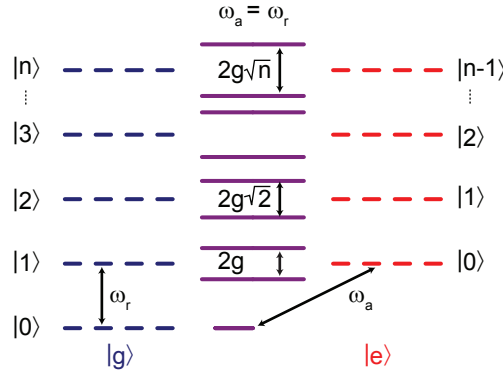


Figure B.1 Jaynes-Cummings energy level diagram (in angular frequencies) in the resonant regime $\Delta = 0$, where we observe vacuum Rabi splitting (uncoupled degenerate blue and red lines become split purple lines). $|n\rangle$ refers to photon number and $|g\rangle$ and $|e\rangle$ correspond to the atom in the ground or excited state. Figure adapted from [7].

CQED phenomenon of vacuum Rabi oscillations. This is obvious at zero detuning from the nature of our eigenstates; starting in $\psi(0) = |e, 0\rangle$, the state will oscillate to and from $|g, 1\rangle$, since these states are the standard $|+\rangle$ and $|-\rangle$ states on the Bloch sphere. More generally at any detuning, if we start in the state $|e\rangle|n-1\rangle$, the standard time evolution of the separated Schrödinger equation applied to the n -excitation subspace yields (after using (B.17) to express $|e\rangle|n-1\rangle$ in terms of the eigenstates $|-, n\rangle$ and $|+, n\rangle$)

$$\psi(t) = \cos \theta_n e^{-iE_{+,n}/\hbar} |+, n\rangle - \sin \theta_n e^{-iE_{-,n}/\hbar} |-, n\rangle. \quad (\text{B.20})$$

Plugging in the eigenenergies (B.16) and taking the squared magnitude of the $|g, n\rangle$ component yields the probability $P_g(t)$ of the excitation having transferred to a cavity photon:

$$P_g(t) = |\cos \theta_n \sin \theta_n e^{-i\Omega t} - \sin \theta_n \cos \theta_n e^{i\Omega t}|^2, \quad (\text{B.21})$$

where $\Omega \equiv \sqrt{g^2 n + (\frac{\Delta}{2})^2}$. Using the trigonometric identities $\cos \theta \sin \theta = \frac{1}{2} \sin 2\theta$ and $\sin \arctan x = \frac{x}{\sqrt{1+x^2}}$, we obtain the expression

$$P_g(t) = \frac{g^2 n}{g^2 n + \Delta^2} \sin^2 \Omega t. \quad (\text{B.22})$$

Thus, the excitation is swapped between atom and cavity at the *vacuum Rabi frequency* 2Ω . It is also interesting to note that the coefficient in front of the oscillation term is a Lorentzian as a function of the detuning, which is a very special instance of commonly measured Lorentzian absorption spectra. Unlike spontaneous emission into a continuum of vacuum modes (which is essentially the result of the destructive interference of many modes), this is a coherent, reversible phenomenon that occurs when the atom interacts with a single quantized mode of the electromagnetic field in a well-defined cavity. As such, it has no obvious classical counterpart. When measuring the vacuum Rabi splitting, the finite lifetimes of the excitations due to decoherence manifest themselves as a finite width in these energy levels in accordance with the energy-time uncertainty principle. Since in the resonant regime excitations are half atomic excitations and half photons, we might guess that the decay rate of these states should be $\Gamma \approx \frac{\gamma_{\perp} + \kappa}{2}$. If we are in the strong coupling regime, the splitting is well-defined and has sharp peaks, with many vacuum Rabi oscillations occurring before the decay of the excitation.

The Dispersive Regime

A now paradigmatic way of utilizing cQED for quantum computation is to operate in the *dispersive regime*, where the detuning is large compared to g (but not so incredibly large that our rotating wave approximation breaks down) so that photons are not absorbed by the atom. This regime provides us with a means of state readout (D5) by providing an effective qubit state-dependent shift in the cavity resonance frequency, which can be detected by probing the cavity with microwaves, and also provides a way to couple distant qubits via the cavity. In this regime, H_{int} will be weak, as even the terms $\sigma_+ \hat{a}$ and $\sigma_- \hat{a}^\dagger$ don't conserve energy. Rather than simply Taylor expanding (B.16) and (B.17), it will be useful to find a unitary change of basis U such that the transformed Hamiltonian $H'_{\text{JC}} = U H_{\text{JC}} U^\dagger$ eliminates the coupling term to first order. We will now motivate the transformation commonly stated in the cQED literature [8]. We know that in this regime $g/\Delta \ll 1$, so that if we express $U = e^{\frac{g}{\Delta} X}$, where X is antihermitian, we can write $H'_{\text{JC}} = e^{\frac{g}{\Delta} X} H_{\text{JC}} e^{-\frac{g}{\Delta} X}$ and Taylor expand for small g/Δ (recognizing and factoring out a commutator each time we take a derivative)

so that

$$H'_{\text{JC}} = H_{\text{JC}} + \frac{g}{\Delta}[X, H_{\text{JC}}] + \frac{1}{2!} \left(\frac{g}{\Delta} \right)^2 [X, [X, H_{\text{JC}}]] + \dots \quad (\text{B.23})$$

We want the second term to eliminate H_{int} from the first term. Since H_{int} is first order in g , we thus require an X which is zeroth order in g and satisfies $\frac{g}{\Delta}[X, H_{\text{cavity}} + H_{\text{atm}}] = -H_{\text{int}}$. Dividing through by $\frac{\hbar g}{\Delta}$ yields

$$\omega_r[X, \hat{a}^\dagger \hat{a}] + \frac{1}{2}\omega_a[X, \sigma_z] = \omega_r(\sigma_+ \hat{a} + \sigma_- \hat{a}^\dagger) - \omega_a(\sigma_+ \hat{a} + \sigma_- \hat{a}^\dagger). \quad (\text{B.24})$$

Using the commutation relations $[\hat{a}, \hat{a}^\dagger \hat{a}] = \hat{a}$, $[\hat{a}^\dagger, \hat{a}^\dagger \hat{a}] = -\hat{a}^\dagger$, $[\sigma_+, \sigma_z] = -2\sigma_+$, and $[\sigma_-, \sigma_z] = 2\sigma_-$, we see by inspection that this equation is satisfied by $X = \sigma_+ \hat{a} - \sigma_- \hat{a}^\dagger$, so that

$$U = \exp \left[\frac{g}{\Delta} (\sigma_+ \hat{a} - \sigma_- \hat{a}^\dagger) \right]. \quad (\text{B.25})$$

Remembering that the conjugate transpose distributes over tensor products, we see that this X is indeed antihermitian. We compute

$$\begin{aligned} [X, H_{\text{int}}] &= 2\hbar g[\sigma_+ \hat{a}, \sigma_- \hat{a}^\dagger] = 2\hbar g(\sigma_+ \sigma_- \hat{a} \hat{a}^\dagger - \sigma_- \sigma_+ \hat{a}^\dagger \hat{a}) \\ &= 2\hbar g[|e\rangle\langle e|(1 + \hat{a}^\dagger \hat{a}) - |g\rangle\langle g|\hat{a}^\dagger \hat{a}] = 2\hbar g\sigma_z(\hat{a}^\dagger \hat{a} + \frac{1}{2}), \end{aligned} \quad (\text{B.26})$$

where we have subtracted a constant offset of $\hbar g$. Using this to calculate (B.23) to second order in $(\frac{g}{\Delta})^2$ and factoring yields the dispersive Hamiltonian

$$H_{\text{disp}} \approx \hbar \left(\omega_r + \frac{g^2}{\Delta} \sigma_z \right) \left(\hat{a}^\dagger \hat{a} + \frac{1}{2} \right) + \frac{1}{2} \hbar \omega_a \sigma_z. \quad (\text{B.27})$$

Remarkably, we see that this is effectively a Hamiltonian for an “uncoupled” cavity and atom, but with the cavity’s effective resonance frequency $\omega'_r = \omega_r \pm g^2/\Delta$ dependent on the state of the qubit! This is what causes the shift in transmission resonance which we can detect to infer the state of the qubit without disturbing it.

We can also regroup the dispersive Hamiltonian terms as

$$H_{\text{disp}} \approx \hbar \omega_r \left(\hat{a}^\dagger \hat{a} + \frac{1}{2} \right) + \frac{\hbar}{2} \left(\omega_a + \frac{2g^2}{\Delta} \hat{a}^\dagger \hat{a} + \frac{g^2}{\Delta} \right) \sigma_z. \quad (\text{B.28})$$

In this form we can interpret the effect of the dispersive interaction as creating a new effective atomic transition frequency $\omega'_a = \omega_a + \frac{2g^2}{\Delta} \hat{a}^\dagger \hat{a} + \frac{g^2}{\Delta}$ (a photon-induced Stark shift of $2g^2 n/\Delta$ and a vacuum fluctuation-induced Lamb shift of g^2/Δ [7]).

The dispersive eigenstates $|+, n\rangle \approx |e\rangle|n-1\rangle$ and $|-, n\rangle \approx |g\rangle|n\rangle$ can be found by

expanding (B.17) to first order in g/Δ :

$$\begin{aligned} |+, n\rangle &\approx \frac{g\sqrt{n}}{\Delta}|g\rangle|n\rangle + |e\rangle|n-1\rangle \\ |-, n\rangle &\approx |g\rangle|n\rangle - \frac{g\sqrt{n}}{\Delta}|e\rangle|n-1\rangle. \end{aligned} \quad (\text{B.29})$$

The $n = 1$ state only has one state (the ground state) to decay into, and so we can expect by the simple argument of how much time $|+, 1\rangle$ spends as a photon (remember vacuum Rabi oscillations) that the rate of decay of the atom from its excited state is

$$\Gamma \approx \left(\frac{g}{\Delta}\right)^2 \kappa + \gamma_{\perp} \equiv \gamma_{\kappa} + \gamma_{\perp}. \quad (\text{B.30})$$

We thus see that if $\kappa \gtrsim \gamma_{\perp}$, the decay rate of the atom can be enhanced an amount γ_{κ} by the presence of the cavity. This is a special instance of the Purcell effect [71, 72], and can be used in single photon sources for quantum optics experiments by encouraging a single atomic excitation to decay through a large κ cavity as a photon [7]. This effect can be the dominant source of relaxation for qubits in the vicinity of or above the lowest cavity mode [72], although at lower bias points, dielectric loss is currently believed to be dominant in Josephson junction-based superconducting qubits [13, 14, 73].

Appendix C

Transmission Line Circuits

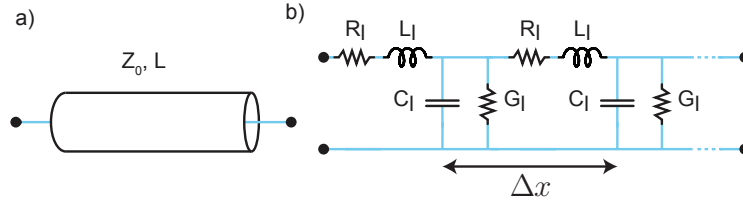


Figure C.1 Distributed circuit model of transmission line. Figure adapted from [7].

In what follows, x denotes the length coordinate along the line, $V(x, t)$ is the potential on the center conductor relative to the ground planes, and $I(x, t)$ denotes the current. As shown symbolically in Fig. C.1, suppose the CPW (or some other one-dimensional waveguide or transmission line) has a uniform capacitance to ground C_l , total self-inductance L_l , resistance R_l , and shunt conductance to ground G_l per unit length. Following Pozar [16], Kirchhoff's laws in infinitesimal form then read

$$\frac{\partial V(x, t)}{\partial x} = -R_l I(x, t) - L_l \frac{\partial I(x, t)}{\partial t} \quad (\text{C.1a})$$

$$\frac{\partial I(x, t)}{\partial x} = -G_l V(x, t) - C_l \frac{\partial V(x, t)}{\partial t}. \quad (\text{C.1b})$$

For sinusoidal steady-state signals of frequency ω , these then become (when using the complex phasor representation $Ae^{i\phi}e^{i\omega t}$ for V and I)

$$\frac{dV(x)}{dx} = -(R_l + i\omega L_l)I(x) \quad (\text{C.2a})$$

$$\frac{dI(x)}{dx} = -(G_l + i\omega C_l)V(x). \quad (\text{C.2b})$$

These transmission line equations combined yield

$$\frac{d^2 V(x)}{dx^2} = \gamma^2 V(x), \quad \frac{d^2 I(x)}{dx^2} = \gamma^2 I(x), \quad (\text{C.3})$$

where $\gamma(\omega) \equiv \sqrt{(R_l + i\omega L_l)(G_l + i\omega C_l)} \equiv \alpha(\omega) + i\beta(\omega)$ is the complex propagation constant. The traveling wave solutions of (C.3) are

$$V(x) = V_0^+ e^{-\gamma x} + V_0^- e^{\gamma x} \quad (\text{C.4})$$

and the analogous result for $I(x)$. From this we see that α represents dissipation while $\beta = 2\pi/\lambda = \omega/v_{\text{phase}} = \omega\sqrt{\epsilon_{\text{eff}}}/c$ contains wave parameters. Plugging (C.4) into (C.2a) yields

$$I(x) = \frac{1}{Z_0} (V_0^+ e^{-\gamma x} - V_0^- e^{\gamma x}), \quad (\text{C.5})$$

where $Z_0 \equiv \sqrt{\frac{R_l + i\omega L_l}{G_l + i\omega C_l}}$ is the *characteristic impedance*. Let us consider the termination of the TL by a load impedance Z_L ($x = 0$ at termination). Using (C.5),

$$Z_L \equiv \frac{V(0)}{I(0)} = \frac{V_0^+ + V_0^-}{V_0^+ - V_0^-} Z_0, \quad (\text{C.6})$$

from which we obtain the reflection coefficient

$$\Gamma \equiv \frac{V_0^-}{V_0^+} = \frac{Z_L - Z_0}{Z_L + Z_0}. \quad (\text{C.7})$$

Note that no reflection occurs when $Z_L = Z_0$, which is known as *impedance matching*. (C.4) and (C.5) then give

$$V(x) = V_0^+ (e^{-\gamma x} + \Gamma e^{\gamma x}) \quad (\text{C.8a})$$

$$I(x) = \frac{V_0^+}{Z_0} (e^{-\gamma x} - \Gamma e^{\gamma x}) \quad (\text{C.8b})$$

The impedance at a point $x = -l$, which can be interpreted as the impedance of a TL of finite length l , is then

$$Z_{\text{in}} = \frac{V(-l)}{I(-l)} = \dots = Z_0 \frac{Z_L + Z_0 \tanh \gamma l}{Z_0 + Z_L \tanh \gamma l} \quad (\text{C.9})$$

after a few lines of algebraic manipulation.

Bibliography

- [1] P. W. Shor, “Polynomial-Time Algorithms for Prime Factorization and Discrete Logarithms on a Quantum Computer.,” *SIAM J. Comput.* **26**, 1484–1509 (1997).
- [2] L. K. Grover, “A fast quantum mechanical algorithm for database search,” *Proceedings, 28th Annual ACM Symposium on the Theory of Computing.* pp. 212–219 (1996).
- [3] D. DiVincenzo, “The physical implementation of quantum computation.,” *Fortschr. Phys.* **48**, 771–783 (2000).
- [4] N. D. Mermin, *Quantum Computer Science: An Introduction* (Cambridge University Press, 2007).
- [5] E. Dennis, A. Kitaev, A. Landahl, and J. Preskill, “Topological quantum memory,” *J. Math. Phys.* **43** (2002).
- [6] A. G. Fowler, M. Mariantoni, J. M. Martinis, and A. N. Cleland, “Surface codes: Towards practical large-scale quantum computation,” *Phys. Rev. A* **86**, 032324 (2012).
- [7] D. I. Schuster, Ph.D. thesis, Yale University, 2007.
- [8] A. Blais, R.-S. Huang, A. Wallraff, S. M. Girvin, and R. J. Schoelkopf, “Cavity quantum electrodynamics for superconducting electrical circuits: An architecture for quantum computation,” *Phys. Rev. A* **69**, 062320 (2004).
- [9] J. Majer *et al.*, “Coupling superconducting qubits via a cavity bus,” *Nature* **449**, 443–447 (2007).
- [10] S. Filipp *et al.*, “Two-Qubit State Tomography Using a Joint Dispersive Readout,” *Phys. Rev. Lett.* **102**, 200402 (2009).
- [11] L. DiCarlo *et al.*, “Demonstration of two-qubit algorithms with a superconducting quantum processor,” *Nature* **460**, 240–244 (2009).

-
- [12] H. Paik *et al.*, “Observation of High Coherence in Josephson Junction Qubits Measured in a Three-Dimensional Circuit QED Architecture,” *Phys. Rev. Lett.* **107**, 240501 (2011).
 - [13] R. Barends *et al.*, “Coherent Josephson qubit suitable for scalable quantum integrated circuits,” <http://arxiv.org/abs/1304.2322> (2013).
 - [14] J. Chang *et al.*, “Improved superconducting qubit coherence using titanium nitride,” <http://arxiv.org/abs/1303.4071> (2013).
 - [15] C. Eichler, Ph.D. thesis, ETH Zürich, 2012.
 - [16] D. M. Pozar, *Microwave Engineering*, 3rd ed. (John Wiley & Sons, 2005).
 - [17] A. A. Clerk, M. H. Devoret, S. M. Girvin, F. Marquardt, and R. J. Schoelkopf, “Introduction to quantum noise, measurement, and amplification,” *Rev. Mod. Phys.* **82**, 1155–1208 (2010).
 - [18] B. Yurke, “Squeezed-state generation using a Josephson parametric amplifier,” *J. Opt. Soc. Am. B* **4**, 1551 (1997).
 - [19] B. Yurke, P. G. Kaminsky, R. E. Miller, E. A. Whittaker, A. D. Smith, A. H. Silver, and R. W. Simon, “Observation of 4.2-K equilibrium-noise squeezing via a Josephson-parametric amplifier,” *Phys. Rev. Lett.* **60**, 764–767 (1988).
 - [20] I. Siddiqi, R. Vijay, F. Pierre, C. M. Wilson, M. Metcalfe, C. Rigetti, L. Frunzio, and M. H. Devoret, “RF-Driven Josephson Bifurcation Amplifier for Quantum Measurement,” *Phys. Rev. Lett.* **93**, 207002 (2004).
 - [21] B. Yurke and E. Buks, “Performance of Cavity-Parametric Amplifiers, Employing Kerr Nonlinearities, in the Presence of Two-Photon Loss,” *J. Lightwave Technol.* **24**, 5054 (2006).
 - [22] M. A. Castellanos-Beltran, “Amplification and squeezing of quantum noise with a tunable Josephson metamaterial,” *Nature Physics* **4**, 929–931 (2008).
 - [23] E. A. Tholén, A. Ergül, K. Stannigel, C. Hutter, and D. B. Haviland, “Parametric amplification with weak-link nonlinearity in superconducting microresonators,” *Phys. Scr.* T137 (2009).
 - [24] C. Eichler, D. Bozyigit, C. Lang, M. Baur, L. Steffen, J. M. Fink, S. Filipp, and A. Wallraff, “Observation of Two-Mode Squeezing in the Microwave Frequency Domain,” *Phys. Rev. Lett.* **107**, 113601 (2011).

- [25] M. Hatridge, R. Vijay, D. H. Slichter, J. Clarke, and I. Siddiqi, “Dispersive magnetometry with a quantum limited SQUID parametric amplifier,” *Phys. Rev. B* **83**, 134501 (2011).
- [26] B. H. Eom, P. K. Day, H. G. LeDuc, and J. Zmuidzinas, “A wideband, low-noise superconducting amplifier with high dynamic range,” *Nat. Phys.* **8**, 623–627 (2012).
- [27] R. Vijay, D. H. Slichter, and I. Siddiqi, “Observation of Quantum Jumps in a Superconducting Artificial Atom,” *Phys. Rev. Lett.* **106**, 110502 (2011).
- [28] R. Vijay, C. Macklin, D. H. Slichter, S. J. Weber, K. W. Murch, R. Naik, A. N. Korotkov, and I. Siddiqi, “Stabilizing Rabi oscillations in a superconducting qubit using quantum feedback,” *Nature* **490**, 77–80 (2012).
- [29] D. Ristè, C. C. Bultink, K. W. Lehnert, and L. DiCarlo, “Feedback Control of a Solid-State Qubit Using High-Fidelity Projective Measurement,” *Phys. Rev. Lett.* **109**, 240502 (2012).
- [30] F. Mallet, M. A. Castellanos-Beltran, H. S. Ku, S. Glancy, E. Knill, K. D. Irwin, G. C. Hilton, L. R. Vale, and K. W. Lehnert, “Quantum State Tomography of an Itinerant Squeezed Microwave Field,” *Phys. Rev. Lett.* **106**, 220502 (2011).
- [31] C. Eichler, C. Lang, J. M. Fink, J. Govenius, S. Filipp, and A. Wallraff, “Observation of Entanglement between Itinerant Microwave Photons and a Superconducting Qubit,” *Phys. Rev. Lett.* **109**, 240501 (2012).
- [32] M. Hatridge *et al.*, “Quantum Back-Action of an Individual Variable-Strength Measurement,” *Science* **339**, 178–181 (2013).
- [33] L. D. Landau and E. M. Lifshitz, *Mechanics*, Vol. 1 of *Course of Theoretical Physics*, 3rd ed. (Elsevier, 1976).
- [34] L. N. Hand and J. D. Finch, *Analytical Mechanics*, 2nd ed. (Cambridge University Press, 1998).
- [35] Wikipedia, “Parametric oscillator — Wikipedia The Free Encyclopedia,” 2013, [Online; accessed 26-April-2013].
- [36] D. Kleppner and R. J. Kolenkov, *An Introduction to Mechanics* (McGraw Hill, 1973).
- [37] G. Blanch, in *Handbook of Mathematical Functions with Formulas, Graphs, and Mathematical Tables*, tenth ed., M. Abramowitz and I. Stegun, eds., (National Bureau of Standards, 1972), Chap. 20. Mathieu Functions.

- [38] M. O. Scully and M. S. Zubairy, *Quantum Optics* (Cambridge University Press, 1997).
- [39] D. F. Walls and G. J. Millburn, *Quantum Optics* (Springer, 1994).
- [40] M. J. Collett and C. W. Gardiner, “Squeezing of intracavity and traveling-wave light fields produced in parametric amplification,” *Phys. Rev. A* **30**, 1386–1391 (1984).
- [41] C. W. Gardiner and M. J. Collett, “Input and output in damped quantum systems: Quantum stochastic differential equations and the master equation,” *Phys. Rev. A* **31**, 3761–3774 (1985).
- [42] M. A. Castellanos-Beltran, Ph.D. thesis, University of Colorado Boulder, 2010.
- [43] W. Appel, *Mathematics for Physics and Physicists* (Princeton University Press, 2007).
- [44] I. Siddiqi *et al.*, “Direct Observation of Dynamical Bifurcation between Two Driven Oscillation States of a Josephson Junction,” *Phys. Rev. Lett.* **94**, 027005 (2005).
- [45] R. Vijayaraghavan, Ph.D. thesis, Yale University, 2008.
- [46] R. Vijay, M. H. Devoret, and I. Siddiqi, “Invited Review Article: The Josephson bifurcation amplifier,” *Rev. Sci. Instrum.* **80** (2009).
- [47] E. M. Stein and R. Shakarchi, *Fourier Analysis: An Introduction* (Princeton University Press, 2003).
- [48] F. Reif, *Fundamentals of Statistical and Thermal Physics* (Waveland Pr Inc, 2008).
- [49] M. H. Devoret, “Quantum Fluctuations,” In *Les Houches Session LXIII*, S. Reynaud, E. Giacobino, and J. Zinn-Justin, eds., pp. 351–386 (Elsevier, New York, 1997, 1997).
- [50] D. J. Griffiths, *Introduction to Quantum Mechanics*, 2nd ed. (Pearson, 2005).
- [51] C. M. Caves, “Quantum limits on noise in linear amplifiers,” *Phys. Rev. D* **26**, 1817–1839 (1982).
- [52] C. Kittel, *Introduction to Solid State Physics*, 8th ed. (Wiley, 2005).
- [53] M. Tinkham, *Introduction to Superconductivity*, 2nd ed. (Dover, 2004).
- [54] M. Göppl, Ph.D. thesis, ETH Zurich, 2009.
- [55] N. W. Ashcroft and N. D. Mermin, *Solid State Physics* (Brooks/Cole, 1976).

-
- [56] M. Wallquist, V. S. Shumeiko, and G. Wendin, “Selective coupling of superconducting charge qubits mediated by a tunable stripline cavity,” *Phys. Rev. B* **74**, 224506 (2006).
- [57] E. M. Purcell, *Electricity and Magnetism*, 2nd ed. (McGraw-Hill, 1985).
- [58] J. Fink, Ph.D. thesis, ETH Zurich, 2010.
- [59] M. Sandberg, C. M. Wilson, F. Persson, T. Bauch, G. Johansson, V. Shumeiko, T. Duty, and P. Delsing, “Tuning the field in a microwave resonator faster than the photon lifetime,” *Appl. Phys. Lett.* **92** (2008).
- [60] P. A. M. Dirac, *Principles of Quantum Mechanics* (Oxford University Press, 1982).
- [61] S. Gasiorowicz, *Quantum Physics* (Wiley, Third Edition, 2003).
- [62] M. Göppl, A. Fragner, M. Baur, R. Bianchetti, S. Filipp, J. M. Fink, P. J. Leek, G. Puebla, L. Steffen, and A. Wallraff, “Coplanar waveguide resonators for circuit quantum electrodynamics,” *J. Appl. Phys.* **104** (2008).
- [63] R. N. Simons, *Coplanar Waveguide Circuits, Components, & Systems* (Wiley, 2001).
- [64] R. E. Collin, *Foundations for Microwave Engineering*, 2nd ed. (Wiley-IEEE Press, 2000).
- [65] G. Stan, S. B. Field, and J. M. Martinis, “Critical Field for Complete Vortex Expulsion from Narrow Superconducting Strips,” *Phys. Rev. Lett.* **92**, 097003 (2004).
- [66] K. Yoshida, K. Watanabe, T. Kisu, and K. Enpuku, “Evaluation of Magnetic Penetration Depth and Surface Resistance of Superconducting Thin Films using Coplanar Waveguides,” *IEEE Trans Appl Supercond* **5** (1995).
- [67] G. J. Dolan, “Offset masks for lift-off photoprocessing,” *Appl. Phys. Lett.* **31**, 337–339 (1977).
- [68] V. Ambegaokar and A. Baratoff, “Tunneling Between Superconductors,” *Phys. Rev. Lett.* **11**, 104–104 (1963).
- [69] D. Ristè, J. G. van Leeuwen, H.-S. Ku, K. W. Lehnert, and L. DiCarlo, “Initialization by Measurement of a Superconducting Quantum Bit Circuit,” *Phys. Rev. Lett.* **109**, 050507 (2012).
- [70] D. J. Griffiths, *Introduction to Electrodynamics* (Prentice-Hall, 1999).
- [71] E. M. Purcell, *Phys. Rev.* **69**, 681 (1946).

-
- [72] A. A. Houck *et al.*, “Controlling the Spontaneous Emission of a Superconducting Transmon Qubit,” *Phys. Rev. Lett.* 101 (2008).
- [73] J. Wenner *et al.*, “Surface loss simulations of superconducting coplanar waveguide,” *Appl. Phys. Lett.* 99 (2011).